EUROPEAN SPALLATION SOURCE

MXType.Localized	
Document Number	MXName
Project Name	<<project name>>
Date	21/03/2014
Revision	MXRevision MXPrinted Version
State	MXCurrent

ESS Instrument Construction Proposal
FREIA - Revised

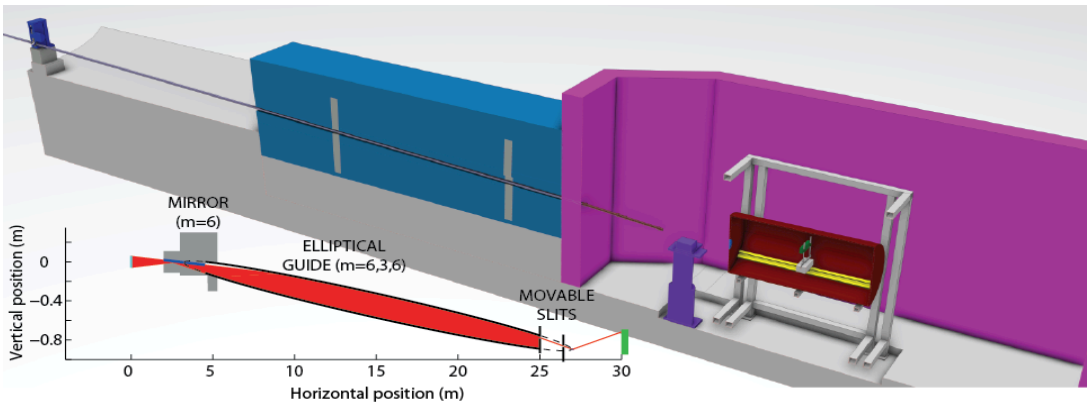

	Name (name, title, e-mail address)	**Affiliation**(name of institution, address)
Proposer	Hanna Wacklin hanna.wacklin@esss.se	ESS
Co-proposers	Anette Vickery	NIB, Copenhagen University NEXMAP, DTU
ESS coordinator	Hanna Wacklin	

The following table is used to track the ESS internal distribution of the submitted proposal.

	Name
Document submitted to	Ken Andersen
Distribution	Dimitri Argyriou, Oliver Kirstein, Arno Hiess, Robert Connatser, Sindra Petersson Årsköld, Richard Hall-Wilton, Phillip Bentley, Iain Sutton, Thomas Gahl, relevant STAP

ENCLOSURES

<< FREIA_Appendix.pdf>>

European Spallation Source ESS AB
Visiting address: ESS, Tunavägen 24
P.O. Box 176
SE-221 00 Lund
SWEDEN

www.esss.se

EXECUTIVE SUMMARY [1-2 PAGES]

FREIA, the Fast Reflectometer for Extended Interfacial Analysis, is a versatile multipurpose instrument with a horizontal sample geometry and a broad simultaneous Q-range for structural and kinetic studies. The instrument design has been optimised for the largest and fastest growing scientific areas of soft condensed matter and life sciences, and also includes a polarisation system for studies of magnetic materials. For maximizing the benefit of the high ESS flux for kinetic studies, a novel collimation system for measuring the full Q-range simultaneously has been designed.

The types of scientific challenges that FREIA will address particularly well include:

- self-assembly of surfactants, polymers and proteins at solid and liquid interfaces
- rearrangement processes in thin films (diffusion, annealing, exchange etc.)
- encapsulation and release in e.g. drug delivery materials, sensors and energy storage
- switchable materials that respond to external stimuli
- chemical and biochemical surface reactions

In these systems, structural changes can occur over a broad length scale, often simultaneously, and the timescales can vary from sub-second to several minutes or even hours.

FREIA has an elliptical guide design focusing a neutron beam with a broad vertical divergence and wavelength range onto the sample surface. From this high-divergence beam, a well-collimated beam can be selected using high-precision slits, which allows measurements to be carried out without moving the sample, as illustrated below. This geometry, not available on any existing instrument, is ideal for studying kinetics, as the angle of incidence can be changed rapidly using a fast shutter system to effectively record the full Q-range simultaneously.

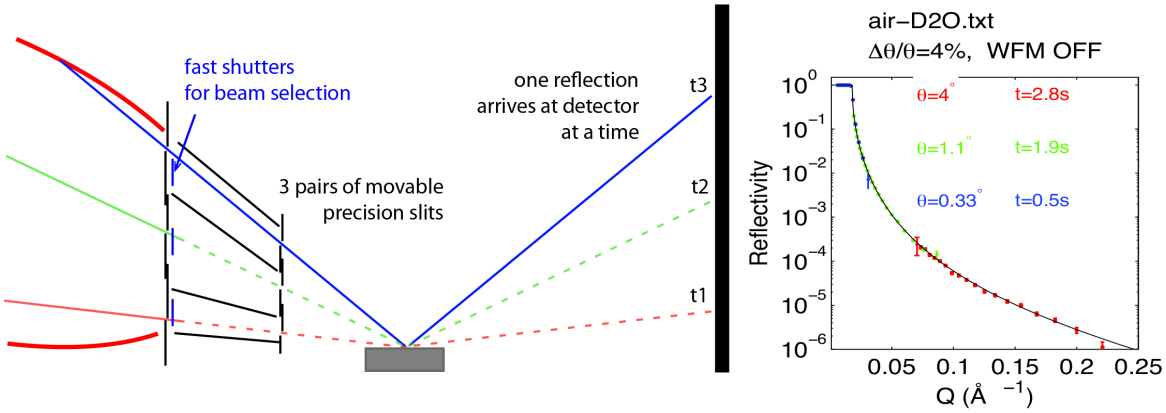

Measurements on FREIA are done by selecting a collimated beam from a broad divergence, either using precision slits, or by fast beam shutters for kinetic experiments b) Simulated reflectivity of a 4cm x 4cm D_2O free liquid surface in air, with an estimated real measurement time of 5.2s for all three angles of incidence.

In the low-medium resolution mode FREIA exploits the advantages of the ESS long pulse source to the full, giving rise to significant reduction in measurement times, which we have demonstrated by careful simulations of virtual experiments. A sophisticated chopper system for Wavelength Frame Multiplication (WFM) can provide a constant relative wavelength resolution dλ/λ=1.5% appropriate for thicker films up to 500Å. Due to the increasing demand for off-specular and Grazing Incidence Small Angle Scattering (SANS) measurements across the scientific fields, a simple slit collimation system for GISANS is also available, with collimation lengths up to 8m to cover lateral structures up to 200nm.

A simple polarisation system using a short polarising S-bender is included in the day 1 design of the instrument in order to take advantage of the recent successes made by magnetic contrast variation in soft matter and biological systems, and will also allow polarised reflectometry studies of a wide range of other systems, with the exception of very small samples.

An inverted beam geometry configuration is available for accessing sample from below the interface, of particular interest for liquid-liquid interfaces, which will benefit from the ESS flux to reduce the sample length and attenuation by the liquids.

The scientific scope of FREIA covers the vast majority of experiments in soft condensed matter, advanced materials and life science, as well as a significant proportion of hard condensed matter. The specially designed kinetic mode that uses fast shutters will enable new science in all areas of thin film growth, self-assembly, rearrangement and surface reactions due to the extended simultaneous Q-range. The instrument design is optimised for 4cm x 4cm samples, but samples between 10mm x 10mm and 10cm x 10cm can also be measured.

FREIA will cater for up to 90% of the reflectometry community, and will therefore function as an excellent first instrument at ESS. FREIA will ideally be complemented by a high-resolution polarised reflectometer optimised for very small samples important for state-of-the art hard condensed matter materials, and a dedicated grazing-incidence SANS/off-specular instrument for determining lateral structures with more flexibility and on extended length scales.

TABLE OF CONTENTS

ENCLOSURES **1**

Executive Summary [1-2 Pages] **2**

Table of ContentS **3**

1 Instrument Proposal **4**

1.1 Scientific Case 4

1.2 Description of Instrument Concept and Performance 8

1.3 Technical Maturity 32

1.4 Costing 32

2 List of Abbreviations **35**

1 INSTRUMENT PROPOSAL

1.1 Scientific Case

1.1.1 Neutron reflectometry at ESS

Neutron reflectometry covers a very broad spectrum of science involving the growth, self-assembly, structure and interactions of a wide variety of thin films and has an impact on all the core areas of the ESS materials science case. Considering that the advanced thin film materials of the future will be increasingly complex, there is an urgent and continued need to develop high performance neutron reflectometers to elucidate their structure. The strong European user base and facilities mean that there is also a need to be ambitious and differentiate the ESS reflectometry suite from existing instruments.

Reflectometry is very well suited to the ESS long pulse time structure, with significant gains expected due to the high cold neutron flux and the relatively relaxed resolution requirements, which allow the full pulse width to be used for many experiments. The time averaged flux of the ESS is estimated to be comparable to that of the ILL cold source, which gives rise to a peak ESS flux of approximately 25 times higher given the 14Hz frequency and 2.86ms pulse length at 5MW. For reflectometry, the ESS offers a possibility to relax the experimental resolution up to the source resolution to gain more usable flux, up to the equivalent of the time-averaged ILL cold source brightness on the sample. In contrast, time-of-flight instruments at reactor sources need to employ pulse shaping choppers, which typically only transmit ~1-2% of the source intensity to the sample. However, the wide range of film thicknesses of interest places a broad range of requirements on instrument resolution and in many cases requires the use of pulse shaping choppers at ESS, in which case the expected flux is proportional to the resolution. Given that there are overall a broad range of requirements on sample size, resolution and bandwidth in reflectometry experiments, it is crucial to optimise a suite of instruments with specific capabilities to enable all of the areas of science at a world leading level.

1.1.2 The user community

Figure 1 shows the distribution of scientific papers published between 2003 and 2013 for the largest scientific areas that use reflectometry, according to records kept by the facilities (ISIS, ILL, HZB, SNS, NIST, ANSTO and PSI are included). It should be noted that many papers span more than one of the topics, and that only a selection of the largest science areas is presented in the graphs, which match well the results of publication surveys done e.g. at ILL over a number of years. The largest sections of the user community today are interested in soft condensed matter, polymers and life science, which have a significant overlap with more general chemistry and materials science at surfaces. Comparing the evolution of publications between 2003-2007 (339) with those in 2008-2013 (507), the total number of unique publications has risen by 50%, reflecting that a number of new instruments have come available within this period (for example FIGARO, Inter, Polref, Offspec, Platypus). In addition to this, although the growth that has occurred in the soft matter and life science areas is the largest, there is a general increase in many other areas as well, including magnetism and polarised neutron reflectometry (PNR). In this context "kinetics" was taken to represent all papers involving kinetics, diffusion, rearrangement, reactions or interactions at surfaces, which have or could have used time-resolved reflectometry. "Liquids" was taken to represent all types of free liquid surfaces, i.e. air-solution, air-water and liquid-liquid interfaces.

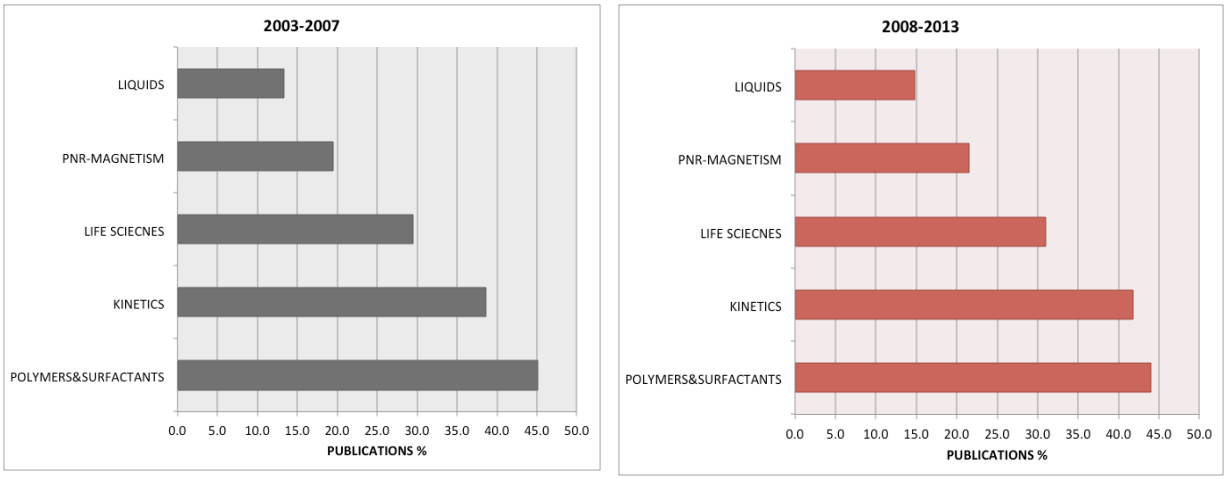

Figure 1. Reflectometry publications in the largest scientific areas during 2003-2007 and 2008-2013, based on publication records collected from ISIS, ILL, HZB, SNS, NIST and PSI. Please note that many papers involve several of the keywords used.

The user community is vibrant, and it is common for one publication to cite several instruments and facilities. A typical oversubscription factor lies between 2 and 3 for most instruments.

1.1.3 The Science case for FREIA

The proposed FREIA instrument has been optimised for the largest and fastest growing science areas of soft condensed matter and life sciences, where both the structure and kinetics in thin film samples are of interest, particularly during their formation and in response to environmental changes. The design of FREIA also makes it highly suitable for a wide range of materials chemistry and hard condensed matter science.

The challenges to be met in soft condensed matter and the life sciences are as wide ranging as the topics investigated. While the sensitivity of neutrons to structural features offers a significant advantage in all types of multicomponent systems, there is a clear trend to follow time-dependent processes due to the development of time-of–flight reflectometers in the past three decades facilities world-wide. These processes include, but are not limited to:

- Self-assembly of surfactants, polymers and proteins at solid and liquid interfaces
- Rearrangement processes in thin films: e.g. polymer interdiffusion, inter-layer movement (e.g. lipid flip-flop), annealing/drying/exchange/wetting processes in composite films such as photovoltaic materials.
- Encapsulation and release of components in e.g. plastics, polymer blends, drug delivery and implant materials, chemical and biological sensors
- Switchable materials that undergo structural changes in response to external stimuli (chemical, mechanical, electrical or electromagnetic) with potential device applications
- Surface reactions that involve change in the film structure or chemical composition; e.g. enzyme catalysis, oxidation or other film degradation reactions, receptor-ligand binding, drug-target interactions, surface functionalisation etc.

These systems can be investigated in-situ by many surface sensitive techniques from neutron and X-ray reflection, ellipsometry/dual polarisation interferometry, quartz crystal microbalance to scanning probe and fluorescence microscopies. Most of these techniques however either lack chemical sensitivity to the sample composition, or require invasive labelling to derive this information.

Time-of-flight (tof) neutron reflectometry offers the possibility to record a range of Q-values simultaneously, allowing determination of both structure and chemical composition as a function of time. Deuterium labelling in soft condensed, organic or biological materials also gives the measurements a unique sensitivity to the composition of multicomponent samples, which is of great importance for both fundamental studies and technological applications. As the systems of interest continue to become more complex in their composition and behaviour, the importance of neutron scattering methods will only increase. The usefulness of tof-reflectometry critically depends on the ability to match both the time-resolution and the dynamic Q-range of the measurements to the structural changes investigated. The time and length scales that can potentially be followed by neutron reflectometry in such systems vary from a few to several hundred Ångströms, and from milliseconds to minutes, or even hours. Today, large samples (up to 30mm x 100mm) are used to reach measurement times on the second-minute scale on world-leading reflectometers, such as FIGARO at ILL, or Inter at ISIS TS2. At ESS it should be possible to use the flux gain to reach sub-second to second measurement times on samples that are of comparable size, or alternatively to reduce the sample size by an order of magnitude. The main challenge for kinetic measurements is that they are typically only possible within a limited Q-range, as to record the full range of interest involves reconfiguring the instrument 1-2 times to access different angles of incidence, which can take several minutes.

1.1.4 The FREIA Solution

The key scientific drivers for FREIA are to allow fast kinetic measurements on the ms-s timescale with the broadest possible simultaneous Q-range, and to provide high-speed measurements across the current and future scientific scope of reflectometry. To make the best use of the ESS cold source flux, a novel guide and collimation system has been developed for this purpose, which allows the entire Q-range to be accessed without any movement of the main instrument optics or the sample. The horizontal sample geometry combined with a variable resolution will cater for a broad range of interfaces and samples, making it a versatile instrument that will ideally be complemented by a polarised reflectometer optimised for samples smaller than 1cm^2 and high-resolution studies (dQ/Q< 2%), as well as a dedicated grazing-incidence SANS/off-specular instrument for 2D-3D film structure. Below is a small selection of examples of the type of scientific challenges for which FREIA is optimised.

Scientific Challenges for FREIA:

- Fast adsorption and desorption processes: Figure 2a shows the fastest acquisition times for determining the surface excess in thin films to a reasonable accuracy on FIGARO, which are in the region of 30-40s. Applications that need faster acquisition times include atmospheric chemistry (oxidation of aerosol surfaces), and surfactant/polymer adsorption at both static and dynamic interfaces. In the future, new applications at either liquid or solid interfaces that need fast measurement times include the reactions of a surface to e.g. fingerprints or shockwaves. At ESS it should be possible to monitor such processes in the sub-second to second time-regime, depending on the Q-range.
- Fast reactions at surfaces, cyclic processes and external stimuli: As data at ESS will be collected in event mode as a standard, the limit of time-resolution in any cyclic process will be the uncertainty in the neutron arrival time at the sample, which is typically of the order of 200μs. This means that such stroboscopic experiments on e.g. electrically driven processes can reach the sub-ms range and probe ever faster reactions, such as early stages of surface association/dissociation and conformational changes at surfaces.
- Biological interactions: The initial interactions of proteins and enzymes with cell membranes are of great interest for determining biological mechanisms underlying both health and disease. The challenge lies in observing a broad enough dynamic Q-range simultaneously. For example in phospholipase A_2 catalysed lipid hydrolysis, the enzyme causes both structural and compositional changes that occur over a wide range in Q. Figure 2b shows such data recorded in 1-2min in D_2O solutions in which the contrast is good and the reaction is slowed down 10 times due to isotope

effects. On FREIA it will be possible to study the kinetics of this biochemical reaction in H_2O. Many other types of biochemical reactions and interactions that will in the future benefit from such measurements form the basis for the function of biological and chemical thin film sensors.

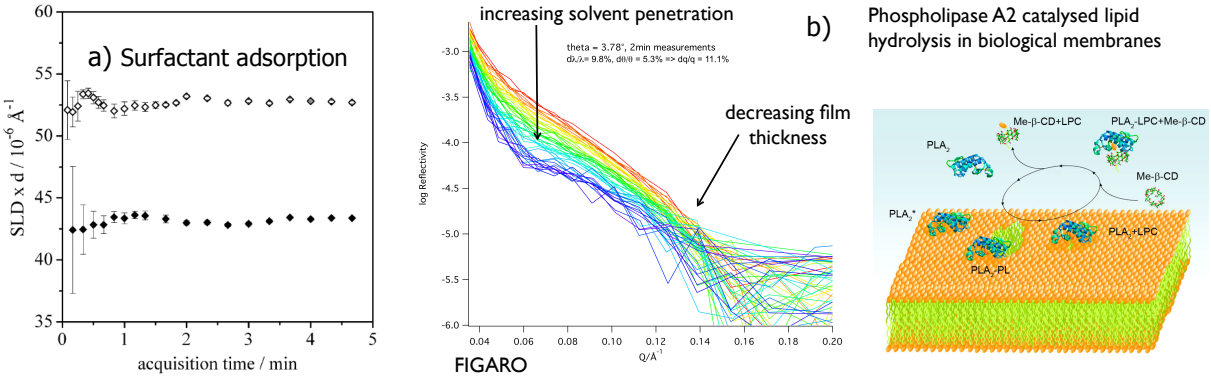

Figure 2. a) Minimum acquisition time to determine the scattering length density of a thin surfactant film (b) 2 min. measurements of enzyme catalysed lipid hydrolysis in the broadest possible simultaneous Q-range. Both measured on FIGARO using dλ/λ=7.25% FWHM. From R. Campbell, A., H. P. Wacklin, et al. (2011) EPJ+ 126, 107.

- Liquid-liquid interfaces (e.g. oil-water): These interfaces are difficult to study due to the drastic beam attenuation by the liquids, mainly as a consequence of the long path length through the sample at grazing angles of incidence. Today, µm-thick spin coated oil-films are used to mimic these systems and overcome this problem, but the measurement times are relatively long and the sample background high (Zarbakhsh, et al. Meas SciTechnol, 1999,10, 738.) The ESS flux will offer a significant reduction in the required sample size, and hence the experimental path length, which should allow real liquid-liquid interfaces to be investigated. Due to a high sample background in these systems, a limited Q-range up to Q=0.2 $Å^{-1}$ is typically sufficient.

- In-situ studies of inter-diffusion at buried interfaces: Many studies today use multiple samples in which each sample has been annealed or quenched at different times in order to study mechanisms that would ideally be best studied in-situ. Applications include many technologically important materials such as photovoltaics, polymer multilayers, and energy materials. For example the early-stage kinetics of deuterium adsorption into hydrogen storage media as shown in Figure 3 could be studied in-situ on FREIA.

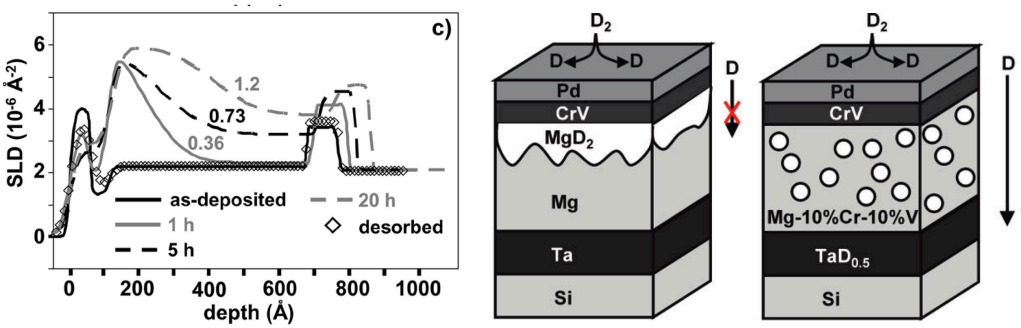

Figure 3. Deuterium adsorption into hydrogen storage materials monitored as change in the scattering length density of the Mg layer in samples annealed at different times. From W. P., Kalisvaart, E. J. Luber, et al. (2012). J. Phys. Chem. C **116**(9): 5868-5880.

- Chemically or biologically active samples for industrial and medical applications, which need high-throughput screening of activity and structure in small samples: many of these users would like to screen 200-300 samples per experiment, which is very difficult with current measurement times and the oversubscription of instruments. This area will be crucial for attracting industrial users to ESS, particularly from the biomedical and pharmaceutical sectors.

- Magnetic contrast and polarised measurements: The advances made recently in employing permalloy layers for magnetic contrast in soft matter and life science experiments have shown that this has great potential to be exploited more widely, especially in the time-of-flight mode and with faster measurement times. On FREIA, a simple polarisation system consisting of a solid-state S-bender capable of efficiently polarising the entire wavelength band will allow these studies to use all the measurement modes of the instrument with greatly improved measurement times.

In the above areas, the length scales of interest span 1Å-1000Å, so instruments with resolution options from 1% ≤ dQ/Q ≤20% are required. The thickest films from 500-1000Å requiring the highest resolutions are usually deposited on solid supports however, and do not require a horizontal sample geometry. For the majority of purposes in specular reflectometry a Q-range of 0.005 – 0.5 $Å^{-1}$ is sufficient, and in cases where bulk liquid phases are part of the sample, the signal is typically background limited beyond Q = 0.25 $Å^{-1}$.

1.2 Description of Instrument Concept and Performance

1.2.1 Instrument layout

A schematic layout of the instrument and its main components is shown from the side and from the top in Figure 4. The total length of the instrument is 25 m from the moderator. A 2.5 m deflecting mirror begins at 2m from the moderator. The mirror is inclined at 1° to the x-axis (horizontal) and has an m= 6 coating to deflect the beam down into the main guide, which is inclined at 2° below the x-axis and has its first focal point at 2.95m from the source. The deflecting mirror acts as a virtual source of neutrons, as described in more in detail section 1.2.2. The guide has elliptical top/bottom faces while the side walls are straight. The width of the guide is constant at 50 mm, and the height of the elliptical guide varies from 16 to 25 cm. The deflecting mirror and beginning of the elliptical guide enclose a multichannel bender with 4 vertical channels (0.5mm walls) and 56m radius of curvature, up to 11.5m from the moderator. The elliptical guide is 15.5m long, and has a variable m-coating: 7.5% (2.3m) with m= 5.45 followed by 20% (6.2m) with m=4.1 at both ends (6.2m) and a 7m m=3 section in the middle. The sidewalls of the simulated guide have the same m-coating as the top and bottom walls (because they cannot be independently defined for the continuous elliptical guide component in McStas), and there is therefore further scope for improving the flux on sample by optimizing this. The elliptical shape is not necessary in the first section of the guide up to 8.9m, as this is the first point where neutrons are reflected, and the top and bottom faces can be replaced by straight m=1 or absorbing walls. The elliptical guide ends at 20m, and is followed by a 10cm gap for a solid-state silicon S-bender for polarizing the beam before the collimation section. The 2m collimation section consists of interchangeable guide sections for i) kinetic measurements, ii) inverted geometry experiments using a deflection mirror and iii) a horizontally focusing guide for small samples, which are described in more detail in section 1.2.5. The beam incident on the horizontal sample is defined to the chosen angular resolution and footprint by two sets of precision slits located at 20m and 22m respectively. Immediately after the first collimation slit at 20m, a system of 3 fast shutters will select the angle of incidence for kinetic experiments. The slit and shutter system is described in more detail in sections 1.2.5.1-1.2.5.2. The sample position is located 28cm after the second collimation slit. In order to more efficiently illuminate small samples (<1cm), an additional slit can be mounted at 7-10cm before the sample. The instrument includes a set of additional slits for GISANS collimation at 8m, 6.5m and 4m before the sample. The sample to detector distance can be varied from 1 to 8m.

The instrument incorporates 8 choppers located at 6.5m, 6.7m, 7m, 8.5m, 10m, 11.1m, 15m and 15.6m from the source, whose function is described in detail in section 1.2.4. The chopping is done

from above across the 50mm width of the guide. The choppers have been drawn in Figure 4b) with the minimum diameters found by simulation to illustrate the horizontal space requirements. The dashed lines in Figure 4b indicate the beam centres of the neighbouring beam ports, from which it is clear that about 10° are required for this instrument depending on the neighbouring instrument. At the sample position, same-level, side access to the sample area is necessary as many of the experiments involve relatively large (50-100kg) and delicate sample environments. A minimum width of 3m at the sample area is envisaged. The detector will need to move both along the beam (7m) and vertically (1m), and have an evacuated flight path. This can be a cylindrical or rectangular tank – the best engineering solution for this will be decided during the design phase.

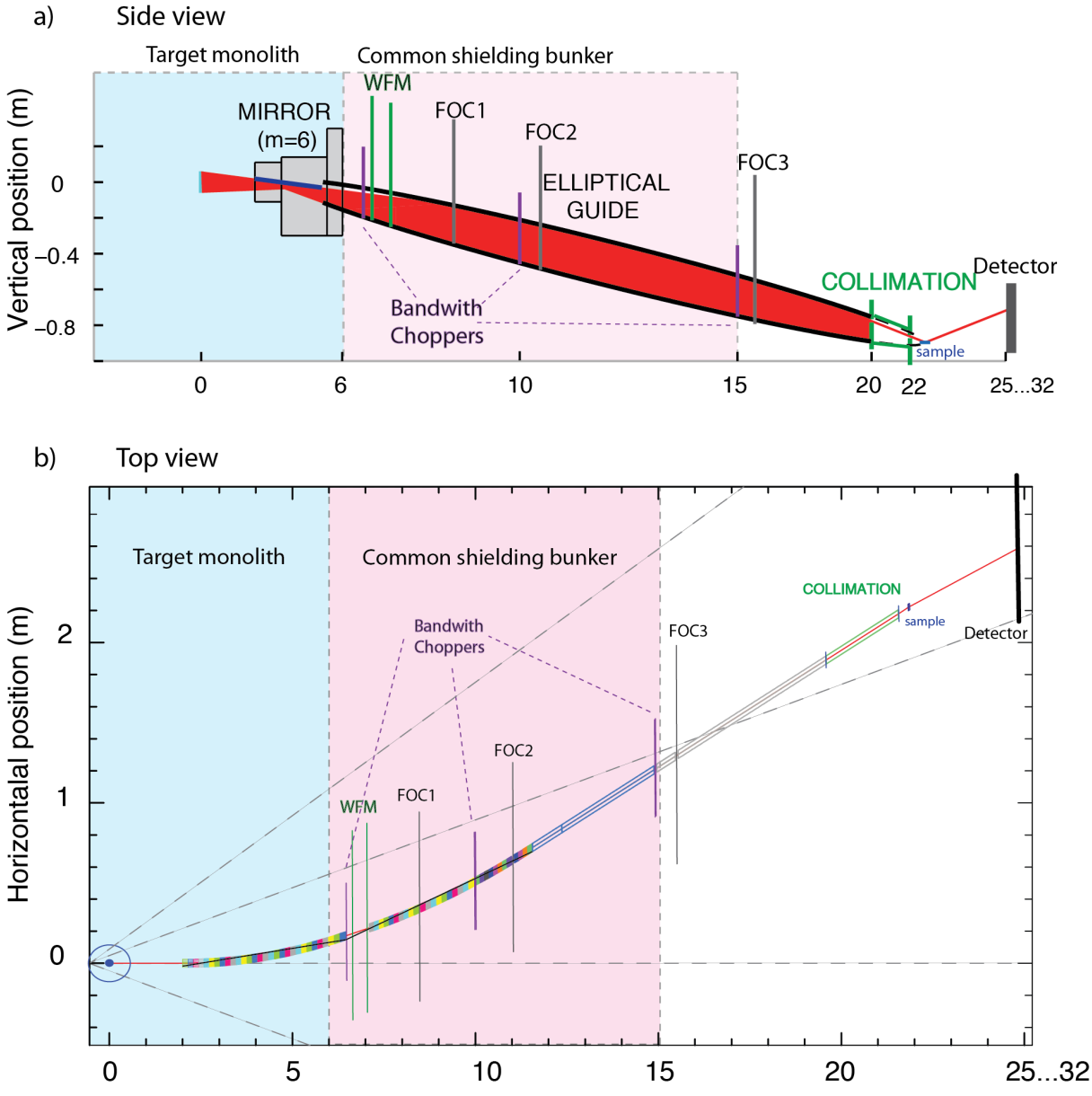

Figure 4. Schematic instrument layout – a) from the side and b) from the top, with the dashed lines indicating the centres of the neighbouring beam axis around the instrument. The choppers are drawn as simulated in panel b). The second line of sight is lost at 11.5m from the moderator, 10.5m before the sample position. The detector position is movable up to 32m.

1.2.2 Neutron guide system and beam transport

1.2.2.1 Beam extraction – Vertical

The ESS baseline beam extraction channel starting at 2m has a height of 220mm in the first 1.7m, after which the height increases to 440mm. In order to view the entire moderator surface from the elliptical guide, a 2.5m deflecting mirror is placed in the narrow section of the beam port, as illustrated in Figure 5. The length, coating and position of the mirror were optimised so that it can view the shortest wavelengths (2.5Å) from the entire 12cm moderator surface – neutrons from the top of the moderator can pass under the mirror inclined at 1°, 2.5Å neutrons can be reflected at the end of the mirror at up to their critical angle, while longer wavelengths can be reflected on the entire mirror from the entire moderator. The first focal point of the elliptical guide sits at 2.94m, 0.8m before the centre of the deflecting mirror which acts as a virtual source of neutrons. A 20mm pinhole at 2.94m can be used to block the direct view from the sample to the moderator, in which case the position of last line of sight is at 14m (8m before the sample). The elliptical guide can only view/reflect neutrons starting at 8.9m due to this geometry, and as a consequence the top and bottom faces of the guide can be replaced by straight m=1 or absorber walls until this point.

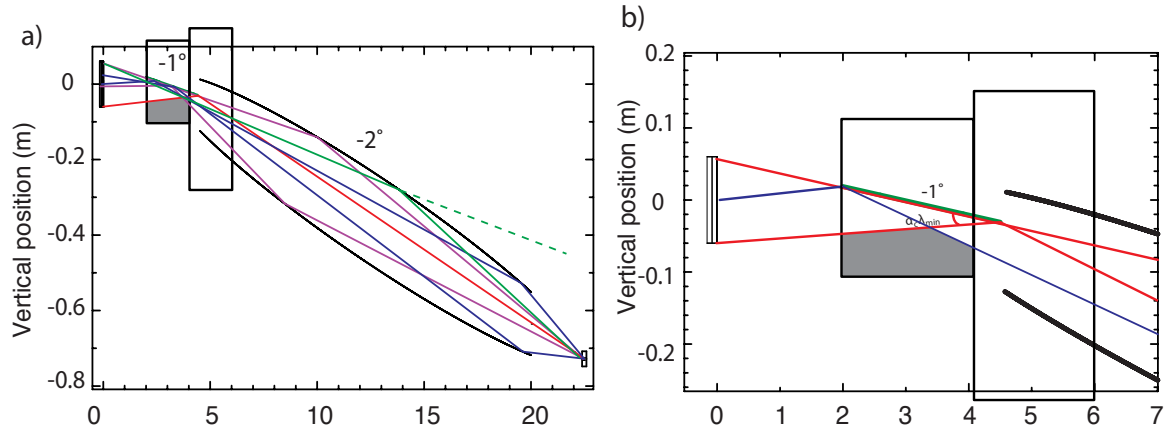

Figure 5. Vertical beam extraction geometry – a) the deflecting mirror is positioned to view the entire 12cm moderator surface and illuminate both faces of the elliptical guide, b) Detailed view of the first 7m showing the mirror position and length, which were optimised to allow the shortest wavelength (2.5Å) from the entire moderator to illuminate the elliptical guide, whose first focal point is located at 2.94m. A 20mm high pinhole placed at this position can be used to block direct view from the sample to the moderator (with last line of sight at 14m).

1.2.2.2 Beam extraction - Horizontal

The direct line of sight (LOS) to the moderator needs to be eliminated twice considering the likely high fast neutron background of the ESS. We have optimized a horizontally curving multichannel bender to transport 2.6Å neutrons and to provide two-fold LOS elimination (considering the full bender width) before 11.5m from the source. Figure 6 shows the geometry of this bender, as well as its relative brilliance transfer compared to an identical straight guide with the same number of channels for a radius of curvature of 56m, 4 channels separated by 0.5mm walls, with m=4.4 outer and m= 2.5 inner surface coating. The bender consists of two 4.5m sections separated by a 0.5m gap for the first three choppers at 6.5m, which has side walls but no channels. Sections 1 and 2 in the Appendix give more details on the design and optimization of the bender.

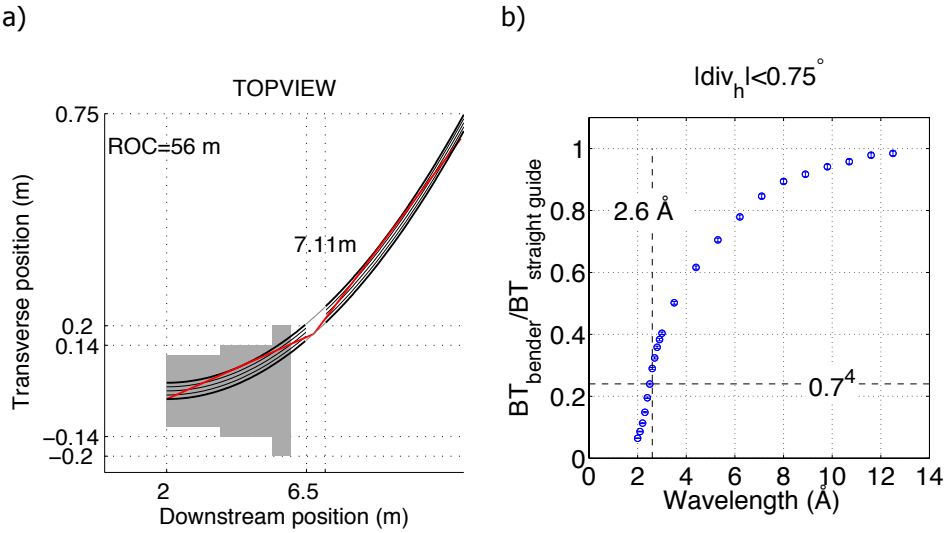

Figure 6 a) 4.5m + 4.5m bender geometry for a 56m radius of curvature and 4 channels, b) the relative brilliance transfer as function of wavelength, compared to an identical straight guide with the same number of channels.

1.2.2.3 Elliptical guide design and performance

The neutron guide system was optimised to deliver a broad divergence range and a broad wavelength band to the sample position, to enable measurements on liquid surfaces without moving the sample or the optics. The resulting guide is inclined at -2° relative to the horizontal, and delivers ±2° of divergence around the guide axis. Thus, an angular range of 0.2-4° in the scattering plane is focused on the surface of the horizontal sample centred at 22.28m. The last 2m of the guide system consist of a vertically absorbing collimating guide (between the two sets of collimating slits) and is designed to eliminate any parasitic scattering from the elliptical guide.

The instrument study was motivated by the need to find a sufficiently homogeneous distribution of flux over the full vertical divergence range and wavelength band. For this, using an inclined elliptical guide to directly extract the required divergence from the moderator would be the optimal solution, but as the first 1.7m of the beam extraction unit has a restricted height (220mm), a 2.5m long deflecting mirror inclined at -1° reflects the beam into the elliptical guide beginning at 4.5m from the source. This leads to two gaps in the divergence profile as shown in Figure 7, but does not affect the overall performance or flexibility of the instrument. The optimisation procedure for the elliptical guide is explained in more detail in the Appendix sections 5.4 and 5.5.

Figure 7 shows the flux as a function of wavelength and angle of incidence at the sample position. The gaps in the divergence originate partly from the mirror reflection and partly from the elliptical guide shape not being realised completely (15.5m of guide corresponds to 79% of the focal point to focal point distance of 19.6m). However, as explained in more detail in section 1.2.3, the full Q-range can be covered with sufficient flexibility in the choice of angles of incidence despite these gaps.

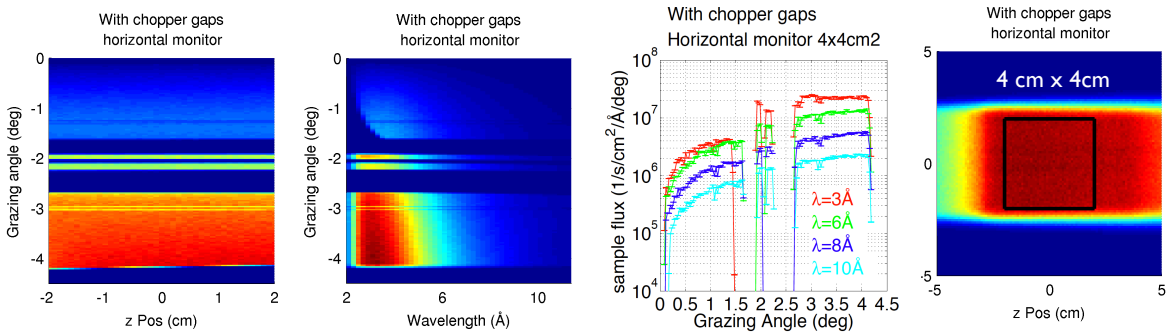

Figure 7. From Left to right: The beam characteristics on a 4cm x 4cm sample area i) divergence vs sample length (all wavelengths), ii) divergence vs wavelength (over 4cm x 4cm area), iii) the full uncollimated intensity as function of angle of incidence, and iv) full white beam footprint at the sample (all wavelengths and full divergence), where the rectangle indicates a 4cm x 4cm area. The simulated guide included 5cm gaps for single disc choppers and 7cm gaps for the double disks in the locations listed in Table 1, section 1.2.4.

The instrument was optimised for 4cm x 4cm samples, which is considerably smaller than the sample sizes used for free liquid samples today (10cm x 3cm) or the average solid-liquid sample cells (8cm x 5cm). The right hand panel in Figure 7 shows the sample area illuminated by the fully open uncollimated neutron beam. As can be seen, a 4cm x 4cm sample can be fully and homogeneously illuminated, as well as longer samples up to 8cm if centred somewhat further forward from the nominal sample position.

The guide system incorporates several choppers, and the required breaks in the guide could potentially lead to further beam losses or gaps in divergence. The effect chopper positioning was simulated for 5cm and 10cm gaps along the full guide length, and the result is shown in Figure 8. The end of the elliptical guide is more sensitive to the presence gaps, but for gaps of the order of 5cm-7cm (as estimated for single and double disc choppers for the ESS chopper group), the combined effect of all chopper gaps is less than 10% of the total flux on sample.

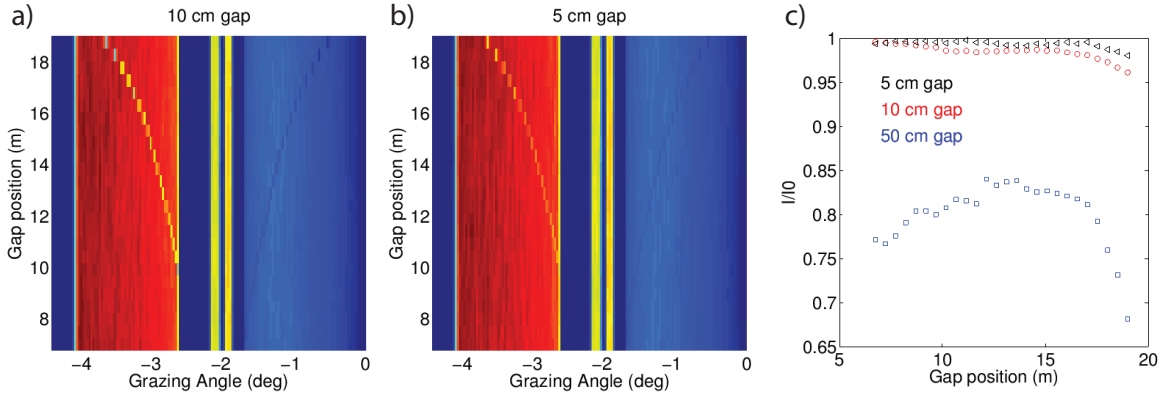

Figure 8. The effect of chopper gaps on the divergence delivered to the sample position as function of chopper position along the elliptical guide for a) 10cm and b) 5cm gaps. The effect on the total flux at the sample position is shown in c) for 5cm, 10cm and 50cm gaps.

1.2.2.4 Sample illumination and Gravity Effects

Gravity was included in all the simulations, and for the 2.5-11.4Å wavelength band the effects on the vertical beam distribution are small. The collimating slit positions need to be adjusted to account for

the parabolic neutron paths but the effect is small (<0.1mm). There is some spreading of the beam footprint at the sample position, which leads to the wavelength distributions as function of angle of incidence shown in Figure 9. Wavelengths up to 15Å can be used at all angles of incidence above 0.35° as can be seen in Figure 9a, but longer wavelengths than this only illuminate the sample above 1°, as shown in Figure 9b. This means that while pulse-skipping can be used to reduce the number of angles, the minimum Q-value is determined by the longest wavelength at the lowest angle, e.g. 15Å at 0.35° gives a Qmin of 5.1 x 10^{-3} $Å^{-1}$. *This applies to all sample sizes down to 1cm^2.*

a) b)

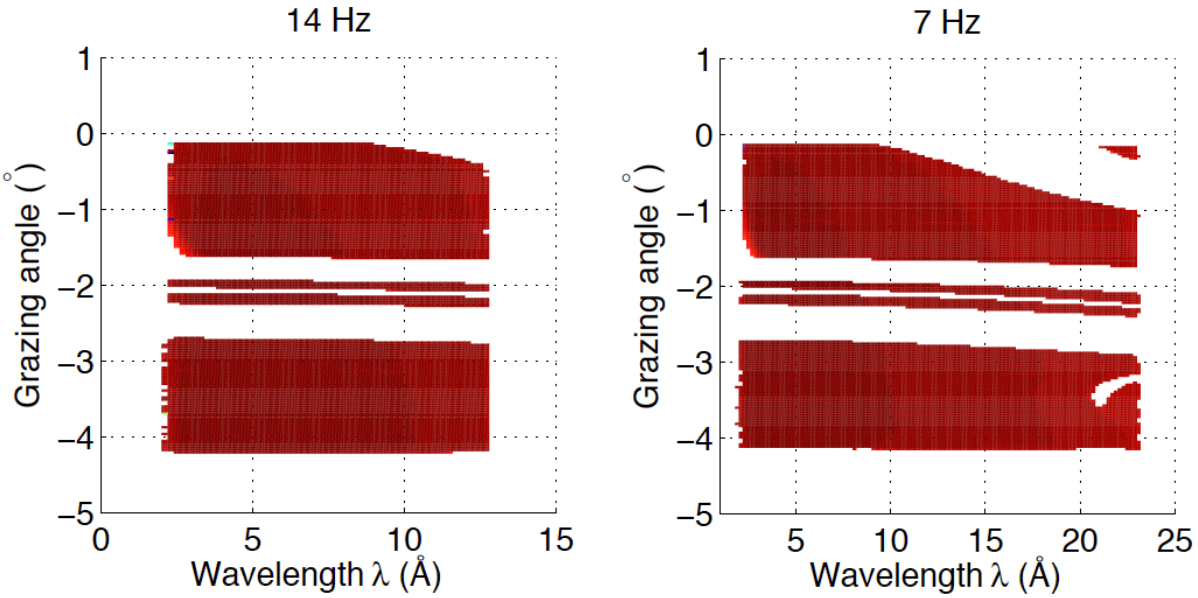

Figure 9. a) Illumination (shown on a logarithmic scale) of the sample area by the full uncollimated beam as function of wavelength and grazing angle showing at 14Hz. The longest wavelengths are beginning to miss the sample above 9.5Å, but only at angles below 0.3°. b) Illumination of the same sample area at 7Hz, showing that the longer the wavelength, the higher the minimum usable angle of incidence is. From 1° up, all wavelengths can be used in the pulse-skipping mode.

In practise the smallest achievable sample footprint is determined by the smallest possible slit opening, which we took to be 30 µm. The simulations were done using a slit-sample distance of 28cm – at this distance the smallest sample that can be under-illuminated with 1.5% angular resolution is 1cm^2. Smaller samples or lower resolutions are possible by placing an additional slit 7cm before the sample. Section 4.1 in the Appendix describes in detail the footprint and slit calculations as well as simulations of the flux with slit-sample distances of 7cm and 28cm.

1.2.3 Wavelength band, Q-range and resolution as function of λ

1.2.3.1 Time-distance diagram

Figure 10 shows the time-distance diagrams for a detector position at 25m corresponding to operating at a) 14Hz within the first frame and b) at 7Hz by skipping every second pulse and measuring across the prompt pulses. The shortest wavelength was chosen considering the worst acceptable resolution (12.4% FWHM for 2.5Å) and the transmission of the multichannel bender described in section 1.2.2.2. The three wavelength band defining chopper pairs WBC1-3, positioned at 6.5m, 10m and 15m are counter-rotating, and allow the relative opening angle to be varied from 0-200° without frame overlap. Their function is described more detail in the Appendix section 5.2.

a) b)

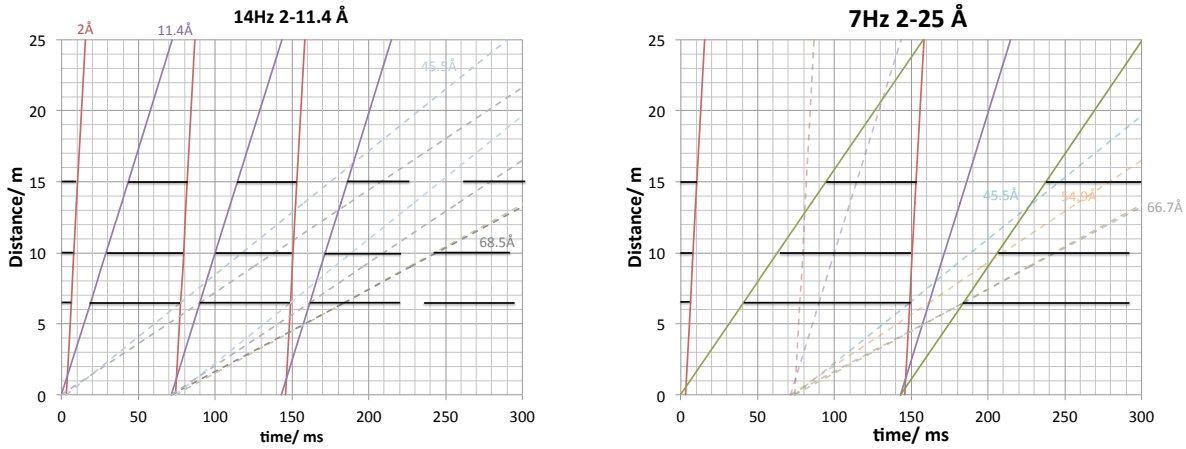

Figure 10. Time-distance diagram for a 25m instrument operating a) in the first frame at 14Hz and at b) 7Hz by skipping every second pulse. The limiting usable wavelength was considered to be 2.5Å with 12.4% FWHM resolution. The chopper positions were chosen so that frame-overlap by up to 70Å neutrons (shown as dashed lines) are avoided with the minimum number of choppers.

a) b)

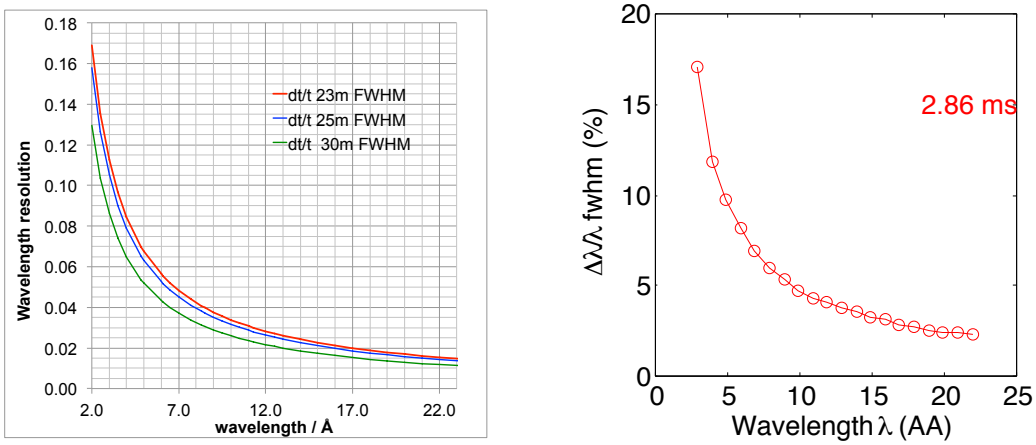

Figure 11. a) Analytical calculation of the full width half maximum (FWHM) wavelength resolution dλ/λ at 23m, 25m and 30m from the source, corresponding to a 2m, 3m and 8m sample-detector distances. b) Simulated dλ/λ (FWHM) at 25m.

Figure 11a shows the calculated relative wavelength resolution dλ/λ considering both the full pulse width as well as a gaussian full width half maximum for 2-23Å at 23m, 25m and 30m from the source, which correspond to the sample to detector distances for specular measurements (3m) as well as the shortest (2m) and longest (8m) GISANS distances. Figure 11b shows the simulated wavelength resolution simulated at 25m. The simulated resolution is somewhat lower than predicted from the 2.86ms pulse width – e.g. for 6Å, dλ/λ is 8.08% (FWHM), as opposed to 7.6%. This results from the pulse tail during which neutrons are emitted at least up to 4ms from the cold moderator, and indicates that the effective pulse length for 6Å is 3.03ms. The detector is movable between 1m and 8m from the sample. At 1m, which may be used for accessing up to Q = 2.25Å^{-1}, the usable wavelength band extends to 12.4Å. At 8m the bandwidth is limited to 2-9.5Å, with the resolution of 2Å being 12.9% FWHM.

At the standard detector position of 25m, the available wavelength band is 2.5-11.4Å within the first frame. The instrument has been optimised to function at 14Hz in a single frame mode. However, provided that measuring during the prompt pulse is possible, the wavelength band can be extended up to 25Å with the limitation to 15Å at small angles, as explained in section 1.2.2.4. The choice of wavelength band was based on the need for the broadest possible simultaneous Q-range.

Figure 12 shows the full uncollimated beam flux at the guide exit after the last slit and on a 4cm x 4cm horizontal sample, as well as the brilliance transfer of the entire instrument. The uncollimated flux on the 16cm^2 area is 1.81 x 10^8 n/s/cm^2, and the brilliance transfer reaches 40% for the longest wavelengths.

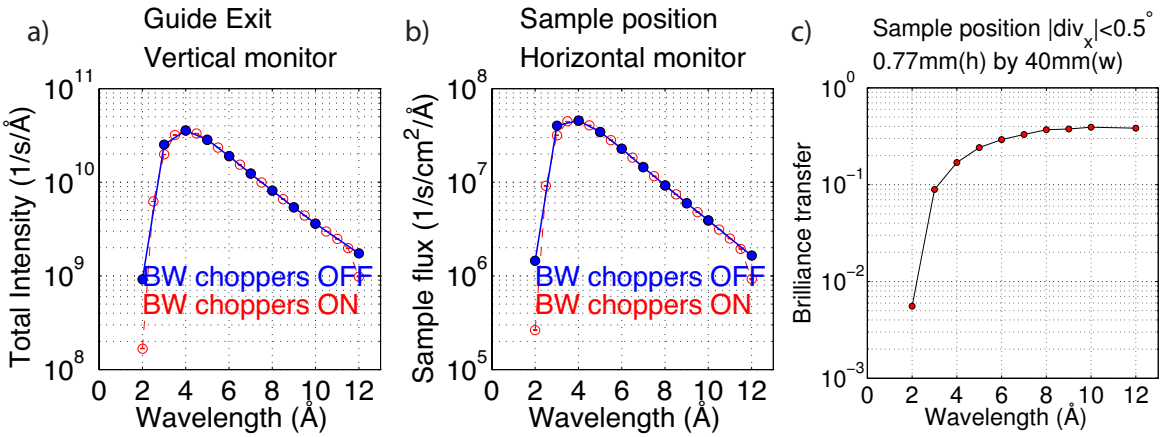

Figure 12 Simulated white beam flux a) at the collimation guide exit and b) on a horizontal 4cm x 4cm sample plotted as n/s/Å/cm^2 vs wavelength, c) the simulated brilliance transfer of the whole instrument over the full vertical divergence range (4°).

Figure 13a shows that it is possible to cover the full Q-range of 0.0065-0.4 Å^{-1} typically required for liquid samples in 3 angles with reasonable overlap ranges (0.01 Å^{-1}). Figure 13b shows that the Q-range on free liquids can be extended to cover 0.0035 < Q < 0.4 Å-1, and gives an example of 5 angles of incidence selected from the divergence available.

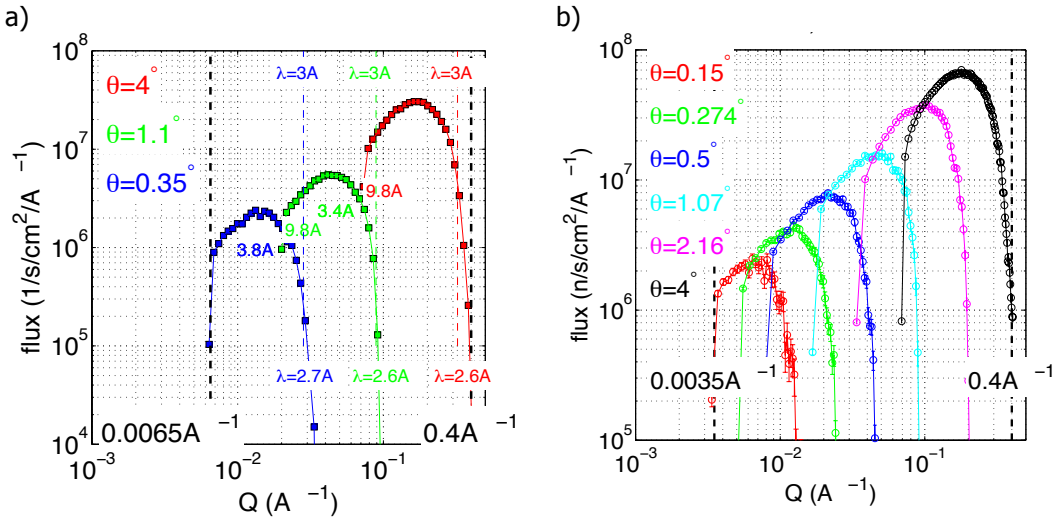

Figure 13. Collimated flux (dθ/θ = 4%) as a function of Q measured on a 4cm x 4cm horizontal sample a) using three and b) six angles of incidence. The wavelengths at the cross-over points are indicated in panel a) as well as 3Å and the lowest usable wavelength (2.6-2.7Å).

Most of the fast kinetics experiments will not need the full Q-coverage, as above Q=0.2 $Å^{-1}$ the signal becomes progressively more and more background limited, leading to long counting times. It can therefore be seen that the choice of three angles for covering kinetic experiments has some flexibility. This will allow the lowest wavelengths to be discarded in cases where their resolution is not sufficient to e.g. resolve minima in the reflectivity profile. Conversely, there may be experiments for which either low Q values are important, such as sapphire-D_2O interfaces (Qc = 0.005 $Å^{-1}$). Low Q_{min} is also desirable for systems that have no critical reflectivity, e.g. films at the air-null reflecting water interface – in these cases the incoherent scattering from the bulk solvent usually prevents measurements above Q=0.25 $Å^{-1}$, and most of the signal is at low Q. In other cases, a high Q_{max} may be of interest for samples with higher reflectivity, e.g. substrates with thick gold or magnetic reference layers. In these cases the low Q limit is only given by the critical angle of the system.

The two gaps in the vertical divergence profile, shown on Figure 7 need to be taken into account in the choice of angles. Figure 14a illustrates the Q-ranges (represented by the orange, blue and green areas) and corresponding wavelength resolutions for three angles that can be chosen to cover the needs of different experiments, using wavelengths above 2.5Å (dλ/λ=10.5% FWHM). The gaps in the divergence profile are indicated by the grey areas. The Q-ranges in the unshaded gaps can also be used in experiments using conventional collimation slits and guide. Higher Q-values are available by rotating the sample/detector for those samples that do not require a horizontal geometry. Thus, the natural resolution of the instrument can be used for a wide range of high flux experiments at medium to low resolution.

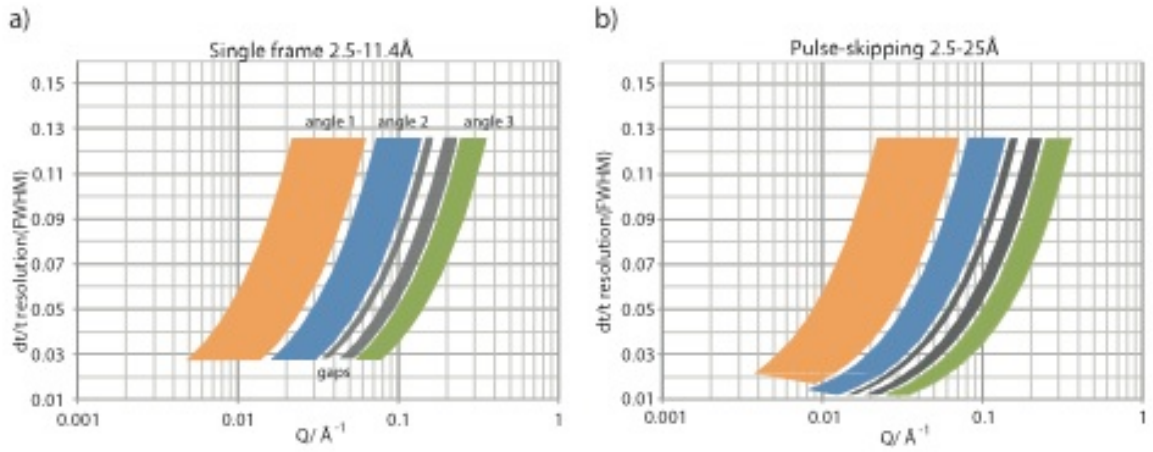

Figure 14. Available Q-ranges for different experiments – a) single-frame experiments using 2.5-11.4Å and b) pulse-skipping experiments using 2.5-25Å. The colored areas represent the three main angular ranges available by using the three-slit collimation for kinetic experiments, while the grey areas indicate the vertical divergence gaps.

1.2.3.2 Pulse-skipping – using longer wavelengths

The wavelength band chopper system can be phased to select the wavelength band at either 14Hz or 7Hz. Pulse-skipping extends the usable wavelength band up to 25Å, assuming that data can be collected during the 2.86ms proton pulse because line of slight to the moderator is avoided twice already at 11.5m, i.e. 10.5m before the sample position. Due to the footprint shift for longer wavelengths described in section 1.2.2.4, the longest usable wavelength varies with the angle of incidence. This does not significantly limit the performance of the instrument, as can be seen in Figure 14b, which shows the available Q-ranges in pulse-skipping experiments. Kinetic experiments in this mode will typically use 1-2 angles of incidence.

1.2.4 Choppers

The instrument includes two chopper systems:

i) three wavelength band defining (WBC) choppers for using the natural resolution of the instrument with possibilities to vary the wavelength range and skip pulses.

ii) 7-fold Wavelength Frame Multiplication (WFM) choppers for constant $d\lambda/\lambda$ =1.5% (FWHM)

The chopping is in all cases done across the 5cm guide width, and preferentially from above the guide. The chopper locations, window heights, radii and frequencies are listed in Table 1.

The wavelength band and frame overlap chopper positions (shown in Figure 10) were optimised to allow both 14Hz and 7Hz operations and to be compatible with the WFM chopper positions. Each WBC consists of a counter-rotating pair whose opening can be varied by the relative phasing of the two discs. The opening angles and times for 14Hz operations and 2.5-11.4Å shown in Table 1. 70Å was taken as the longest simulated wavelength for avoiding frame overlap. The third chopper at 15m is necessary for running at 7Hz, as described in the Appendix section 5.2. A vertical frame-overlap mirror, or a curved horizontal mirror could in principle be used instead of the third chopper, but the third chopper was considered to be a simpler solution than inserting such a mirror inside the elliptical guide.

Table 1. The final chopper configuration for FREIA showing chopper positions, opening angles, frequencies and disc sizes.

Chopper	Position/ m	Frequency/ Hz	Windows	Radius/ mm	Description
WBC1	6.5	14/7	1	375	Double disc
WFM1	6.713	56	7	650	Co-rotating blind pair
WFM2	7.074	56	7	650	
FOC1	8.5	56	7	650	Single disk
WBC2	10	14/7	1	375	Double disc
FOC2	11.1	42	7	650	Single disk
WBC3	15	14/7	1	375	Double disc
FOC3	15.6	28	7	750	Single disk

To increase the wavelength resolution, it is necessary to use WFM to preserve the usable bandwidth, as otherwise the bandwidth of the instrument is limited, e.g. to 1.7Å for a 1ms chopper window opening (due to the earliest possible chopper position being at 6.5m from the source). WFM relies on an optically blind chopper pair to create a sequence of short sub-pulses that are separated in time-of-flight but overlapping in wavelength, which allows a continuous wavelength spectrum to be used in data-reduction. The number of frames required to fill the frame is related to the ratio of the natural instrument length and the actual length of the instrument, with the number of frames increasing for short instruments. The WFM chopper system was optimised according to the method published by M.

Strobl et al[1], and its design and limitations for short instruments with medium resolution and a broad bandwidth are described in the Appendix section 5.2.

Table 2. WFM chopper configuration for 2.5-11.3Å, dλ/λ = 1.38% (FWHM).

Window	1	2	3	4	5	6	7
λ/ Å	2.5-3.97	3.97-5.36	5.36-6.89	6.89-7.94	7.94-9.14	9.14-10.3	10.3-11.3
WFM1	7.32°	9.89°	12.34°	14.66°	16.85°	18.94°	19.98°
WFM2	7.32°	9.89°	12.34°	14.66°	16.85°	18.94°	19.98°
FOC1	17.95°	19.98°	21.91°	23.74°	25.47°	27.12°	28.68°
FOC2	27.88°	28.66°	29.41°	30.12°	30.79°	23.88°	32.03°
FOC3	35.57°	34.06°	32.13°	28.61°	26.26°	24.31°	31.48°

A constant dλ/λ = 2% FW (derived from the full source pulse width), which corresponds to 1.38% FWHM can be achieved using 7-fold WFM as shown in Figure 15. In each frame, the shortest wavelengths originate from the end of the source pulse, and the longest from the beginning, with the pulse width being proportional to the wavelength, giving rise to constant dλ/λ. The resolution is determined by the inter-chopper distance z0, which in this case is 0.364m. To avoid cross-talk between the sub-frames, and contamination from the pulse tail (which extends to 5ms), 3 frame overlap choppers are required to keep the frames apart until they reach the detector. Both the time between frames and the length of each frame become shorter with increasing wavelength.

[1] M.Strobl, M. Bulat, K.Habicht, Nuclear Instruments and Methods in Physics Research A 705 (2013) 74–84, doi: 10.1016/j.nima.2012.11.190.

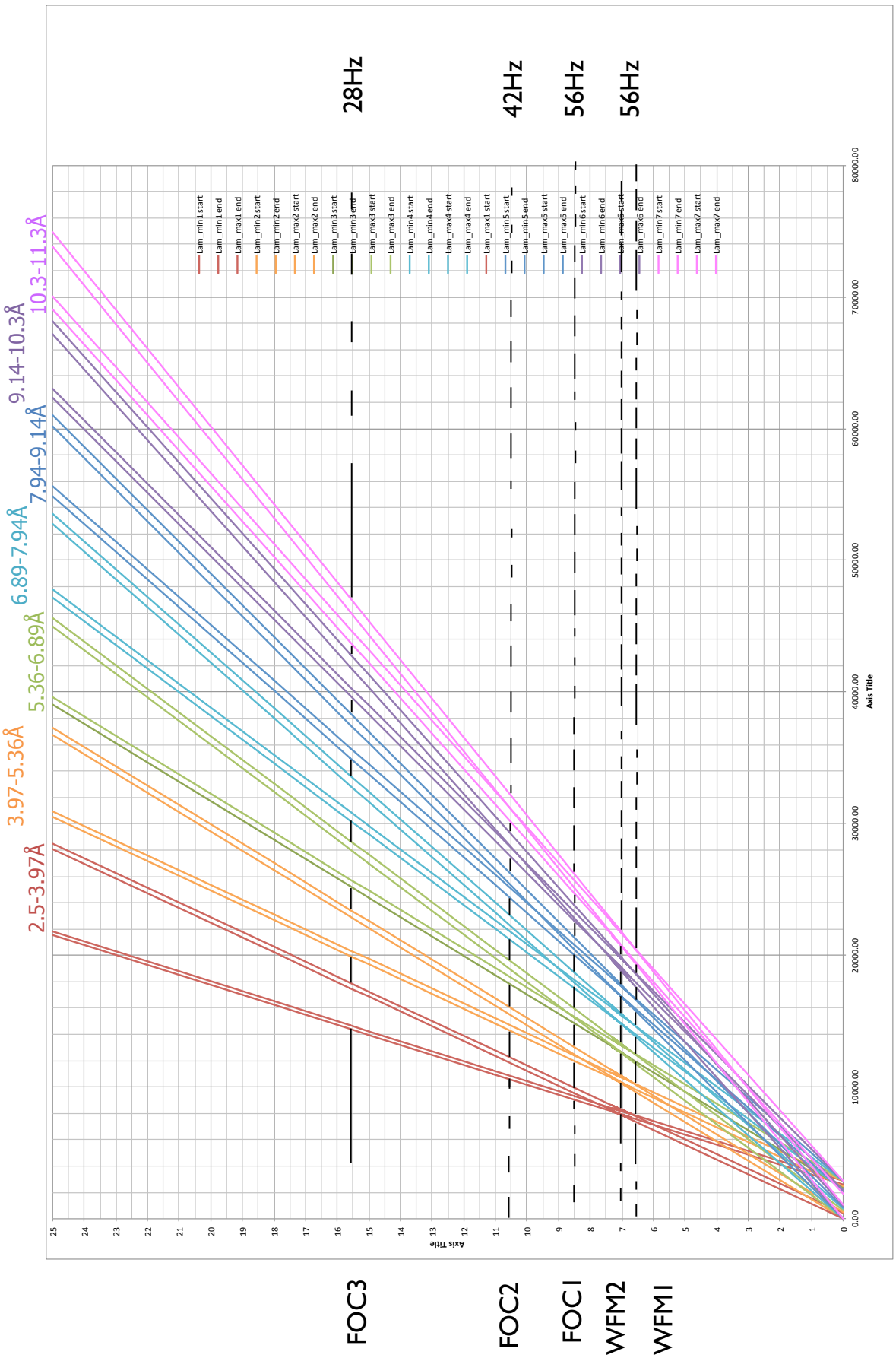

Figure 15. 7-fold wavelength frame multiplication for 2% (FW) = 1.38% FWHM resolution using wavelengths from 2.5-11.3Å.

The final chopper configuration and parameters are shown in Table 2, with Figure 16 showing the time-of-flight of the sub-frames, the wavelength spectrum, and the actual wavelength resolution (FWHM) obtained from the simulations.

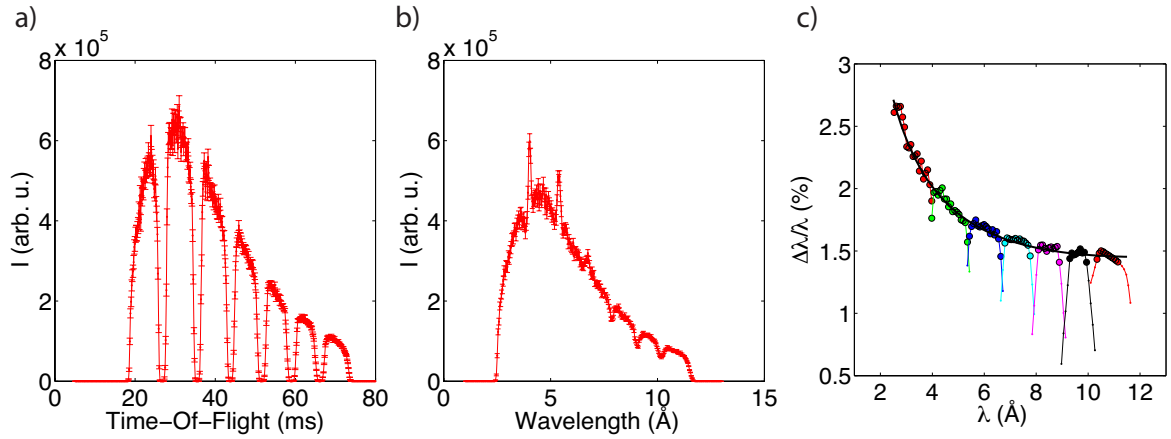

Figure 16. Simulated performance of the WFM choppers using the full guide system – a) time-of-flight and b) wavelength spectrum, simulated at the detector position, c) actual dλ/λ (FWHM) simulated at the detector position.

The resolution of the WFM chopper system shown in Figure 16c was determined from the simulated time-of-flight spread of each wavelength at the detector, with the wavelengths in each sub-frame determined from the simulated time-of-flight from the mid-chopper position to the detector. The details of how this was done can be found in the Appendix sections 4.2 and 4.3. The achieved FWHM resolution varies between 1.5% and 2.5%. For the shortest wavelengths the resolution is somewhat worsened by the limited chopper speed.

1.2.5 Collimation options

Due to the varied experimental requirements, interchangeable collimation guides will be used – using motorised guide sections for this purpose is well-documented (e.g. FIGARO, Platypus). The main collimation options for reflectometry (both specular and off-specular) are illustrated in Figure 17. In addition to these, a horizontally focusing guide for small samples and GISANS collimation will also be available.

1.2.5.1 Three-slit collimation

Three sets of horizontal precision slits, with a common pair of vertical slits are installed at 20m and at 22m. The slit pairs can be stacked within 40mm along the beam direction, which does not affect the angular resolution. Each slit pair will be designed for the required positioning and opening of one the three main angular ranges (as shown in Fig 14a). For angles below 0.3°, a special slit pair will be needed to provide openings down to 5µm, whereas the other slits only require a standard precision of 20 µm. The high precision slits will be driven by piezoelectric positioners, which typically have very high precision and good lifetimes (25% failure in 5.5 years), especially considering that their duty cycle is unlikely to be more than 50%.

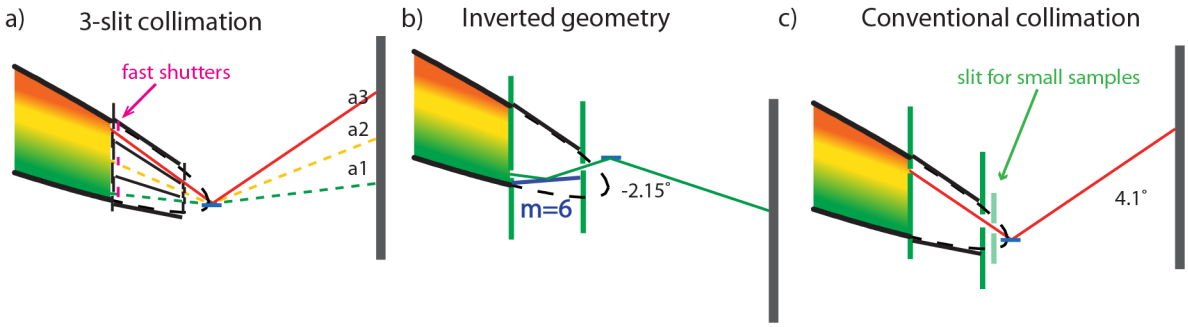

Figure 17. Collimation options: a)Three movable/adjustable slit pairs cover the full angular range of the instrument without moving long distances between measurements. In the kinetic mode, fast shutters placed after the first collimation slits open and close each of the three slit pairs in turn, so that each pulse can arrive at the detector at a specific time and angle, b) the collimated beam can be deflected up by an m=6 mirror to approach the sample from below the horizon at up to -2.15°, c) conventional collimation can be used for both b) and for illuminating small samples that require a slit positioned closer to the sample. A horizontally focusing guide section will also be available for this.

The 2m collimation guide section is split into three or four horizontal channels with 1mm (ideally 0.5mm) absorbing walls to prevent crosstalk between slit 1 and slit 2, so that a second set of fast shutters is not needed. Blocking the cross-talk between the lowest (0.2°-0.5°) and the middle (0.9°-1.3°) angles inadvertently leads to a gap in the divergence profile, but can be positioned in such a way that the effect on measurements is minimized. The effect of such a split guide was simulated for a simple model with 4 equally spaced channels as shown in Figure 18 – this prevents all cross-talk beams, and the additional divergence gaps can be minimized by removing the 3rd (highest) absorber, and by optimising the position and angle of the remaining 2 walls. The simulated performance of the split guide is described in more detail in the Appendix section 5.3.

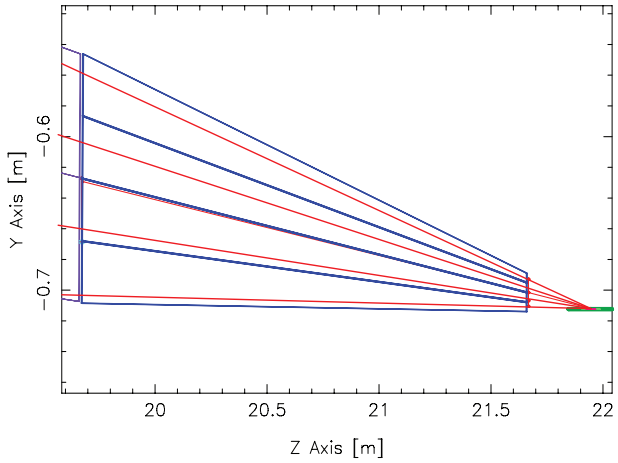

Figure 18. Simulated design of a simple symmetric 4-channel guide to eliminate crosstalk between the three angular settings for kinetic experiments.

The horizontal slit blades will be driven by piezo positioners, which fit in well within the space constraints. Such devices typically have a up to 30N capacity, minimum step size 0.1 µm, use a resistive encoder with a resolution of 0.1-1 µm and repeatability of 0.4 µm. Figure 19 illustrates the arrangement of the triple slit package drawn on a scale that fits in at slit position 2, where the full beam height is 20mm. At slit 1 position, the distances and openings are much larger and conventional stepper motors can be used.

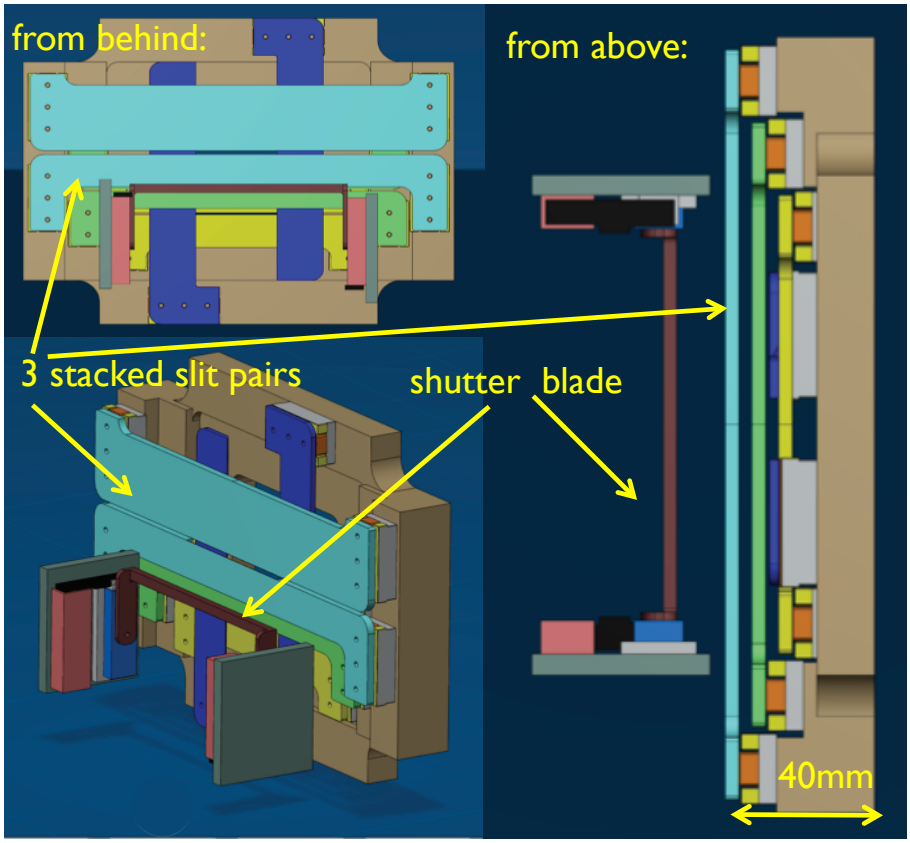

Figure 19. Preliminary concept for the slit packages (slit 2). Three pairs of precision slits and one vertical slit pair are mounted in a stack and are moved piezo positioners. One of the fast moving shutter blades controlled by a voice coil actuator is shown mounted before slit 2 here.

1.2.5.2 Fast shutters for kinetic measurements

A fast shutter mechanism mounted after slit 1 or before slit 2 position selects the angle of incidence as a function of time. One such shutter blade is illustrated in Figure 19, in this case mounted before slit 2. This shutter system needs to attenuate the beam to the same extent as the precision slits when they are fully closed, and to provide sufficiently opening and closing times. The required "open" state of the shutters corresponds to the time from the arrival of the 2.5Å neutrons (15ms) until the arrival of the 11.4Å neutrons (71ms), i.e. 56ms. A concept for three linear, independent shutters has been designed that allows a different opening time to be chosen for each slit according to the expected signal from the sample, with the shortest opening time being 56ms. The shutters are driven by voice coil actuators, which have the ability to reach up to 20G acceleration. Nevertheless, the acceleration/deceleration of a 2-3mm thick and 5mm tall shutter blade easily becomes very high at the short timescales in question. To circumvent the problem of excessive acceleration/deceleration, two solutions were employed. Figure 20 illustrates a solution for operating three shutters in a cycle that repeats at 14/3 Hz. For closing a slit, the shutter blade starts to accelerate at a position of 5mm below the slit edge at t=-28ms, which corresponds to midway through the minimum opening period of the previously open slit (56ms). The shutter begins to close at t=0, and is fully closed at t=15ms, when the 2.5Å neutrons arrive. During the same time 15ms, the shutter for the next slit opens. The closing time for each shutter will always be at least N-1, where N is the number of slits used. Hence, once the shutter completely closes the first slit, it can decelerate for up to 28ms, and stop for the remainder of the time, until the cycle starts at 28ms before the next opening. To allow the 5mm extra travel of the shutter on both sides of the slit, the shutter in this example needs to be 10mm in height. This example, which is for the largest slit and heaviest shutter blade, gives rise to accelerations below 5G, whereas all the others are lighter and need to travel shorter distances.

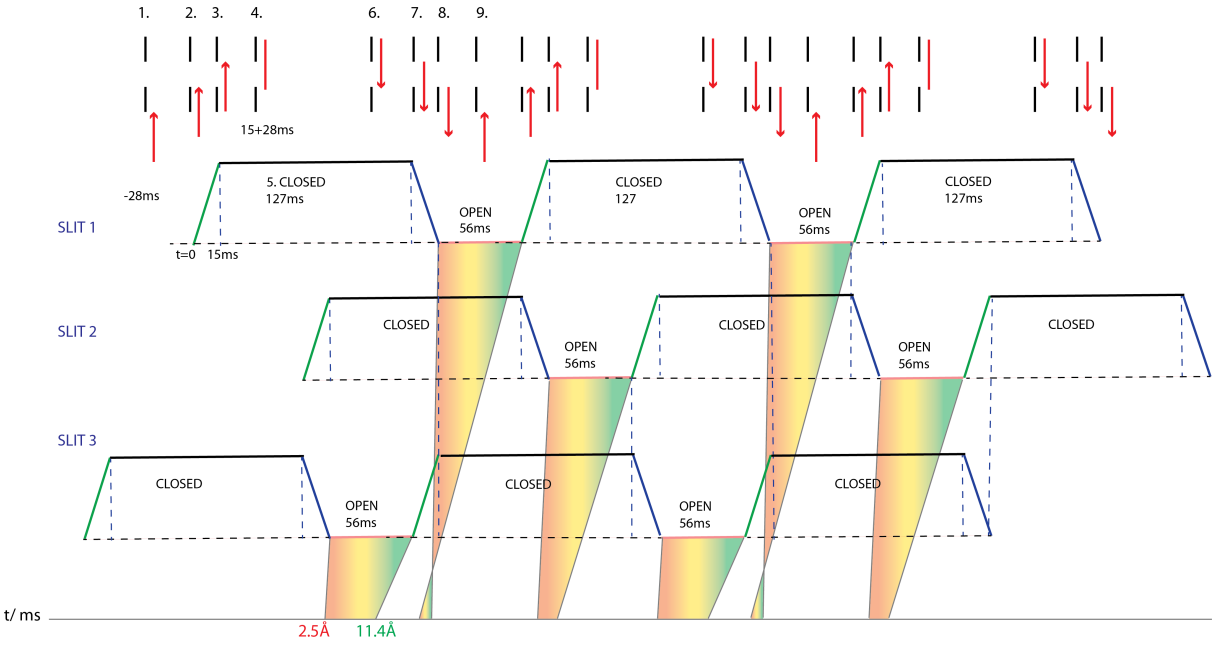

Figure 20. Shutter cycle for operating three slits with an opening time of one pulse each:
1. at -28 ms, the first shutter (red) starts to accelerate up froma position of -5mm
2. at t=0ms, the shutter reaches the lower edge of slit1 gap and starts to close it
3. At t=15ms, the shutter covers slit1 gap completely and starts to decelerate
4. At 15+28ms, the shutter comes to a stop
5. for 2x56ms+15ms = 127ms, the shutter for slit 1 is CLOSED
6. at 71-28ms, the shutter starts to accelerate up
7. at 71ms, the shutter starts to open slit 1
8. at 71+15ms the shutter is fully open, and starts to decelerate
9. in the middle of the 56ms opening, the shutter starts to
accelerate again and the cycle repeats in opposite direction.
The three slits are synchronized so that while one shutter is closing (15ms), the next one is opening, during which time any overlap neutrons are removed by either the choppers, or from the event mode data afterwards.

As a fall-back solution, using an asymmetric Fermi-type cylindrical shutter with 56ms opening time at 4 2/3 Hz is also possible, but this needs up to 30ms cross the beam, and has a fixed open/close ratio. This would work well for slower kinetics where several pulses are acquired at each angle, and e.g. 2/14 can be sacrificed. Clearly the shutter and slit system require development and for this purpose the instrument budget includes 18 man-months for the design, manufacture and testing of these devices.

1.2.5.3 Inverted beam geometry

For accessing horizontal samples from below the interface, a second collimation guide with a deflecting mirror will be used. As the smallest downward angle originating from the elliptical guide is 0.25°, the maximum upwards angle that can be achieved with an m=6 mirror is 2.15°, which gives rise to a Qmax = 0.2 (2.4Å). This is sufficient for experiments at liquid-liquid interfaces in which the sample background and beam attenuation rarely allow for signal observation above this. Although the mirror will have some off-specular scattering, the sample background levels for liquids will always be significantly higher than this. Experience from Platypus at ANSTO shows that in practise the use of such a mirror does not limit the instrument performance. The geometry will also be helpful for other in-situ sample environments that cannot be tilted, such as open cone-plate rheometers. For these measurements the counting times will be approximately twice as long as for those shown in the virtual

experiments in section 1.2.8, due to the 50% intensity loss caused by the additional mirror reflection. Enclosed environments e.g. solid-liquid cells that can be rotated to -4.5° do not need to use this option but can be inverted relative to the undeflected beam. The up-deflection involves extending the range of positions for the highest slit 2 to 44mm relative to the guide axis. This options is compatible with the triple-slit package, but not with the fast shutters and split collimation guide, and the angles need to be selected by the precision slits.

1.2.5.4 Conventional collimation/options for small samples

For those experiments that do not need the three-slit collimation and fast shutters, e.g. small samples or samples with longer measurement times, and the inverted beam geometry, conventional slit collimation is available, and can be used to select any angle of incidence from the beam divergence.

The 28cm slit to sample distance is necessary for accommodating bulky sample environments, but makes efficient illumination of small samples (<2cm long) difficult. For this purpose an additional slit is placed on an optical rail and can be positioned at 7cm before the sample. The counting times for small samples will always be of the order of minutes to hours, and will not require the fast shutters. To further focus the flux on small sample areas, a horizontally focusing guide can be inserted in the collimation section.

1.2.5.5 GISANS collimation

Three additional pairs of slits are inserted at 4m, 6.4m and 8m collimation distances from the sample. Allowing 2cm guide gaps at each position was found to lead to no effects on the vertical divergence profile of the beam, and this arrangement of absorbing slits also prevents side reflections from the guide from reaching the sample. Changing from reflectometry to a GISANS mode will only entail moving these motorised slits into position. The 2m collimation guide options are compatible with GISANS experiments, which can consequently be done in either the normal or inverted beam geometry. The 8m and 4m collimation slits will be housed inside the common shielding bunker (up to 15m), but according to the ESS Neutron Technology division this does not pose significant problems. To match the collimation lengths, the detector will have a variable distance up to 8m from the sample. On a $1m^2$ detector, this arrangement gives rise to a Qy_{min} = 3.3 x 10^{-3} $Å^{-1}$ using 9.5Å at 8m and a Qy_{max} = 1.016 for 3Å at 2m, assuming 10mm/5mm collimation and a beam size of 20mm on the detector. This gives access to probe length scales between 0.6 and 190nm. The angular resolution with a 1mm detector pixel size in this case will be 5%, leading to a relative Qy-resolution (FWHM) of 5.6% (9.5Å) – 9.4% (3Å) at 8m, and a constant dQy/Qy = 5.2% if using the WFM. The longest detector distance can in principle be extended to 10m if deemed necessary, which would increase the maximum accessible length scale (for 9.5Å) to 240nm. The incident beam intensity collimated to an angle of incidence of 0.35° for a 4cm x 4cm sample is 3.1 x 10^6n/s, from which we can estimate that for a 5mm horizontal collimation the direct beam intensity for GISANS measurements at this angle would be 3.9 x 10^5n/s on a 4cm long sample = 1.95 x 10^4n/s/cm^2 if being careful not to overilluminate the sample.

1.2.6 Beam polarisation/analysis

An important boundary condition for a polarising system on FREIA is that it must be integrated in such a way that it does not interfere with the non-polarised operation or performance of the instrument. Due to its small size, a solid-state polarizing S-bender can be inserted between the end of the elliptical guide and the first collimation slit without any effect on the vertical beam divergence. The S-shape leaves the beam direction unchanged and any off-specular scattering from the bender is removed by the collimation slits. As illustrated schematically in Figure 21a, the bender consists of a stack of thin silicon wafers coated on both sides with an m=3.6 Fe/Si supermirror coating and an anti-reflecting Gd/Si coating. For the 2.5-11.4 Å wavelength band, a 6cm long configuration using 150µm wafers is sufficient, and otherwise the device will have a configuration very similar to existing devices designed

at both ILL and HZB[2], and presents therefore a low-risk option. Figure 21b shows a prototype device made for the IN14 spectrometer at ILL - the same configuration can be used for supporting 5cm wide stacks.

a) b)

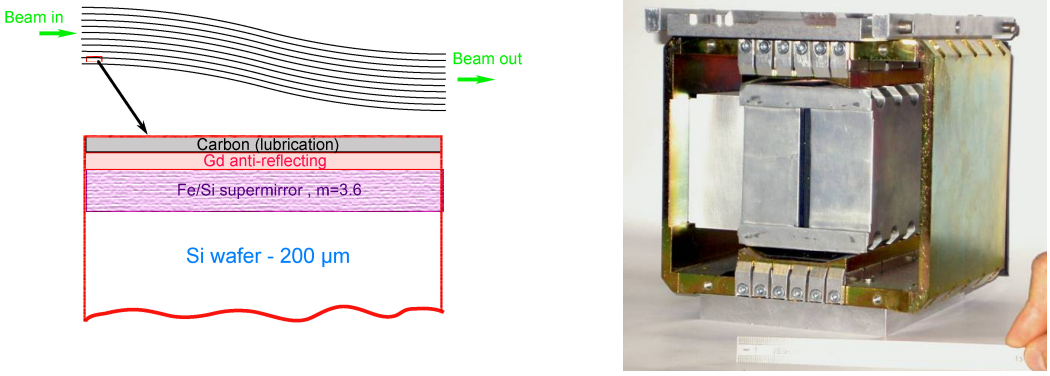

Figure 21. a) Schematic structure of a solid-state polarising bender, b) IN14 prototype from 2006.

The absorption of neutrons in the silicon channels varies between 2% (2Å) and 6% (10Å) per cm, and the polarisation efficiency is up to 98%. A guide field and non-adiabatic spin-flipper are only required around the 2m collimation guide. All interchangeable collimation sections will be housed within their own coils for polarised measurements, which will be moved in with the polarizer according to the geometry needed. Kinetic experiments using the fast shutters, inverted experiments and GISANS can therefore all be done in the polarised mode. Using either a ^{3}He or a supermirror analyser before the detector is possible, the requirements here do not differ from existing reflectometers.

1.2.7 Measurements

1.2.7.1 +/- angular range and implications for moving sample/instrument

The FREIA guide system delivers an angular range of 0.15-4.1° on the sample position, which can be used without moving the sample. The slits and fast shutters are the only parts of the instrument that need to be moved to select particular angles of incidence within this range. This gives rise to the a usable Q-range of $0.0035 < Q < 0.44$ Å^{-1} for free liquid surfaces. For solid or enclosed liquid samples that can be tilted, a 0.5m x 0.5m detector at 1m can be used to measure up to $2\theta=26°$ without displacing the detector vertically, and at 3m up to 9.5°. For GISANS, detector distances up to 8m can be used, but as the angles of incidence are typically below 0.5°, little or no vertical movement of the detector is needed for this. For direct mean measurements at up to 4 degrees, the detector needs a movement of ±200mm at a distance of 3 m from the sample. The corresponding vertical movement of the 8.5m detector tank (if necessary) is ±600mm.

The inverted beam geometry involves moving the sample for each angle of incidence when using the deflection mirror, up to 56mm. The corresponding detector movement down is 130mm at 3m and 350mm at 8m.

1.2.7.2 Data acquisition, treatment and normalisation procedures

Data will be collected in event-mode, allowing the frames to be combined or rejected afterwards. Data-treatment will be done in the conventional way. Normalisation will ideally be done to monitors to

[2] Stunault, A., Andersen,K.H., Roux, S., Bigault, T., Ben-Saidane, K., Rønnow, H.M., Physica B 385-386 (2006) 1152-1154; Krist, Th., Peters, J., Shimizu, H.M., Suzuki, J., Oku, T., Physica B 356 (2005), 197-200.

account for any source fluctuations, which implies that several monitors with different efficiencies are likely to be necessary. Otherwise, a direct beam can be measured at each angle and slit setting. A solution to this will be determined during the first phase of the engineering design. The instrument will have three measurement modes.

1.2.7.3 Kinetic mode using fast shutters

In the conventional mode, successive angles of incidence are recorded using the two sets of precision slits until sufficient statistics have been collected, and the data sets are combined.

In the kinetic mode, three independent fast shutters will open and close three angles in turn, allowing background subtraction from each data set while spanning the full Q-range effectively at the same time, with the time-resolution of the length of the slit cycle. The opening time of each shutter will depend on the experiment, but the design allows opening for a single pulse at each angle, to allow measurements down to 71.42ms at one angle, and thus 214ms for three angles. The event mode acquisition allows any frame-overlap or redundant neutrons between cycles to be discarded. Three angles/shutters and pairs of precision slits have been chosen for practical reasons, as they allow a dynamic Q-range of up to 61.5 to be covered in the range between 0.0035 and 0.44 $Å^{-1}$, by combination of three angles in the ranges 0.15°-1°, 1-2° and 3-4.1°.

1.2.7.4 Stroboscopic mode:

As all data will be acquired in event mode, and the time of arrival for each neutron will be known, measurements of any reproducible process can be cycled until enough counts have been collected at each time-point. If using the kinetic mode on FREIA, the time-resolution of the results will only be dependent on the uncertainty in the neutron emission time from the source. This results in a time-resolution of the order of 200μs at the sample position.

1.2.7.5 Angle-dispersive mode:

For any samples that do not cause a significant off-specular background, it should also be possible to use FREIA in a wide-divergence mode similar to the Estia concept, particularly by using sections of the full 4 degree divergence to extend the simultaneous Q-range at one angle. These options will be investigated in full during the design phase as they also depend on developing a more detailed concept for the slit packages and shutters, and the count-rate capabilities of the detectors available.

1.2.7.6 Minimum Reflectivity

Estimating minimum reflectivity requires knowledge on the general background levels and the shielding options available. We will aim to achieve R = 10^{-7} on liquids, and 10^{-8} on solids, which are standard reflectivities reached on existing reflectometers.

1.2.8 Performance of instrument and virtual experiments using standard samples

The instrument performance was simulated using the full guide system and compared to FIGARO at ILL, which covers the same science case and has variable resolution. The full uncollimated flux on FREIA was simulated to be 1.81 x 10^8 n/s/cm^2 on a 4cm x 4cm horizontal monitor placed at the sample position, which represents the usable flux on a sample of this size. The total flux at the exit of the elliptical guide (5cm x 16cm) was determined to be 1.42 x 10^{11} n/s/cm^2.

Virtual experiments were carried out as agreed at a STAP benchmarking meeting in December 2012. Each sample was simulated using the natural wavelength resolution, as well as with the WFM system with constant dλ/λ =1.5% FWHM, with selected examples shown below (all of the data is available on request). The samples were all simulated using an input data file (simulated in Motofit with 0.001% dQ/Q resolution, zero background and 25000 data points).

The key parameters used were:

- 3Å roughness for all interfaces
- Sample size: this is the collimated illuminated area on the sample (no overillumination)
- Counting statistics: 50 signal counts in lowest statistics bin in the specular region (these points are represented by filled circles, whereas lower statistics points are given a dots)
- A constant incoherent background of 10^{-6} (of the direct beam) for liquids and 10^{-7} for other samples was added, and the error bars corresponding to the statistics when this has been subtracted from the signal are shown.

The definition of statistical errors in McStas and derivation of the counting times and simulated resolution are described in the Appendix section 4.4. Three angles of incidence (0.35°, 1.1°, 4°) were used to collect data in the theoretical Q-range of $0.0065 < Q < 0.4$ Å^{-1}, and in practise the Q-range was limited to obtain similar reflectivities to the experimental FIGARO measurements used for comparison. $d\theta/\theta = 4\%$ and the sample size was 40mm x 40mm in all cases.

The full list of samples simulated is:

SAMPLE 1. Air-D2O
SAMPLE 2. Air-null reflecting water (sld = 0) + 30Å monolayer with sld 4 x 10^{-6} Å^{-2}
SAMPLE 3. Air-Silicon with 15Å SiO2 layer
SAMPLE 4. Air-d-polystyrene (300Å, sld 4.5x 10^{-6} Å^{-2})-SiO_2(15Å)-Si
SAMPLE 5. Air-120Å layer (sld =0) 60% solvent on D2O

SAMPLE 1: Figure 22 shows the reflectivity simulated from the air-D2O interface at the natural instrument resolution, and the simulated resolution as function of Q. The simulated reflectivity reaches 7 x 10^{-7} in 5.2 seconds with similar statistics compared to the same data measured on FIGARO in 1 min. on a sample with approximately twice the area. It should be noted that on FIGARO it takes an additional 1min to move the instrument between the two consecutive angles of incidence. The filled circles in Figure 22a represent data points with at least 50 counts – this data reaches up to 3 x 10^{-6}. The FREIA measurement is 23 times faster, taking into account the difference in sample size.

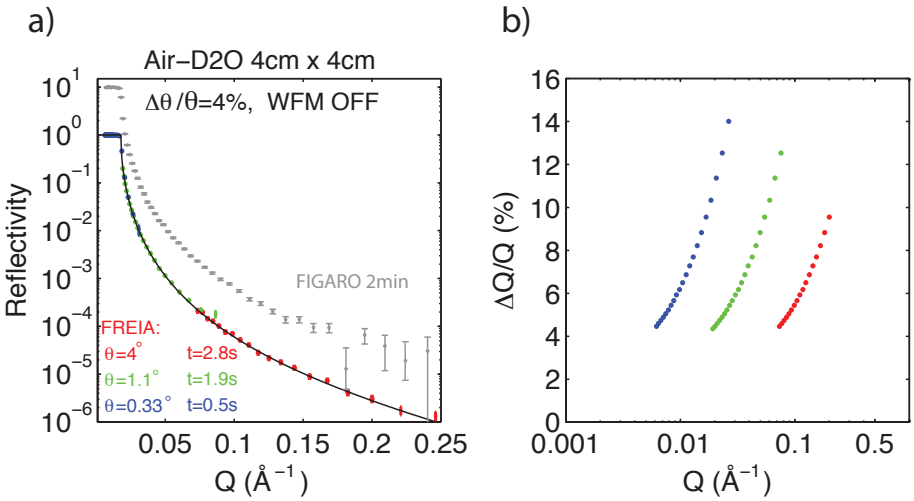

Figure 22. a) Simulated reflectivity from SAMPLE 1: a 40 x 40 mm^2 air-D2O interface and b) the simulated resolution on FREIA. The grey data in a) is recorded with comparable resolution (7.25%) on FIGARO in 1 min + 1 min movement time in 2 angles (0.62° and 3.8°, 2.5-30Å) on a 40 x 80mm sample.

SAMPLE 2: One of the key design features of FREIA is to allow fast kinetic measurements on thin and weakly reflecting films at the air-water interface. Figure 23 shows data simulated from a 30Å deuterated monolayer (of e.g. a polymer or surfactant) on null-reflecting water in air. The estimated measurement time for all three angles down to 2 x 10^{-6} is 6.62 seconds. Panel b in figure 23 shows the estimated time using only one angle of incidence in a limited Q-range to obtain the fastest

possible time-resolution. The data reaches considerably better statistics than in the example of 1s FIGARO data in 350ms (5 pulses). The sample size in the FIGARO example was 30 x 100mm^2. On FIGARO, experiments at these time scales can only be done at one angle at a time, whereas using the fast shutters on FREIA allows the entire Q-range to be covered in 6.62s. Since samples up to 8cm can be illuminated on FREIA, this measurement could be done in 2-3 pulses.

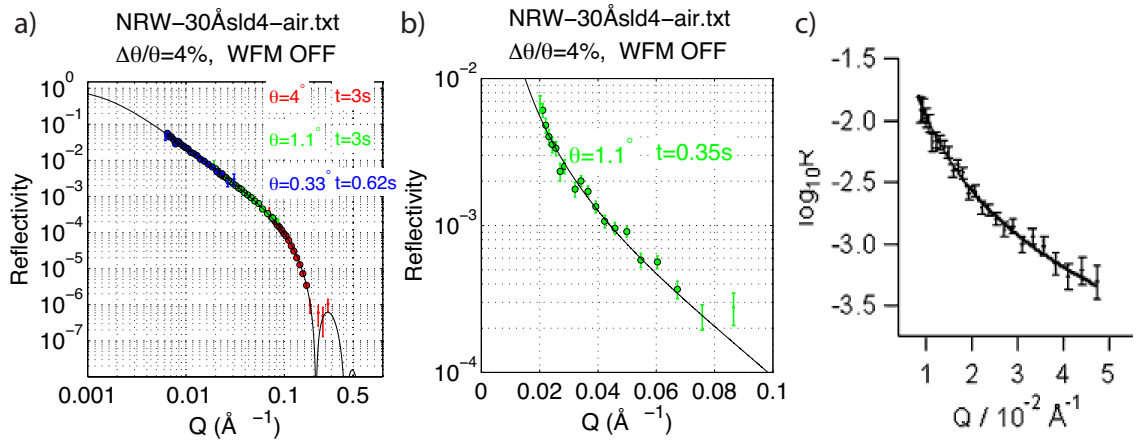

Figure 23. Simulated reflectivity from SAMPLE 2: a 30Å deuterated monolayer (sld = 4.0 x 10^{-6}Å^{-2}) on null-reflecting water (sld = 0) – a) full Q-range with three angles of incidence down to R = 2 x 10^{-6}, b) the middle angle (1.1°) simulated in 350 ms, and c) 1s data from FIGARO recorded at 0.68° with dλ/λ = 7.25% on a larger sample (30 x 100mm^2 15Å monolayer with sld ~6 x 10^{-6}Å^{-2}).

SAMPLE 3: The above two cases are examples where the measurable signal is limited by the incoherent background from the liquid sample (1e^{-6} for D2O). Figure 24 shows the reflectivity from the air-silicon interface with a 15Å SiO_2 layer simulated down to 10^{-7} to compare to routine measurement times for such data. The simulation times using both the intrinsic resolution of FREIA (2min 50.2s) and dλ/λ = 1.5%FWHM (21min 15s) are shown in comparison to data recorded at an intermediate resolution (4.14%) on FIGARO in 2 hours on a 5cm x 8cm sample down to 5 x 10^{-6}.

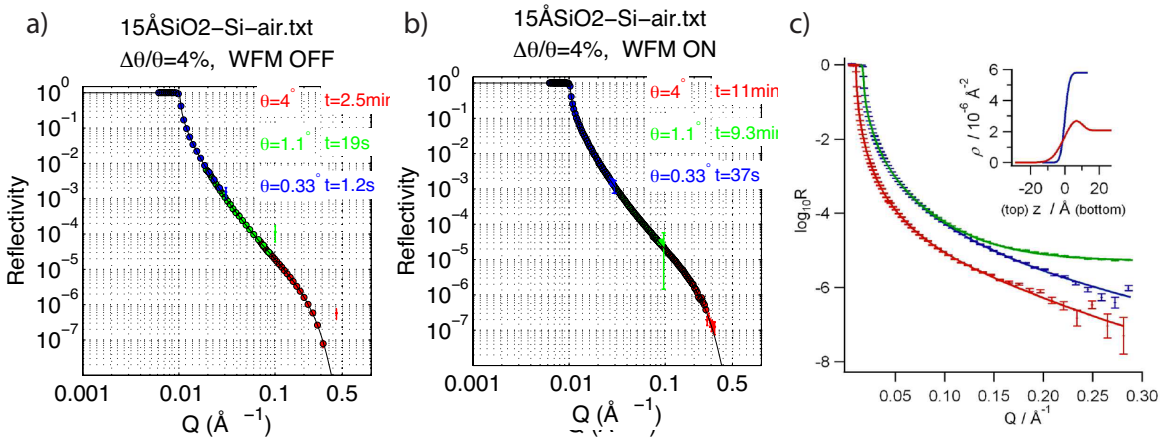

Figure 24. Reflectivity profiles of SAMPLE 3: 15Å SiO2 at the air-Si interface a) at the natural FREIA resolution and b) using WFM (dλ/λ = 1.5%) simulated down to R = 10^{-7} and c) data measured on FIGARO (red curve) using dλ/λ = 4.14% in 2h.

SAMPLE 4: The WFM system was incorporated into the FREIA design to allow higher resolution measurements on thicker films. As an example of this, data simulated from a 300Å deuterated polymer layer (d-polystyrene, sld = 4 x 10^{-6} Å^{-2}) is shown in Figure 25 and compared to the same data simulated using the natural wavelength resolution. Panel c in Figure 25 shows the actual WFM

resolution in the Q-range simulated. It can be seen from Figure 25a that the natural wavelength resolution of FREIA is only useful for measuring the first 3 interference fringes of the 300Å film, but also that the measurement times for the first two angles are an order of magnitude faster so that this could be used for fast kinetics of e.g. thick film swelling. With the WFM resolution and 4% angular resolution giving rise to 3-3.75% Q-resolution, the simulated time to reach 10^{-7} is 21 min 25s.

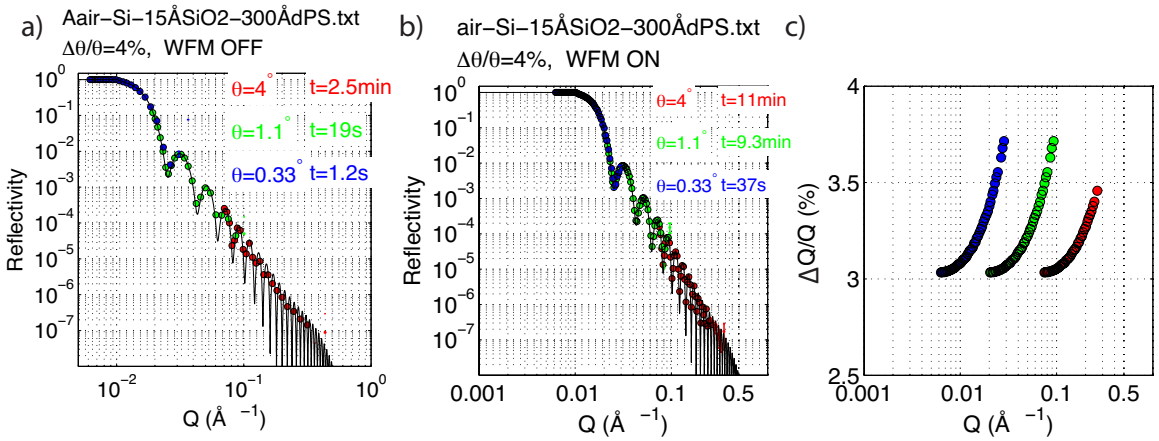

Figure 25. Reflectivity profiles of SAMPLE 4: a 300Å deuterated polystyrene layer on silicon (with a 15Å SiO2 layer) simulated a) without and b) with WFM, with c) showing the actual Q-resolution as function of Q.

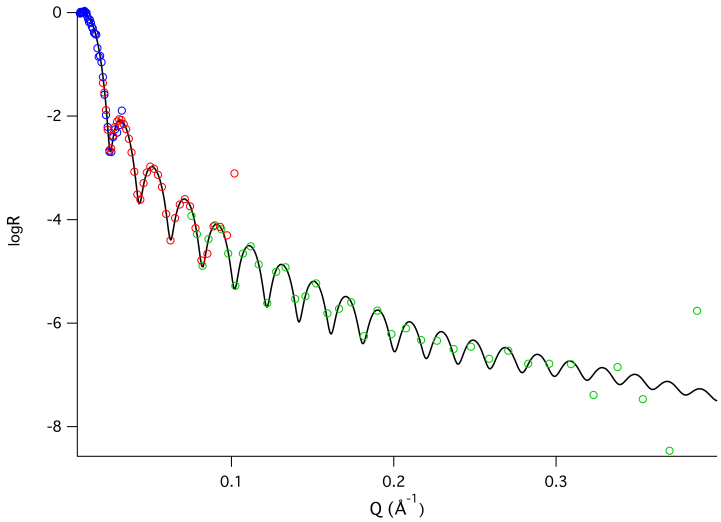

Figure 26. Simulated data from a SAMPLE 4, a 300Å d-polystyrene film on silicon (15Å SiO2) fitted to the original reflectivity model using a constant dQ/Q = 3.4%.

The 300Å d-polystyrene data was fitted in Motofit to the original reflectivity model using a constant resolution of 3.4%, as shown in Figure 26. This corresponds to the average resolution of the experiment.

SAMPLE 5: Finally, a virtual sample with a diffuse 120Å layer (sld = 0, 60% solvent) at the air-D2O interface was simulated to show the effectiveness of the natural wavelength resolution to measure samples with deep interference fringes. Figure 27 shows the data simulated with and without the WFM choppers. It can be seen that the first three fringes can be resolved with the natural wavelength resolution, provided that the angles are adjusted so that the longest wavelengths cover the minima, and the overlap regions are between them.

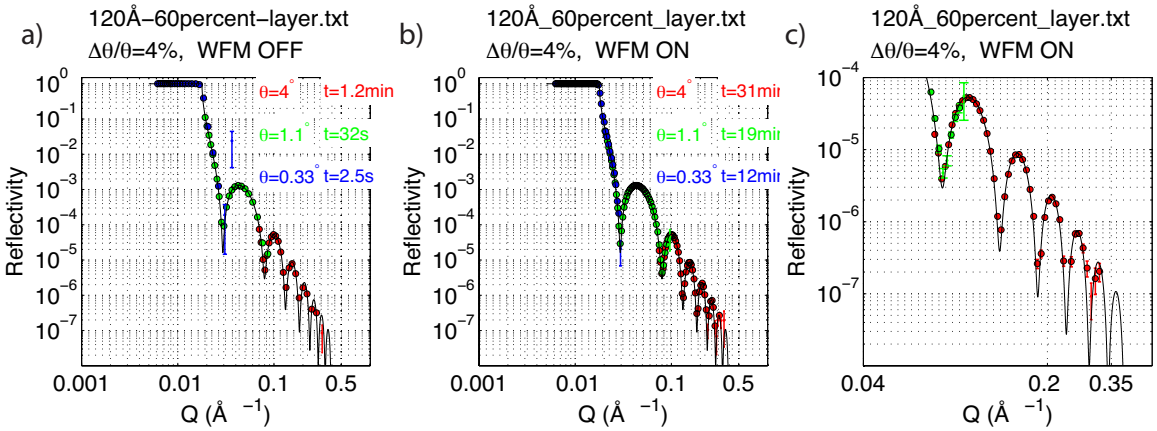

Figure 27. Reflectivity profiles of SAMPLE 5: a 120Å layer with sld 0 and 60% solvent penetration at the air-D2O interface simulated a) without and b) with WFM and c) a zoom at high Q with WFM.

The virtual experiments above were all done with the 40mm x 40mm sample size that FREIA is optimised for, but considering that the flux and wavelength distribution are completely uniform within the central 1cm^2 area (see Figure 10), smaller samples can also be illuminated if using a slit placed closer to the sample. Based on the incident flux on a 1cm^2 area using a slit at 7cm before the sample and 6.8% angular resolution, there is approximately a factor of 35 difference in comparison to the 4cm x 4cm samples if careful not to overilluminate the small sample. Thus, it should be possible to measure a 1cm^2 air-D2O sample to 10^{-6} in 3 minutes, and a 1cm^2 air-Silicon sample to 10^{-7} without WFM in 1h 40 minutes. For larger samples the measurement times should simply scale with the illuminated area. For samples for which a slight overillumination is not a problem (e.g. no sample environment that will cause background), the flux can be increased by a factor 2. The flux comparison and all benchmarking results using SAMPLE 3 (1cm^2 Air-Silicon with 15Å SiO2 layer) shown in full in the Appendix section 4.5 and 4.6.

To summarise, the virtual experiments show that FREIA is applicable to a variety of samples and can be used at both resolutions with more than an order of magnitude faster measurement times than on existing instruments. The uniform flux on sample allows for both small and larger samples to be investigated, and more advanced measurement options using e.g. wider divergence are possible.

A note on pancake moderators

The possibility of increasing the source brightness by using a flat moderator with a reduced height has been suggested and as a part of a study of the instrument suite, the effect of such a moderator on FREIA was investigated. FREIA will be able to use a 2.5-3cm tall moderator, with a flux gain of 2.8 on the sample compared to a 10cm moderator (the maximum is 3.4). This means that the counting times described for all the virtual experiments described in this section can be reduced by this factor, e.g. the 1min 46.5s counting time shown in Figure 7a will be reduced to 38s, and the same sample with WFM from 62 min to 22min 8s. The pancake moderator investigation is described in the Appendix section 5.1.

1.2.9 Functional detector specifications

This instrument can use existing technologies, e.g. a 0.5m x 0.5m ^{3}He-tube detector with 1mm x 8mm resolution, and the price of this detector is not expected to be significantly different to a ^{10}B detector, therefore in the costing only a general estimate obtained from the ESS Detector group was used. The boron technology could however offer an advantage, as it is likely to have enough energy resolution (due to the absorption depth of different wavelengths) to discriminate the inelastic incoherent background from water. The most important criterion for the FREIA detector is the count rate

capability, because the direct beam neutron flux can reach 10^8 n/s on a relatively small area (e.g. 5mm x 500mm).

1.2.10 Feasibility, tolerances and risk management strategy

1.2.10.1 Do you need to measure during the prompt pulse, and what is the cost if you can't?

The instrument is designed to be fully functional and cover its science case using only the first frame. We have followed the advice from the ESS Optics group and go out of line of sight of the moderator twice using two multichannel bender sections. We have been assured that having done this, the prompt pulse should not present problems. In the event that data can be acquired during the proton pulse, the instrument will be able to skip pulses and record data with the longer wavelengths by either using two frames or by working only in the second frame for higher resolution.

1.2.10.2 Feasibility/risks of any new or non-standard components

The main feasibility question relates to the fast shutter system. The ESS motion control group has welcomed the challenge of designing a concept, and the preliminary work suggests that a solution can be developed to allow each angle to be operated by an independent shutter. We expect to test and prototype this system as part of the design phase, and have included 6+12 months of engineering time for this purpose, as the component is specific to FREIA. There is so far no reason to believe that the 15ms/56ms cycling at 14Hz would present difficulties using the solution described in section 1.2.5.2. The proposed shutter solution uses voice coil actuators, which typically have extended lifetimes – it has however not been possible to obtain a reliable lifetime estimate from manufacturers as this requires design and testing of the complete device, which we will start during the early stages of the design phase.

However, if it proves difficult to run such shutters at 14Hz,, the first mitigation strategy will be to relax the condition so that multiple pulses are always measured, and if necessary one pulse before and after are sacrificed - e.g. 5 pulses open out of 7 gives 71% of the flux compared to using every pulse, and an effective time resolution of 500ms per angle and 1.5s for covering three angles. This corresponds closely to the shortest measurement times on the vast majority of samples.

A simple solution that can be used without any additional cost as an ultimate fallback or as a basic start-up configuration is the conventional collimation option consisting of two slit pairs, which can be moved to access any angle of incidence. With typical movement times of 10-15s, this will still be considerably faster than the time needed to move on existing instruments, particularly because liquid samples cannot be accelerated/decelerated fast, and this typically takes at least 1-2 min between angles on a horizontal instrument. 10-15s is sufficient for a large number of processes that take place on the minute time-scale, and also means that very little measurement time is wasted by moving the instrument.

The second main risk relates to the size requirements for the WFM choppers. Informal discussion with Astrium representatives have not identified any insurmountable difficulties as none of the choppers run faster than 56Hz.

1.2.10.3 What are the tolerances? When does the instrument no longer work?

If the WFM system is not found feasible due to the mechanical constraints of the choppers, the instrument will function very well in the high-flux mode for a wide range film thicknesses and fast kinetics and can reach higher resolutions in the pulse-skipping mode. Although this depends somewhat on the ability to use the 2nd frame neutrons, the instrument will be applicable to many kinds of samples where $d\lambda/\lambda max=10.5\%$ is sufficient, as the lowest resolution data can in the vast majority of cases be discarded.

If the fast shutter system proves to be impossible, or is delayed, the instrument will function as a high flux reflectometer with the ability to record the whole Q-range sequentially still without moving the

sample and for non-liquid samples, and pulse-skipping and some of the divergence may be used to expand the simultaneous Q-range in a fashion similar to the Estia concept.

1.2.11 Assumptions made during simulations.

The simulated guides are built of either the component testcomp87.comp written by Henrik Carlsen and Mads Bertelsen or guide_gravity. Gravity is included in the simulations. The optimization of the guide system was conducted within the iFit Data Analysis library written by E. Farhi (http://ifit.mccode.org/). An analytical equation fitted to reflectivity curves from Swiss Neutronics was used to describe the reflectivity of multilayer mirrors (see Appendix section 1.1).

For the elliptical guide components, the same m-coating had to be simulated for both side and top/bottom walls in each section, which means that the side walls still need to be optimized to have a lower m-coating – this will result in improved flux on sample.

1.3 Technical Maturity

Bender section: This is relatively large and expensive – during the design phase, alternative solutions such as solid-state silicon benders will be investigated as a more compact and economical solution.

Elliptical guide: This is not used for point-to-point imaging as in the case of the Selene guide concept, and as such its performance is less sensitive to guide misalignments. Off-specular scattering will be removed by the two slits and collimating guide.

Choppers: The performance requirements are clear from the simulation study. Several of the discs are relatively large due to the large guide size, and there are two 56Hz choppers with 7 windows. Advice has been sought informally from Astrium, who have not indicated that this will be a problem. The engineering solution to this will need early attention during the design phase.

Polarisation system: uses existing technologies and similar to existing solutions - low risk.

Fast shutters: Advice has been sought from both electrical and mechanical engineers at ESS. Suitable technologies exist, but this system will require development. An estimate for the development and prototyping time (18 months) is included in the Design phase.

1.4 Costing

The costing is presented in detail below. Hardware costs generally include components, manufacturing, testing and installation. Most of the costs will be incurred in the Procurement and Installation phases, but some of the major procurements may be initiated in the Final Design phase. *This cost estimate should be regarded as very preliminary and only indicative of the relative cost profile between the various components.* The manpower is estimated in person-months (10 k€/month) and the following categories are included:

Integrated Design: Overall instrument design by the Lead Scientist and engineer, as well as other scientists and engineers involved.

Systems Integration: Systems engineering for compatibility between components and compliance with ESS standards.

Detectors and Data Acquisition: Detector system including electronics. The cost estimate, which includes electronics, beam monitors, and the design work/installation, is based on discussions with the ESS Detector group.

Optical Components: The beam delivery system including the bender, guides, collimation, polarisation and analysis system, guide housing and alignment system, collimation slits and the fast shutter system. The guide cost estimate of 500k€ is based on a confidential market survey by the ESS

Neutron Optics group, assuming that the guide has the same m-coating for all four sides. For the 4+4m bender a quote of 1.94M€ was obtained from Swiss Neutronics as the upper limit for the cost of going out of line of sight twice. The estimate for the slit package and shutter development (100k€ hardware) given by the ESS Motion control and project engineering group also contains 18 person-months to test and prototype this novel system during the Design phase.

Choppers: The estimate from the ESS Chopper group includes all motors, vacuum housings and other infrastructure to operate the choppers.

Detector Vessel: The vacuum vessel for the detector, including pumps, windows, mounting and installation.

Sample Environment: Goniometers, rotation and translation stages for mounting samples and specific sample environment such as liquid troughs, flow cells, sample changers, controlled atmosphere boxes etc.

Shielding: Shielding for radiation protection and background reduction, including shutter systems and instrument cave. The estimate is based on guidelines from the ESS Optics group (1.5 times the cost of the guide system, for a straight guide with the same m in place of the bender).

Instrument Specific Support Equipment: This includes mechanical components not costed elsewhere.

Instrument Infrastructure: The buildings and facilities not provided as part of the Conventional Facilities budget, such as cabins, mezzanines, raised floor areas etc. As no definite floor plan exists at the moment, the estimate here is based on information from last year's instrument proposals.

in k€	Phase 1 (Design and Planning)			Phase 2 (Final Design)			Phase 3 (Procurement and Installation)			Phase 4 (Beam Testing and Cold Commissioning)			Total			
	Hardware	Staff (k€)	Staff (months)	Hardware	Staff (k€)	Staff (months)	Hardware	Staff (k€)	Staff (months)	Hardware	Staff (k€)	Staff (months)	Hardware	Staff (k€)	Staff (months)	Staff (years)
Integrated Design	0	420	42	100	720	72	0	480	48	0	240	24	100	1860	186	15.50
Systems Integration	0	0	0	0	30	3	0	120	12	0	60	6	0	210	21	1.75
Detectors and Data Acquisition	0	60	6	0	60	6	1200	30	3	200	120	12	1400	270	27	2.25
Optical Components	0	60	6	0	60	6	2500	30	3	20	60	6	2520	210	21	1.75
Choppers	0	60	6	100	60	6	2500	30	3	50	30	3	2650	180	18	1.50
Detector Vessel	0	30	3	0	30	3	1000	30	3	0	10	1	1000	100	10	0.83
Sample Environment	0	0	0	0	30	3	500	10	1	200	60	6	700	100	10	0.83
Shielding	0	30	3	0	60	6	3750	60	6	20	60	6	3770	210	21	1.75
Instrument Specific Support Equipment	0	0	0	0	30	3	100	120	12	20	30	3	120	180	18	1.50
Instrument Infrastructure	0	30	3	0	30	3	100	60	6	20	30	3	120	150	15	1.25
Total	0	690	69	200	1110	111	11650	970	97	530	700	70	**12380**	**3470**	347	28.92
Grand total (no VAT)	**15850**															

2 LIST OF ABBREVIATIONS

Abbreviation	Explanation of abbreviation
WFM	**Wavelength frame multiplication**
WBC	**Wavelength band chopper**
FOC	**Frame overlap chopper**
PNR	**Polarised neutron reflectometry**
LOS	**Line of Sight**
NR	**Neutron Reflectometry**

PROPOSAL HISTORY

New proposal:	(yes/no)
Resubmission:	(yes/no)

APPENDIX: FREIA

Anette Vickery and Hanna Wacklin

March 21, 2014

Contents

1 How direct line of sight of the guide entry is avoided **2**
1.1 Reflectivity . . . 2
1.1.1 Critical angle of reflection . . . 2
1.1.2 Reflectivity model for a supermirror . . . 2
1.2 Curved neutron guide, bender . . . 3
1.3 Bender design for FREIA . . . 4

2 Neutron guide system and beam transport **5**
2.1 Brilliance transfer of the mirror guide and bender . . . 5
2.1.1 Effect of bender channels . . . 6
2.1.2 Effect of bender curvature . . . 6
2.2 Brilliance transfer of the complete guide system . . . 7

3 Usable wavelength range **7**
3.1 Estimated available Q-range . . . 7

4 Virtual experiments **9**
4.1 Angular resolution . . . 9
4.1.1 Defining the grazing angle at the sample . . . 9
4.1.2 Correspondence between simulated and nominal angular resolution . . 9
4.1.3 Correspondece between simulated and nominal sample illumination . . 11
4.2 Conversion of time-of-flight WFM data . . . 11
4.3 Wavelength- and Q-resolution, WFM data . . . 12
4.4 Estimation of counting times and derivation of virtual data from simulations . 14
4.4.1 Real vs simulated data . . . 14

4.4.2 Counting time and data quality 15
4.4.3 Estimating the appearance of a "real" data set 15
4.5 Sample flux 15
4.5.1 Comparison of flux - Model A, B 17
4.6 The standard sample simulation 19

5 Other simulations **21**
5.1 Pancake moderator 21
5.2 Choppers 27
5.3 Cross talk between collimation slits 33
5.4 The elliptical guide optimization strategy 35
5.5 optimizing the distribution of intensity vs grazing angle at the sample position 35

1 How direct line of sight of the guide entry is avoided

As discussed in the proposel the simulated instrument has the mirror guide (2.5 m long) and the first 7 m of the elliptical guide included in a 4 channel bender (of total length 9.5 m) with radius of curvature 56 m. With a guide width of 50 mm, this eliminates twice the direct line-of-sight of the guide entry by 11.5m from the moderator. Sec. 1.3 outlines the bender design implemented in the instrument simulations. Sections 1.1 and 1.2 contain a short explanation of the theory which forms the base of Sec. 1.3 .

1.1 Reflectivity

1.1.1 Critical angle of reflection

If a mirror has a critical scattering vector of length $m\,Q_{\mathrm{Ni}}$, neutrons with wavelength λ have a critical angle of reflection,

$$\alpha_c = \frac{m\,Q_{\mathrm{Ni}}\,\lambda}{4\pi}\,. \tag{1}$$

where $Q_{\mathrm{Ni}} = 0.0217$ Å^{-1} is the critical scattering vector of Ni. The critical angle is proportional to the wavelength and for realizable m values, $\alpha_c < 2^\circ$ for $\lambda < 2$ Å. Figure 1**A** shows the critical angle as function of wavelength for different values of m.

1.1.2 Reflectivity model for a supermirror

The simulations utilize an analytical model for the reflectivity R of a supermirror which is in accordance with the reflectivity curves from state-of-the-art mirrors provided by Swiss

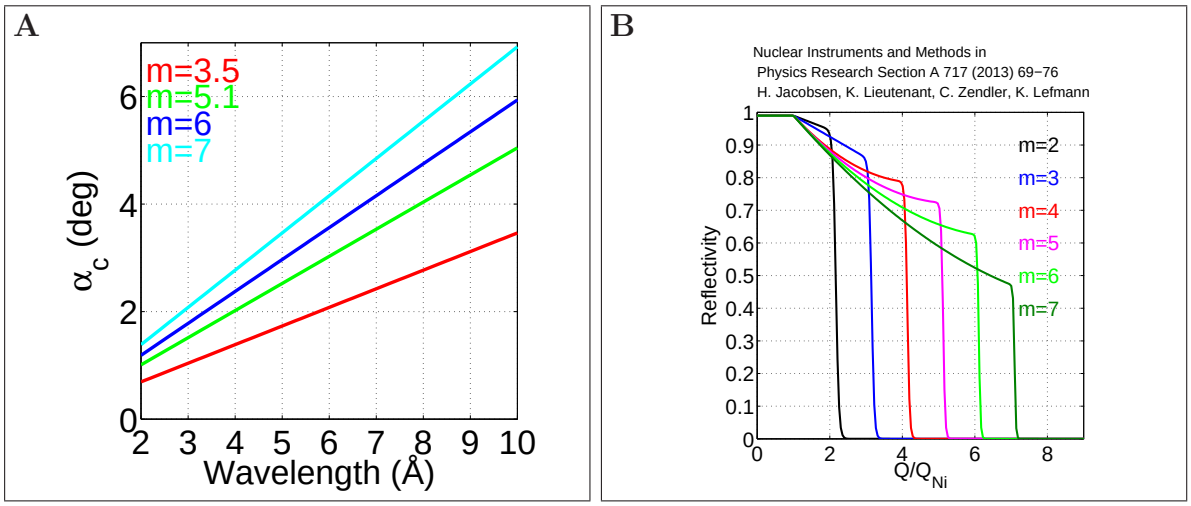

Figure 1:
A: The critical angle of reflection for different m values.
B: Reflectivity curves of supermirrors. The scattering vector is normalized to the critical scattering vector of Ni, $Q_{\mathrm{Ni}} = 0.0217$ Å^{-1}. The model for supermirror reflectivity implemented in the updated version of McStas 2.0.

Neutronics[1]. For scattering vectors $q > Q_{\mathrm{Ni}}$ we define $\arg = \frac{(q - mQ_{\mathrm{Ni}})}{W}$. The reflectivity of a supermirror can then be modelled according to

$$R(q > Q_{\mathrm{Ni}}) = \frac{R_0}{2}\left(1 - \tanh \arg\right)\left(1 - \alpha\,(q - Qc) + \beta(q - Qc)^2\right) \tag{2}$$

where $R_0 = 0.99$. By fitting the reflectivity curves by Eq. 2, the authors found that the values of α, β and W depend approximately linearly on m. Figure 1**B** shows Eq. 2 with α, β and W derived from the fits.

1.2 Curved neutron guide, bender

A straight neutron guide with a rectangular cross section that is fully illuminated by the source will transmit a beam with a square divergence of full width $2\alpha_c$ in both the horizontal and vertical directions, that is, the transmitted solid angle is proportional to λ^2, see Eq. 1. In a curved guide there are two possible types of reflection, called garland and zig-zag reflections. Garland reflections involves only the outer wall of the curved guide. Fig. 2**A** shows that for a guide of width w and radius of curvature R, the characteristic angle of reflection is

$$\theta^* \approx \sqrt{2w/R}\,. \tag{3}$$

If $\theta^* > \alpha_c$ neutrons are transmitted by garland reflections only. The direct line-of-sight length is

$$L^* = 2R\theta^* = \sqrt{8wR}\,, \tag{4}$$

which can be reduced by subdividing the guide into a number of narrower channels, each of which acts as a mini-guide. The resulting device is often referred to as a neutron bender. The

[1]H. Jacobsen, K. Lieutenant, C. Zendler, K. Lefmann: Nuclear Instruments and Methods in Physics Research Section A 717 (2013) 69-76

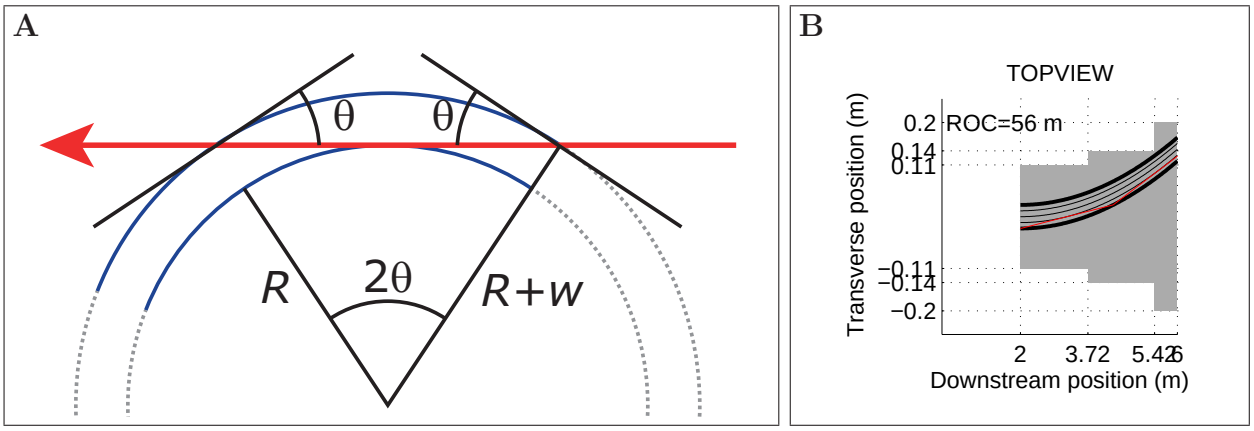

Figure 2:
A: The arrow indicates the flight path of a neutron entering a curved guide with width w. The guide curves to the left with the radius of curvature R. Here we consider the limiting case, where the neutron just glances of left wall. Due to the curvature, the neutron will hit the right wall at an angle θ. From the sketch it is clear that $\cos\theta = R/(R+w) \approx 1-\theta^2/2$, and therefore $\theta \approx \sqrt{2w/R}$. The length of the corresponding scattering vector is $q = (4\pi/\lambda)\sqrt{2w/R}$. To scatter the neutron, we need $q \leq mQ_{c,\mathrm{Ni}}$, so the shortest wavelength which can be transported by the guide is $\lambda_{\min} = \frac{4\,\pi}{mQ_{c,\mathrm{Ni}}}\sqrt{\frac{2w}{R}}$. The neutron is reflected at the distance $R2\theta$ from the guide entrance. The transmission of a bender relative to straight guide segment with the same coating and number of channels.
B: *TOPVIEW*. To avoid the direct line of sight of the guide entry, the first 9.5 m of the guide system is combined with a 4 channel bender of width W =5 cm. Here is only shown the first 4 m of the bender which is within the beam extraction unit. The radius of curvature is 56 m.

transmission of a bender of length L^* compared to a straight channeled guide of same length and m-coating amounts to 67%[2].

1.3 Bender design for FREIA

Please note that in this section we denote by R_B the bender radius of curvature to avoid confusion when the reflectivty of a supermirror R is introduced in the calculations.

The minimum radius of curvature is limited to 56 m by the baseline design of the beam

[2]ILL Neutron Data Booklet, Second Edition

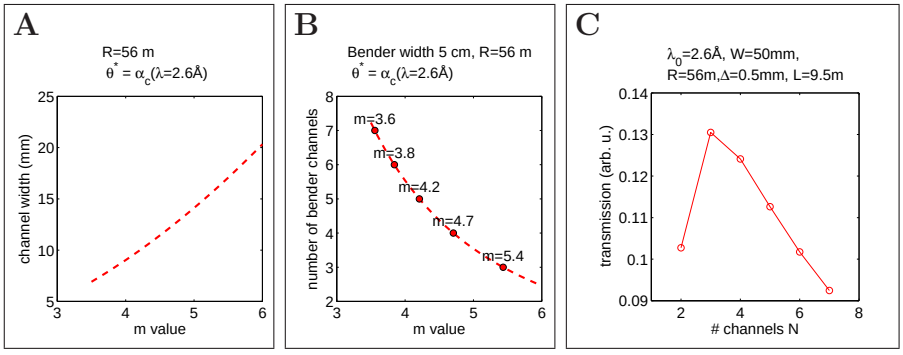

Figure 3: The bender must transmit a wavelength band starting at 2.6 Å, so we require that θ^* is equal to the critical angle of reflection α_c for $\lambda = 2.6$ Å.
A: Calculated bender channel width as function of m value.
B: Calculated number of bender channels as function of m value for a total guide width of 50 mm.
C: Rough analytical comparison of the transmission of 2.6 Å neutrons as function of number of bender channels.

extraction unit Fig. 2**B**. With a guide width of 50 mm, the direct line-of-sight length is calculated by Eq. 4 to $L^* = 4.73$ m. Therefore, one way of eliminating the direct line of sight of the guide entry twice, is by including the first 9.5 m of the guide system a bender with a radius of curvature 56 m.

The bender must transmit a wavelength band starting at 2.6 Å, so we require that the bender characteristic angle θ^* is equal to the critical angle of reflection α_c. From Eq. 1 and Eq. 3 we get the channel width

$$w_{\mathrm{ch}} = \frac{R_B}{2}\left(\frac{m\,Q_{\mathrm{Ni}}\lambda}{4\,\pi}\right)^2. \tag{5}$$

Fig. 3**A** shows Eq. 5 for $\lambda = 2.6$ Å, $R_B = 56$ m and $Q_{\mathrm{Ni}} = 0.0217$ Å^{-1} as function of m value. Fig. 3**B** shows the equivalent number of bender channels assuming a total guide width of 5 cm. As the number of reflections taking place in the bender is proportional to the number of bender channels, it is of interest to limit the number of channels. However, as shown in Fig. 1**B**, the reflectivity decreases with increasing m value.

We made an analytical estimate of the optimal number of bender channels. A neutron passing through a bender of length L and total width W undergoes a number of garland reflections N_G. The minimum value of N_G is estimated from the bender length, width W, the radius of curvature R_B and the number of channels N:

$$N_{G,\mathrm{min}} = \frac{L}{L^*} = \frac{L}{\sqrt{8R_BW/N}} \tag{6}$$

We assume that the transmission of 2.6 Å neutrons is proportional to α_c and the reflectivity at the critical angle $R(\alpha_c)$ to the power of $N_{G,\mathrm{min}}$. Theoretically $R(\alpha_c)$ amounts to 2/3, however as shown in Fig 1**B**, the reflectivity at the critical angle may be substantially different from 2/3 and varies strongly with the m-value. Further, the transmission is proportional to the efficient width of the bender. The efficient width of the bender amounts to Nw_{ch}. This width can be calculated by assuming that the bender walls have a finite thickness Δ, so $w_{\mathrm{ch}} = (W - (N-1)\delta)/N$. Figure 3**C** shows this crude estimate of the bender's ability to transport 2.6 Å neutrons, and suggests that the optimum number of bender channels is 3 or 4. Increasing the assumed thickness of the bender blades to 1 mm does not change this result.

The simulations of the bender brilliance transfer as function of m-value and number of channels are included in Sec. 2. The simulations confirm the analytical calculations: the optimum number of bender channels is 4 when the bender radius of curvature is 56, the total bender width 50 mm and the length 9.5 m. The simulated blade thickness is 0.5 mm. The optimal coating of the outer bender walls is found to be m=4.4. Other simulations (not included) show that the optimal supermirror coating of the inner bender walls is m=2.5.

2 Neutron guide system and beam transport

2.1 Brilliance transfer of the mirror guide and bender

The mirror guide starts at 2 m from the moderator face and the entry has dimensions 5 cm (w) by 10 cm (h) and is centered at the ESS cold moderator horizontally. Vertically the guide

entry center is 3 cm below the cold moderator center.

The simulations utilize an analytical model for the supermirror reflectivity curve shown in Fig 1**B**. We compared the performance of a mirror/bender unit built of elements of lengths 14 cm, 7 cm and 3.5 cm. The performance is very close to identical, so the simulations are done with elements of length 15 cm.

The brilliance transfer is derived from 2 identical divergence sensitive monitors. One is placed at the bender entry 2 m from the moderator, the other is placed at the bender exit at 11.5 m from the moderator. As the bender is inclined 2°, the vertical distribution of intensity in the bender is nonuniform. To account for the intensity distribution, the monitors are 1 cm wide 15 cm tall. Vertically we integrate over a divergence range of width 1.54°, the critical angle of reflection for a m=6 mirror. The divergence range starts from $-\theta_{\mathrm{mirror}}$. In the horizontal plane we integrate over a divergence range from $-1.54°$ to 1.54°.

2.1.1 Effect of bender channels

If a neutron ray bounces once in a straight guide of length L and width W, this ray may be reflected at a distance between $L/2$ and L from the guide entry, and the angle of reflection θ is in the interval between $2W/L$ and W/L. If the same ray enters a straight guide with N channels, it is reflected after the distance

$$d = \frac{W}{N\,\tan\theta} \approx \frac{W}{N\,\theta}\,, \tag{7}$$

so the number of reflections amounts to

$$N_{\mathrm{reflections}} = \frac{L}{d} = 2N \quad \text{for} \quad \theta = 2W/L\,, \tag{8}$$

and

$$N_{\mathrm{reflections}} = \frac{L}{d} = N \quad \text{for} \quad \theta = W/L\,. \tag{9}$$

Since the transmission scales with R^N it is clear that the brilliance transfer decreases with increasing number of guide channels (*in a straight guide with channels*). Figure 4**A** shows the simulated brilliance transfer of 2.6 Å neutrons through a 9.5 m straight guide otherwise similar to the proposed bender. The first 4 m of the side walls have a super mirror coating with the m-value varying according to the values shown on the x-axis. The last 5.5 m of the simulated guide has constant m=3. We see that the brilliance transfer decreases with increasing number of guide channels, in accordance with Eq. 8, 9.

2.1.2 Effect of bender curvature

When the bender characteristic angle is less than or equal to the critical angle for 2.6 Å neutrons, the transmission of a bender of total length L will scale with $0.67^{L/L^*}$ compared to a straight guide with same number of channels, see Fig. 2**B**. L^* is the line-of-sight length of one channel. The longer wavelengths will have better transmissions. For a 50 mm wide bender with 4 channels the ratio $L/L^* \approx 4$, so the brilliance transfer of 2.6 Å neutrons is

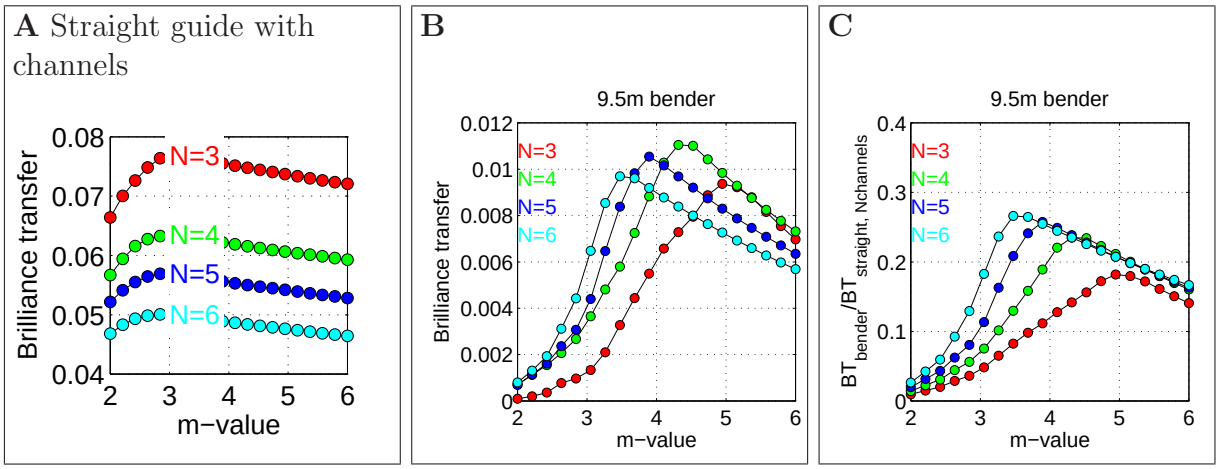

Figure 4: **A**: The brilliance transfer of a straight guide with N channels. The top/bottom of the guide walls are identical to the proposed instrument. The first 4 m of the guide has supermirror coating varying according to m-value on the x-axis. The remaining 5.5 m guide has a constant supermirror coating with m-value 3.
B The brilliance transfer of benders with N channels, radius of curvature 56 m and total width 50 mm.
C: The ratio of the brilliance transfers **B** and **A**.

expected to amount to approximately 20% of a straight guide with same number of channels. Fig. 4**B** shows the simulated 2.6 Å brilliance transfer of a 9.5 m benders with $R_B = 56$ m and different number of channels. As expected from Sec.1.3 the optimal number of bender channels is 4. Fig. 4**C** compares the brilliance transfers shown in Fig. 4**B** with *the simulated brilliance transfers a straight guide with same number of channels*, i.e. Fig.4**A**. We see that the maxima of the simulated brilliance transfers *ratios* scales approximately with $0.67^{L/L^*}$ as expected.

2.2 Brilliance transfer of the complete guide system

The instrument is designed for horizontal samples of length 40 mm. For that reason the instrument is designed to focus a wide range of (vertical) divergence (0° to 4°) to the sample position. It is therefore relevant to derive the brilliance transfer from monitors with a height similar to θ×40mm, where θ is a typical grazing angle used in the experiments. The monitor widths are 40 mm. Fig. 5**A** shows the brilliance transfer of neutrons from the guide entry to the sample position. The results shown here are simulated with monitors of heights $\sin(1.1\text{deg}) \times 40\text{mm}$=0.77 mm. The brilliance transfer derived from monitors with heights $\sin(0.35\text{deg}) \times 40\text{mm}$ and $\sin(3.7\text{deg}) \times 40\text{mm}$ is identical.

3 Usable wavelength range

3.1 Estimated available Q-range

The shorter wavelengths (< 3.3 Å) will illuminate only partly the lower part of the ellipse, so these wavelengths will to some extend be missing in the lower range of grazing angles, that is from 0° to 2.14°. However, considering that the Q-range covered by a given grazing angle

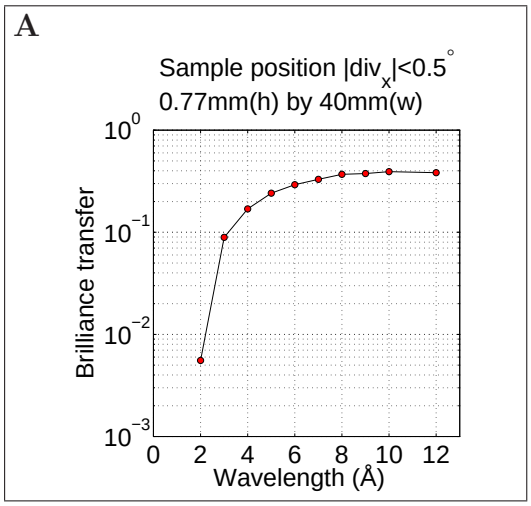

Figure 5: **A**:The brilliance transfer for horizontal divergence within ±0.5deg. The monitor area is 40mm (w) by 0.77mm (h). The height corresponds to 40mmsin 1.1deg. The brilliance transfer derived from monitors with heights 40mmsin 0.35deg and 40mmsin 3.7deg gives identical results.

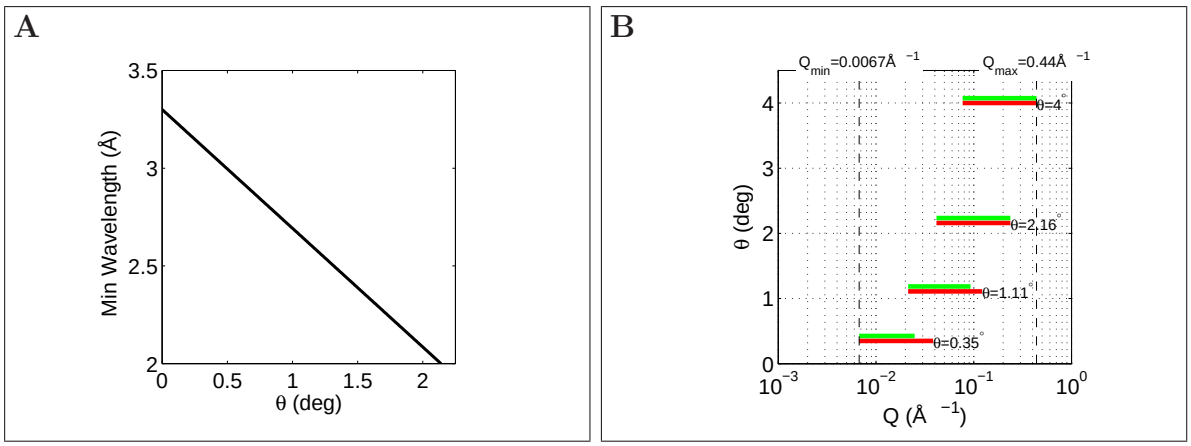

Figure 6: **A**: Assumed available minimum wavelength as function of grazing angle on the sample position.
B: Q range coverage with the full wavlength range (2 Å-11.4 Å) is shown with red lines. The green lines indicate the Q ranges covered with the limited wavelength range, that is from the minimum wavelength shown in **A** up to 11.4 Å.

θ is

$$Q_{\rm min} = \frac{4\pi}{\lambda_{\rm max}} \sin\theta \quad \text{and} \quad Q_{\rm max} = \frac{4\pi}{\lambda_{\rm min}} \sin\theta\,, \tag{10}$$

we see that only the value of $Q_{\rm max}$ will be affected for grazing angles smaller than 2.14°. To roughly estimate the impact on the reachable Q-range, we can simply assume that the minimum available wavelength at the sample position varies linearly with the grazing angle as shown in Fig. 6**A**. Assume now that we will cover the Q-range with $Q_{\rm min} = 0.0067\text{Å}^{-1}$ and $Q_{\rm max} = 0.44$ Å^{-1}. The red lines of Fig. 6**B** show how this may be done with the wavelength range 2 Å-11.4 Å using 4 different grazing angles. If the wavelength range is limited so the minimum wavelength varies with the grazing angle as shown in **B**, each grazing angle give access to the the Q-ranges indicated by the green lines.

4 Virtual experiments

4.1 Angular resolution

The results are simulated with a virtual source emitting a wavelength band of 1 Å to 13 Å . If not stated explicitly, the grazing angle at the sample is defined by two slits separated by a distance of 2 m. The slit which is close to the sample is slit 2. If not stated explicitly, the distance from slit 2 to the sample position is 28 cm.

4.1.1 Defining the grazing angle at the sample

Denoting by d_1 and d_2 the height of the slit gaps and by L_{12} the distance between the slits, the angular contribution to the Q-resolution may be determined by[3] [4]

$$\sigma_\theta = \frac{1}{L_{12}} \sqrt{\frac{d_1^2 + d_2^2}{12}} \,. \tag{11}$$

The factor $1/\sqrt{12}$ is due to the assumption that the divergence profile is rectangular. The sample position is at the distance L_{2s} from slit2. At the sample position the beam height h is

$$h \approx d_2 + \frac{L_{2s}}{L_{12}} \left(d_1 + d_2\right), \tag{12}$$

and illumintates an horizontal area of length

$$\text{footprint} \approx \frac{h}{\sin\theta} = \frac{d_2 + \frac{L_{2s}}{L_{12}} \left(d_1 + d_2\right)}{\sin\theta} \,. \tag{13}$$

The illumination of this area is not completely homogeneous. The sample is homogeneously illuminated within an area of length $d_2/\sin\theta <$ footprint. The lower limit of the footprint length $\mathrm{FW_{min}}$ depends on the smallest realistic slitgap which can be obtained. Here we have assumed that the limit is 30μm. The upper limit for the footprint length $\mathrm{FW_{max}}$ is defined as where the slit gaps $d_1 = d_2$. Fig. 7 shows the slit heights for $\Delta\theta/\theta$ =1.5% (**A**) and 4% (**B**) angular resolution as function of the footprint full length FW (Eq.13) and the minimum and maximum sample lengths which can be used without overillumination.

4.1.2 Correspondence between simulated and nominal angular resolution

Fig. 8**A** shows the divergence profiles derived from a horizontal monitor (4×4 cm^2) at the sample position. The grazing angle is 4°. Fig. 8**B** shows the simulated angular resolution as function of nominal angular resolution fwhm. The simulated angular resolution is derived from the fwhm and standard deviation of the divergence profiles. The dashed lines are linear fits to the data points with nominal angular resolution greater than the $(\Delta\theta/\theta)_{\mathrm{min}}$, which is the limit where the collimating slits 1 and 2 have the same gap height. From the linear fit we

[3] A.A. van Well, H. Fredrikze, Physica B, 357 (2005) 204–207

[4] V.-O. de Haan et al, Nuclear Instruments and Methods in Physics Researc A 362 (1995) 434-453

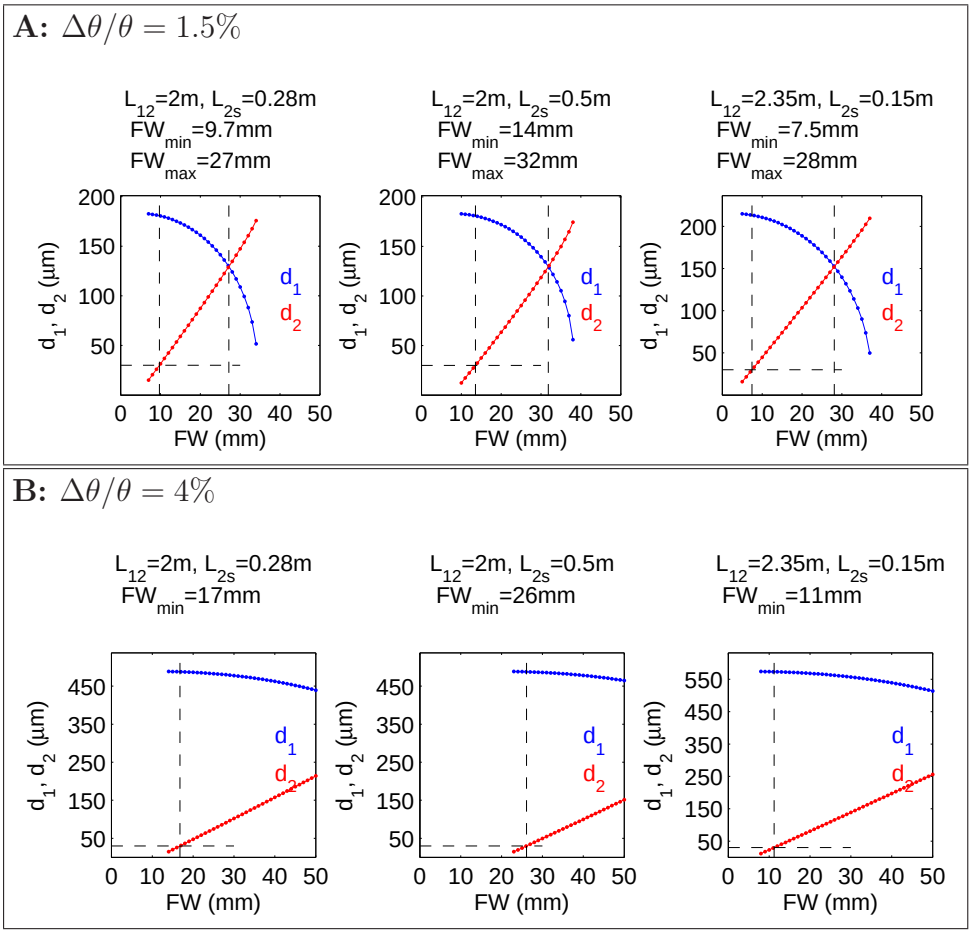

Figure 7: **A, B**: The slit heights calculated according to Eq. 11 and Eq. 12. The minimum sample length $\mathrm{FW}_{\mathrm{min}}$ is defined where the slit2 is 30μm. If smaller slit heights can be made, smaller samples can be used without over illumination. The maximum sample length $\mathrm{FW}_{\mathrm{max}}$ is defined as where $d_1 = d_2$.

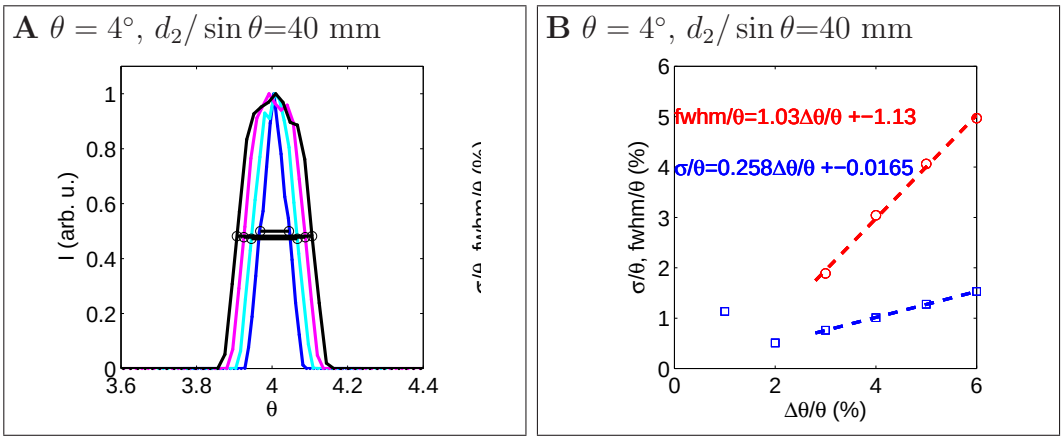

Figure 8: **A**: Divergence profiles at the sample position for different nominal angular resolutions and grazing angle 4°. **B**: The fwhm and standard deviation of the divergence profiles shown in **A**.

see that there is a good correspondence between the simulated angular resolution (fwhm) of the divergence profiles and the nominal angular resolution. The standard deviation amounts to $0.258\Delta\theta/\theta$ which is consistent with the observed triangular–rectangular peak shapes.

4.1.3 Correspondece between simulated and nominal sample illumination

Sec. 4.1.1 describes how the settings of the collimation slits may be defined from the sample dimensions and the required angular resolution. The Eq. 13 is a good approximation, however simulations indicate the corrections are necessary to ensure exact illumination of the sample. The slit settings of the simulated proposed instrument are based on Eq. 13 with corrections derived from simulations. Eq. 11 and Eq. 13 can be rearranged to

$$\text{footprint} \approx \frac{d_2}{\sin\theta}\,\alpha + \beta \tag{14}$$

where

$$\alpha = 1 + \frac{L_{2s}}{L_{12}} \quad \text{and} \quad \beta = \frac{L_{2s}}{L_{12}} \frac{\sqrt{12\,L_{12}^2\sigma_\theta^2 - d_2^2}}{\sin\theta}\,. \tag{15}$$

The simulations indicate that in general the full width of the illuminated area is wider than predicted by Eq.14. Further the corrections to Eq 14 are angle dependent, with the magnitude of β increasing dcreasing grazing angle. The simulated results in Sec.4.6 utilize the corrections to Eq14 shown in Table 1.

4.2 Conversion of time-of-flight WFM data

The data sets from the virtual experiments using standard samples are simulated as intensity as function of time-of-arrival at the detector position. Fig. 9**A** shows the direct beam incident on the sample with 4° grazing angle. The 7 WFM pulses are clearly separated in time. To convert the shown time-of-flight data to intensity as function of wavevector transfer Q, we need to know for each wavelength the exact flight time from the mid-position between the choppers PSCH1 and PSCH2 to the detector position.

	θ (°)	L_{12} (m)	L_{2s} (m)	$\Delta\theta/\theta$ (%)	α	β (mm)	$\Delta\theta/\theta$ (%)	α	β (mm)
simulation	0.35	2.35	0.15	1.5	1.01	4.03	4	1.03	7.39
Eq.15					0.989	2.91		1.05	6.17
simulation	0.35	2.0	0.28	1.5	1.10	6.58	4	1.10	13
Eq.15					0.979	5.43		1.10	11.5
simulation	4	2.0	0.28	1.5	1.09	4.8	4	1.09	11.8
Eq.15					0.979	5.43		1.10	11.5

Table 1: Corrections to Eq. 14, 15 derived from simulations. The values of α and β derived from the simulations are angle dependent, contrary to the values calculated from Eq. 15.

Fig. 9**B** and **C** shows how the mean arrival time of each neutron wavelength may be derived from the simulations. These results may also be obtained analytically from the exact chopper geometries, positions, relative phase and frequencies. The neutron take-off times as function of wavelength from the mid position between the choppers PSCH1 and PSCH2 is derived in a similar way. With the knowledge of the flight path length and the flight time to the detector we can calculate the neutron energy and wavelength from the time-of-flight according to

$$E = 5.22704 \cdot 10^{-6} \left(\frac{L_{\text{flight}}}{t_{\text{flight}}} \right)^2 \tag{16}$$

and

$$\lambda = \frac{2\pi}{\sqrt{E/2.072}} \,. \tag{17}$$

Fig. 9**D** shows the intensity as function of wavelengths as calculated from the time-of-flight for the 7 WFM pulses. This data is then rebinned to a single data set and Q is calculated as $4\pi \sin\theta/\lambda$.

4.3 Wavelength- and Q-resolution, WFM data

The relative wavelength spread $\Delta\lambda/\lambda$ is estimated from the $\Delta t/t_{\text{flight}}$, where Δt is the time spread monitored at the detector position. Fig. 9**E** shows the relative wavelength spread at the detector derived from the simulations as $\Delta t/t_{\text{flight}}$. We see that the wavelength resolution fwhm $\Delta\lambda/\lambda$ is wavelength dependent and in general varies between 1.5% and 2.7% (circular data points). At the beginning and end of each WFM pulse the wavelength spread is smaller. However, when the data is rebinned to a single data set as shown with blue data points in Fig. 9**D**, the resolution will roughly follow the black line shown in Fig. 9**E**. The black line is derived from a fit of a 2nd order polynomial to the circular data points, as shown in Fig. 9**F**. The derived polynomial is used to calculated the bin widths (equal to the Q-resolution) used for the virtual sample data sets. Fig. 9**G** shows (for 3 different grazing angles 0.35°, 1.1°, 4°) the relative Q resolution calculated from the wavelength resolution and the angular resolution.

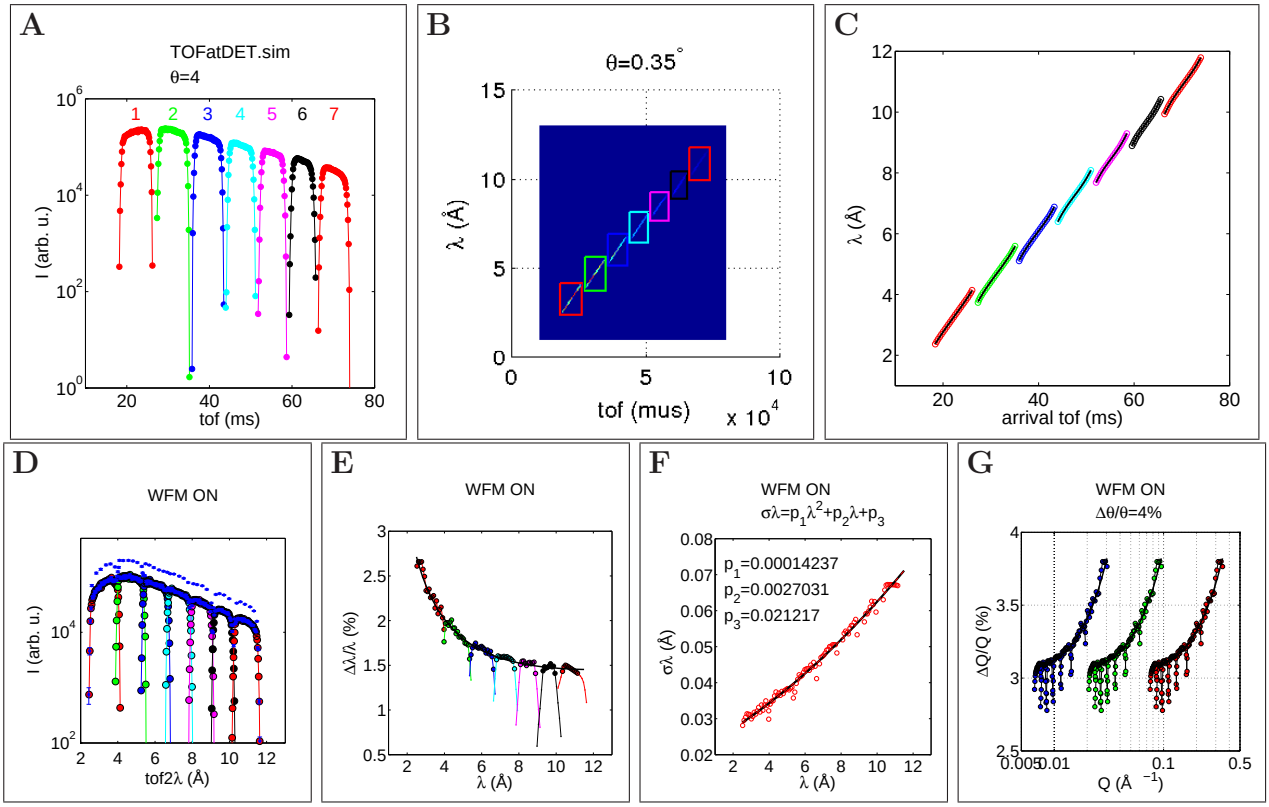

Figure 9: **A**: The positions in time of the 7 different WFM pulses are determined by a time-of-flight sensitive monitor at the detector position.
B: The information from the high resolution time-of-flight monitor **A** is used to separate the pulses on the wavelength and time-of-flight sensitive monitor at the detector position.
C: The mean arrival time and time width at the detector for each wavelength is derived from **B**. The circles indicate the mean arrival time as derived from **B**, the black lines is a 3rd order polynomial fitted to the data points.
D: The simulated intensity as function of the wavelengths calculated from time-of-flight. The big circles with different colors indicate the 7 data sets corresponding to the 7 WFM pulses. The blue points show the same data, but rebinned to a single data set.
E: The relative wavelength spread as calculated from the time spreads derived from **B** and the flight time from the mid position between the 1st pair of PS choppers to the detector. The circular data points are included in the fit shown in **F**.
F: A fit of a 2nd order polynomial to the circular data points shown in **E**.
G: The relative Q resolution calculated from the wavelength resolution and the angular resolution for 3 different grazing angles 0.35° (blue), 1.1° (green), 4° (red). The black line is the Q resolution calculated from the 2nd order polynomial shown in **F**, the angular resolution and the grazing angle.

4.4 Estimation of counting times and derivation of virtual data from simulations

In a typical simulation the result consists of a count of neutrons histories ("rays") with different weights w. The sum of these weights, I_i, is an estimate of the mean number of neutrons hitting bin number i in the monitor (or detector) per second in a "real" experiment,

$$I_i = \sum_j w_{i,j} \,, \tag{18}$$

where $w_{i,j}$ is the weight of ray number j arriving in bin number i. If we increase the number of rays (by increasing the value assigned to the `--ncount` parameter), the statistical mean value of I_i will remain unchanged, but the *precision* (in the meaning of repeatability) of the simulation will be enhanced. Another result of the simulation is an estimate of the statistical errors of the intensities, i.e. a measure of the simulation *precision*. Sec. 4.2.1 in the *User and programmers guide to the neutron ray-tracing package McStas, version 2.0*[5] explains how these statistical errors are estimated within McStas, and the standard deviation σ is approximated by

$$\sigma^2(I_i) = \sum_j w_{i,j}^2 \,. \tag{19}$$

The paper[6] by K. Lefmann et al describes in detail how simulated data may be scaled to absolute measurement times.

4.4.1 Real vs simulated data

A dataset from a "real" experiment is often analyzed using Poisson statistics. When the number of counts n_i per bin exceeds ∼20, the Normal Approximation to the Poisson distribution is adequate. Here the standard deviation σ_i for each point is

$$\sigma_i^2 = n_i \,, \tag{20}$$

and the total number of counts is

$$N = \sum_i n_i \tag{21}$$

with the standard deviation σ

$$\sigma^2 = \sum_i \sigma_i^2 = N \,. \tag{22}$$

The approximation improves as n_i increases. In general the "counts" per bin in a simulated data set rarely demonstrates this relation.

[5] http://mcstas.org/documentation/manual/mcstas-2.0-manual.pdf

[6] Journal of Neutron Research, Vol. 16, Nos. 3–4, September–December 2008, 97–111

4.4.2 Counting time and data quality

With a simulated data set $(I_i, I_{\mathrm{err},i})$ and a counting time t we will have $n_i = tI_i$ counts in bin number i, with the standard deviation $t\,I_{\mathrm{err},i}$. Simulations can (also) be useful to estimate a necessary counting time to get data of a specified quality. To make a reliable estimate of this counting time, first of all the simulated instrument model must be realistic. Further, the noise content of the simulated data set must be *less* than it would be in a real experiment, so we require that

$$t\,I_{\mathrm{err},i} \leq \sqrt{n_i} = \sqrt{t\,I_i} \tag{23}$$

from which we get

$$t \leq \frac{I_i}{I_{\mathrm{err},i}^2}\,. \tag{24}$$

Eq. 23 must hold for every individual bin in the data set. In general Eq. 23 is not fulfilled. Either the noise content of the simulated data bins is lower or higher than it would be in a real experiment. If Eq. 23 is fulfilled, the noise content of the simulated data is less than it is in a measured data set, and the simulated data set can then be used as the fundament at which base our estimate of a "real" data set.

4.4.3 Estimating the appearance of a "real" data set

Assume that we have a simulated data set (I, I_{err}) which, for a certain counting time t fulfill Eq. 23, so we have a fundament at which we can base the estimate of a "real" data set. Assume that we have $n_i = tI_i$ counts in bin number i and the standard deviation of that bin is $tI_{\mathrm{err},i}$. We then require that the noise content of a "real" data set is

$$\sigma_i = \sqrt{n_i} > tI_{\mathrm{err},i}\,, \tag{25}$$

so we must *add noise* to the simulated data in order to derive a more realistic set of data. The amount of noise which must be added to *each bin* is estimated from the simulated standard deviations. For each bin the noise could be added as a random number from a normal distribution with standard deviation $E_{+,i}$ and mean parameter 0. The magnitude of $E_{+,i}$ is

$$E_{+,i}^2 = n_i^2 - (tI_{\mathrm{err},i})^2\,. \tag{26}$$

4.5 Sample flux

Fig. 10 compares the collimated flux on a horizontal monitor at the sample position for 3 different grazing angle of incidence 0.33°, 1.1° and 4°. These grazing angles are identical to those used for the virtual experiments. The labelling A, B refers to different collimation distances. The percentages $\phi \approx x\%$ are comparisons of the different flux curves to dark blue curve, which represents the average flux on an exact illuminated horizontal sample area of 4×4 cm^2 and angular resolution $\Delta\theta/\theta = 4\%$ fwhm with the WFM choppers deactivated. In the following the differences between the models are explained. In Sec.2 the guide system is characterized in terms of brilliance transfer.

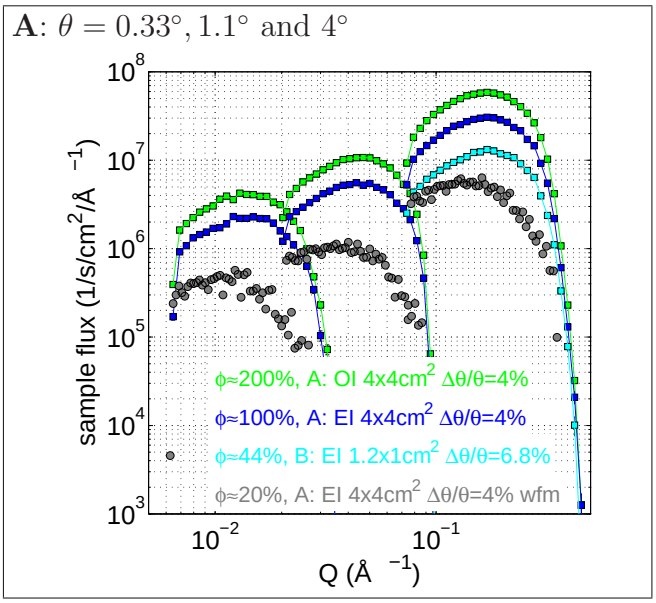

Figure 10: **A**: Comparison of the sample flux for exact under-illumination and over-illumination (UI, OI) for different instrument settings and instrument models - see text for explanation. The slit settings for exact illuminations are shown in Tab. 2.

MODEL	θ (°)	$\Delta\theta/\theta$ (%)	L_{12} (m)	L_{2s} (m)	d_1 (mm)	d_2 (mm)	w_1 (mm)	w_2 (mm)	$d_2/\sin\theta$ (mm)	w_2/L_{12} (°)
A, OI	4	4	2	0.28	4.838	2.790	40	40	40	1.14
A, UI	4	4	2	0.28	5.316	1.712	30	30	24.55	0.86
B, UI	4	6.8	2.21	0.07	10.467	0.321	9	9	4.60	0.23

Table 2: Slit settings for models A, B in Fig. 10.

Model A This is the proposed instrument with a 9.5 m long 4 channel bender section. The instrument is simulated with the updated McStas 2.0 standard reflectivity curves, see Fig. 1**B**. The flux curves labeled A in Fig 10 are simulated with identical guide systems and the flux is averaged over a horizontal area of $4 \times 4\text{cm}^2$ at the sample position. The blue curve shows the average flux with exact illummination of the sample, as shown in Fig. 11**A, B** for 4° and 0.35° respectively. If the WFM choppers are activated, the average flux is reduced to about 20% compared to the WFM off flux. If overillumination can be tolerated, the height of the slit 2 may be $d_2 = \theta L$ for a sample of length L. Fig 11**C, D** shows the intensity distribution on the $4 \times 4\text{cm}^2$ over-illumminated horizontal sample for 4° and 0.35° respectively. The green curve in Fig. 10 shows that the average flux on an overilluminated sample is 200% compared to an exactly illuminated sample of same area.

Model B This instrument model is identical to the proposed instrument except

- the position of the slit 2 is shifted 21 cm downstream, so $L_{2s} = 0.07$ m (in Model A it was $L_{2s} = 0.28$ m)
- the collimation distance is increased to $L_{12} = 2.21$ m (in Model A it was $L_{12} = 2$ m)

In Fig. 10 the flux curves labeled B show the flux averaged over an exact illuminated horizontal area of 1.2 cm×1.0 cm at the sample position and angular resolution 6.8% fwhm. The slit

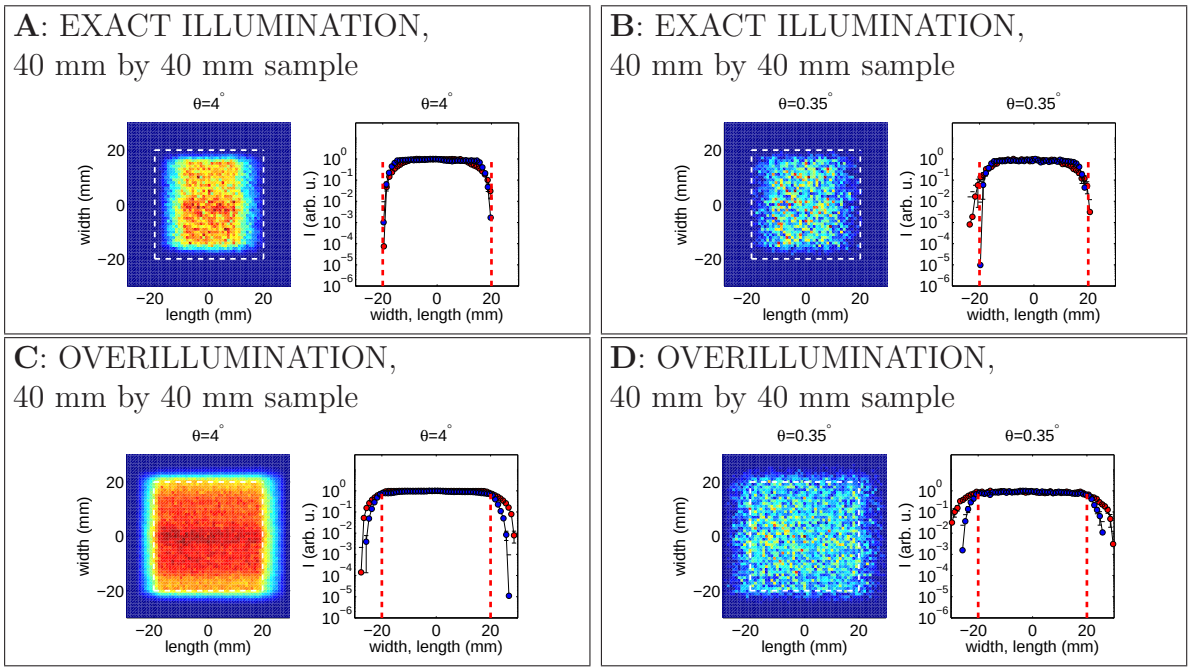

Figure 11: Comparison of the sample flux for exact and over-illumination (denoted by EI, OI in Fig. 10). For exact illumination the slit settings are as defined by Eq. 13. For over-illumnitation the height of slit 2 (the slit close to the sample) is $d_2 = \theta L$ for a sample of length L. In each panel the left image shows, on a linear scale, the spatial distribution of intensity on a horizontal monitor. The right panel shows, on a logarithmic scale, the intensity profiles achieved by integration along the length (blue), width (red).

settings are shown in Tab. 2 and the sample illumination is shown in Fig 12.

4.5.1 Comparison of flux - Model A, B

The total intensity of a beam collimated by a pair of slits may be calculated according to[7]:

$$I_t = T\Phi_t d_1 \frac{d_2/L_{12}}{\alpha_v} w_1 \frac{w_2/L_{12}}{\alpha_h} \tag{27}$$

where the factor T takes into account the transmission of the choppers and the flight path and $\alpha_{v,h}$ is the incident beam divergence in the vertical/horizontal direction. d_1, w_1 and d_2, w_2 are the slit heights, widths and L_{12} is the collimating distance. This equation holds if $d_2/L_{12} < \alpha_v$ and $w_2/L_{12} < \alpha_h$. If any of the ratios $\frac{d_2/L_{12}}{\alpha_v}$ or $\frac{w_2/L_{12}}{\alpha_h}$ exceeds 1, they must be replaced by 1 in Eq. 27. Fig. 13 shows the horizontal divergence at the sample position, both as basewidth, fwhm and standard deviation. We see that for wavelengths $\lambda > 3$ Å, the basewidth is 2.37° corresponding to ±1.18° so $\alpha_h \leq 1.18°$.

Tab. 2 gives the slit settings for Model A and B. Here we compare the expected flux for exact illumination. For both models, the ratio $d_2/L_{12} < \alpha_v$. For Model A the ratio $w_2/L_{12} = 0.86°$ which comparable to α_h. Eq. 27 suggests that Model A will have 2.26 times more flux $(1/\mathrm{s/cm^2})$ than model B, corresponding to $\phi = 44.2\%$ in Fig. 10. A comparison of the simulated flux for Models A,B shows that the actual simulated difference is in accordance with Eq. 27.

[7]V.-O. de Haan et al, Nuclear Instruments and Methods in Physics Research A 362 (1995) 434-453

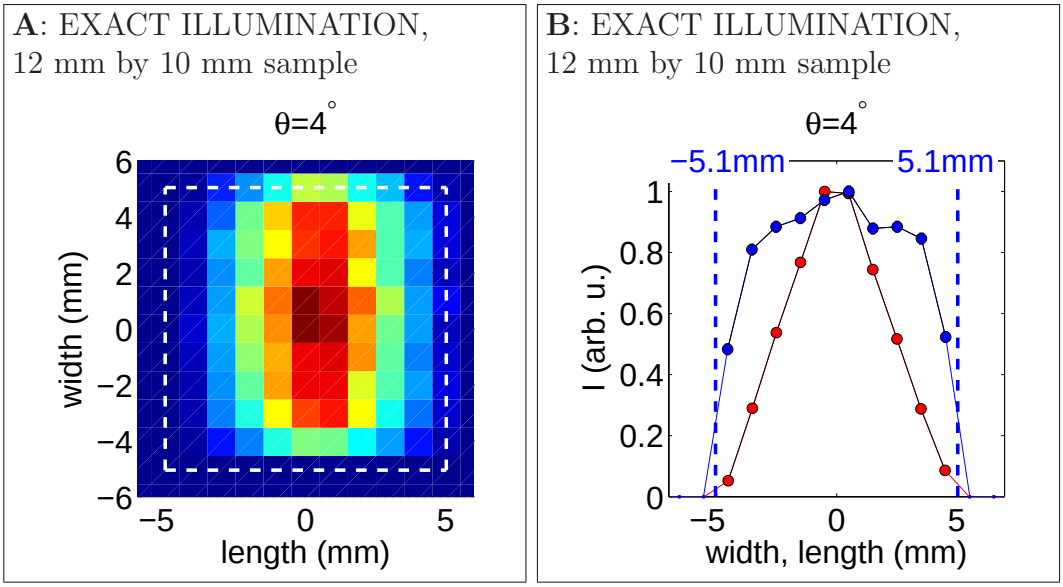

Figure 12: Model B illumination of the horizontal sample. The slit settings are as defined by Eq. 13 (with corrections) and can be found in Tab. 2.
A: The spatial distribution of intensity on a horizontal monitor at the sample position.
B: The intensity profiles from integration of **A** along the length (blue), width (red). The non-zero bins are indicated by circles. The dashed blue lines at ±5.1mm indicates the center between the bins with zero counts and non-zero counts. For the red data points illumination corresponds to exact ±5 mm.

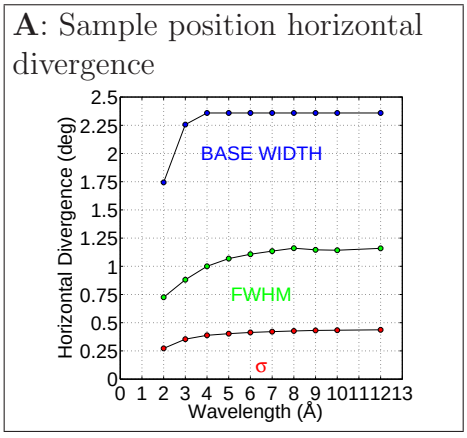

Figure 13: **A**: The collimating slits are wide open. The horizontal divergence monitored at the sample position.

4.6 The standard sample simulation

The standard sample simulations assumes an exactly illuminated sample area of 1 cm by 1 cm. A background corresponding to 10^{-7} times the direct beam must be added and accounted for when the errorbars are estimated. The background is subtracted and the data is binned to $\Delta Q/Q = 1\%$. There must be at least 50 signal counts in the $Q = 0.35$ Å^{-1} bin.

In Sec. 4.5 we have showed that an exact illumination of such and area can be obtained with the proposed instrument (with angular resolution $\Delta\theta/\theta = 6.8\%$ fwhm and $L_{2s} = 0.07$ m). The average flux is about 2.25 times less than the average flux on a 4 cm by 4 cm sample when $\Delta\theta/\theta = 4\%$ and $L_{2s} = 0.28$ m (called 'Model A'). In Sec. 4.5.1 we have justified the factor 2.25 by analytical calculations.

Due to the very low intensity on such a small sample, we have simulated only the $\theta = 4^\circ$ direct beam. From this data set we have derived the scaling factor of 2.25×16. The 2 other grazing angles, 0.33° and 1.1° are obtained from Model A by scaling with a factor 2.25×16. The factor 16 is due to the area difference and the factor 2.25 can be understood from Eq. 27. Fig. 14 **A,B** shows a simulated reflectivty curve within Model A. The data is binned according to the instrument resolution which is shown in Fig. 14 **C**. Fig. 14 **D** shows the same data set but scaled to mimic a 1 cm by 1 cm exactly illuminated sample. The Q bin widths corresponds to the instrument resolution. The last $Q < 0.35$ Å^{-1} with 50 signal counts is at a reflectivity of about 3×10^{-8}.

Fig. 14 **E,F** shows the needed counting times when we require a binning of $\delta Q/Q = 1\%$. Due to the dramatically decrease of the bin widths (from $\delta Q/Q \approx 14.1\%$ at high Q to constant $\delta Q/Q = 1\%$), the counting times to obtain 50 signal counts at $Q = 0.35$ Å^{-1} increases with a correspondingly. Here the counting time is 14 times higher, simply due to the difference in bin widths. Similar arguments applies to the scaling of the data when the WFM is activated.

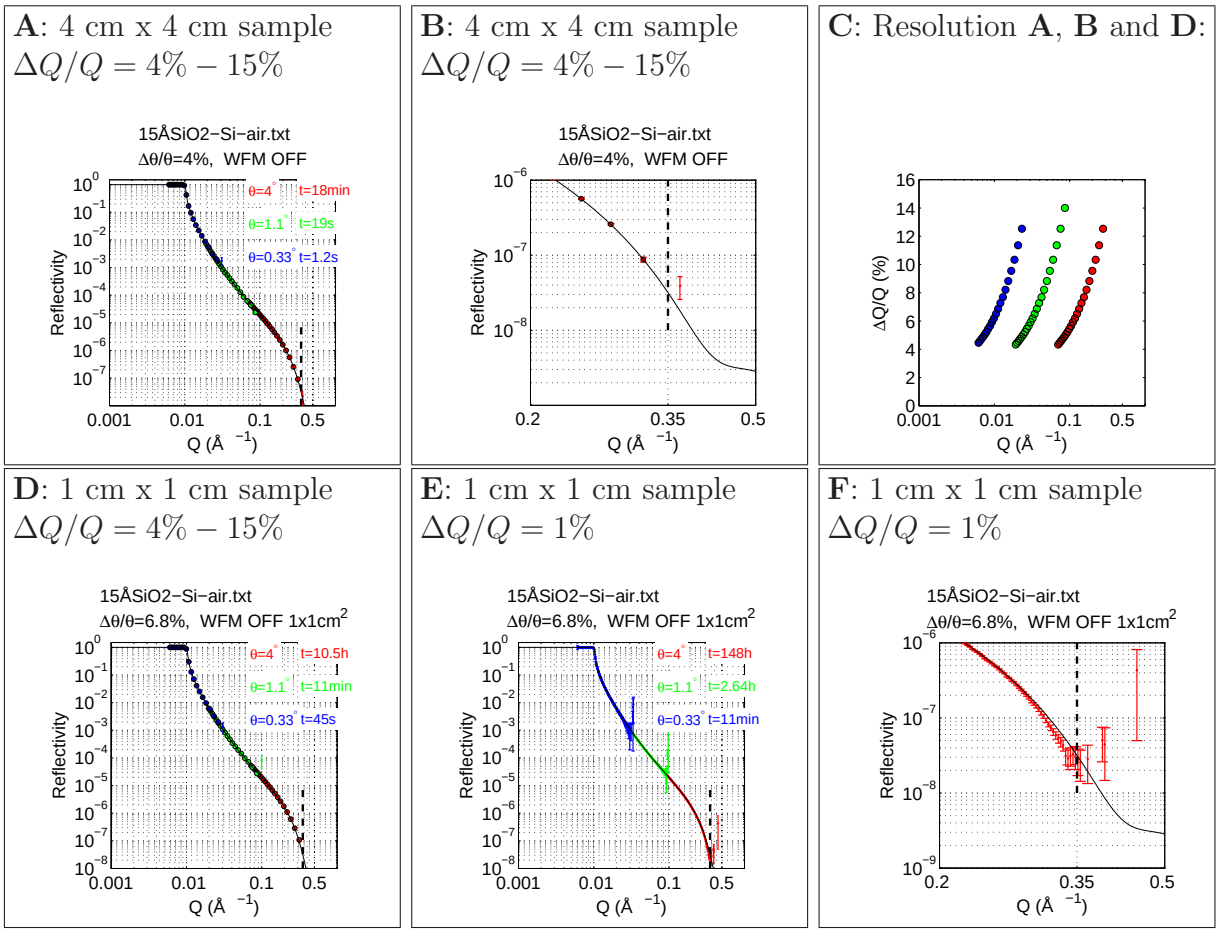

Figure 14: Virtual reflectivity curves. The wavevector transfer Q is derived from a time-of-flight sensitive monitor. A background of 1e-7 times the direct beam has been added and subtracted. There are 50 signal counts in the bins $Q < 0.35$ Å^{-1}.
A: Model A, with the WFM turned OFF.
B: Model A, zoomed view of **A**.
C: The full binwidths of **A, D** divided by the bin center, the Q-resolution corresponds to the instrument resolution.
D: Model B. The counting times are scaled relative to those shown in **A** by a factor 16×2.25.
E: Model B, binned to $\delta Q/Q = 1\%$. The counting times are scaled relative to those shown in **A** by a factor 16×2.25×14.1.
F: Model B, zoomed view of **E**.

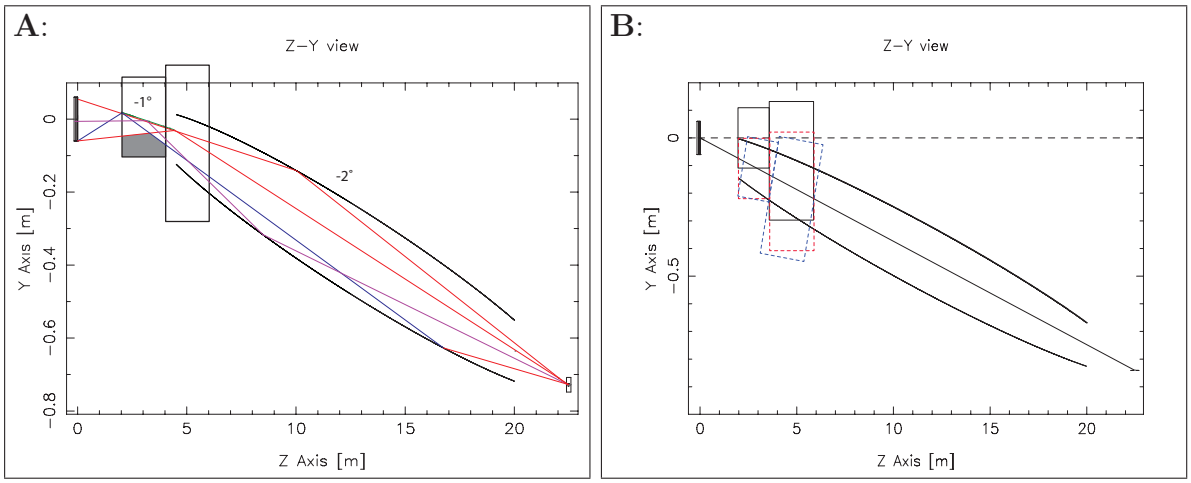

Figure 15: **A**: Geometry of the FREIA beam extraction. The deflecting mirror allows 2.4 Å neutrons from the bottom of the moderator to be reflected at up to the critical angle therefore all longer wavelengths are reflected along the full length. The vertical position of the mirror was chosen so that it only blocks those rays which would enter the inclined guide at too high angles to be reflected onto the sample.
B: Geometry of the guide used for the optimization. The guide is inclined by -2.14 degrees and has its first focal point at the centre of the source.

5 Other simulations

5.1 Pancake moderator

The beam extraction geometry of the current FREIA instrument was designed to allow the required vertical divergence to be extracted through the baseline beam extraction unit. The design relies on a 2.5m long deflecting mirror to illuminate the inclined elliptical guide, which has its first focal point at the centre of the deflecting mirror. The mirror acts as a virtual source for neutrons that otherwise could not be accepted into the guide, which cannot be inserted at 2m due to its height and the inclination. The mirror length and its position were optimized to view as much of the source and to accept as many of the 2 Å neutrons as possible. This leads to the configuration sketched out in Fig. 15**A**. In this geometry, the length and position of the mirror are fixed by the need to illuminate the large elliptical guide with as much divergence as possible. Reducing the moderator size however dictates that the length an position need to decrease in proportion (otherwise it is under-illuminated), and the height should follow the centre of the moderator, which leads to an incomplete illumination of the guide. So for this geometry the smallest usable moderator size is 10cm, and the optimum would be around 20cm.

The moderator height optimization was done using a version of the 25m long FREIA instrument which does not include the 2.5m deflecting mirror before the beginning of the guide. This geometry implies that a customized beam port would be required to fit the elliptical guide in at an inclination of -2 degrees. This corresponds to lowering the height of the beam port by approximately 6cm relative to the centre of the moderator, and a small inclination as shown in Fig. 15**B**. The possibility of splitting the guide into two elliptical section of half the length (and half the height) was investigated but led to unacceptable divergence losses due to the larger relative fraction of missing guide (2m from moderator + 2.5m to sample).

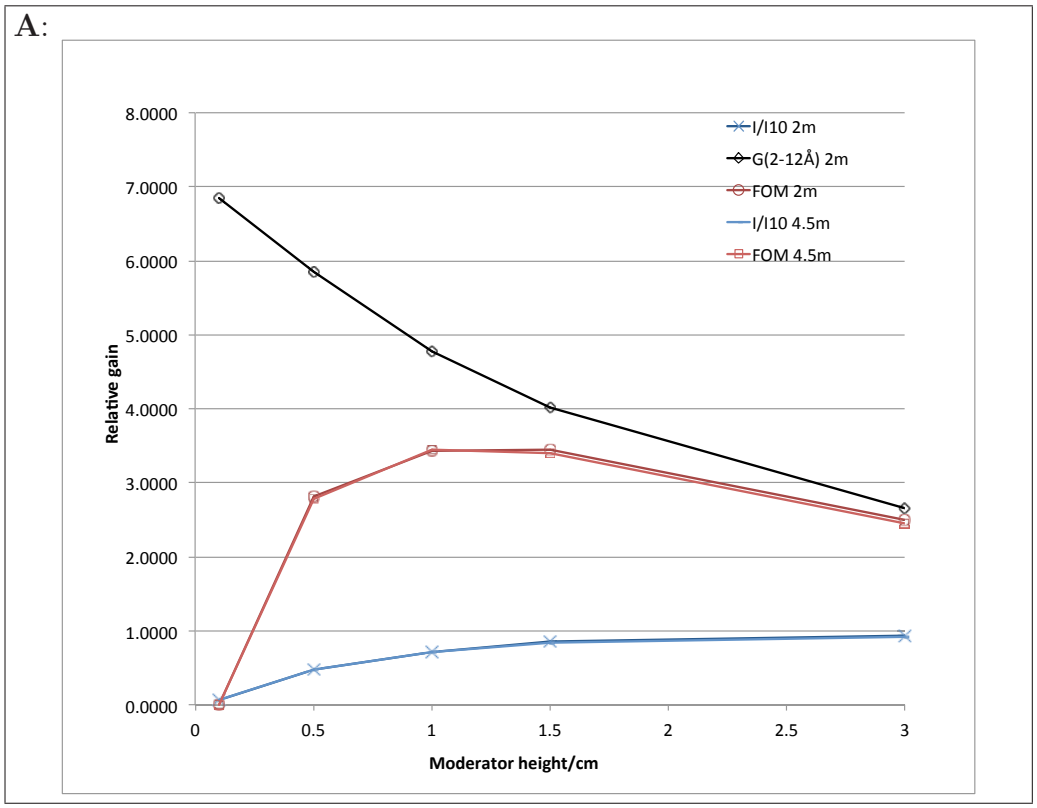

Figure 16: Intensity from a flat moderator (grey crosses) normalized to the intensity of a 10cm flat moderator, gain factor for the ESS cold source for 2-12 Å neutrons (black diamonds), and their product (red circles), as function of moderator height. Clearly this is not sufficient information to determine a real figure of merit, since the instrument performance depends critically on the vertical divergence range that can be transported to the horizontal sample position.

As a first figure of merit, the intensity on a 4cm x 4cm horizontal sample was scanned as function of moderator height using a flat source with 2-12 Å wavelengths, which was then multiplied by the wavelength dependent gain factor B (normalised to a 10cm moderator and integrated over 2-12 Å) to obtain a relative figure of merit. This is shown in Fig.16 for the guide starting at 2m and 4.5m from the source. Clearly this is not sufficient information to determine a real figure of merit, since the instrument's performance depends critically on the vertical divergence range that can be transported to the horizontal sample position. Figures 17-19 show the dependence of the divergence and wavelength distribution at the sample position for moderator heights from 30m down to 10mm. It can be seen that the Vertical divergence is uniform on the sample area down to 30mm, below which the long wavelengths at low divergence start to disappear. These results suggest that a FREIA instrument without a deflecting mirror before the elliptical guide, with a focal point in the moderator will be able to gain a factor of 2.8 without significant losses in either divergence or the long wavelengths, at a moderator height of 25mm.

A:

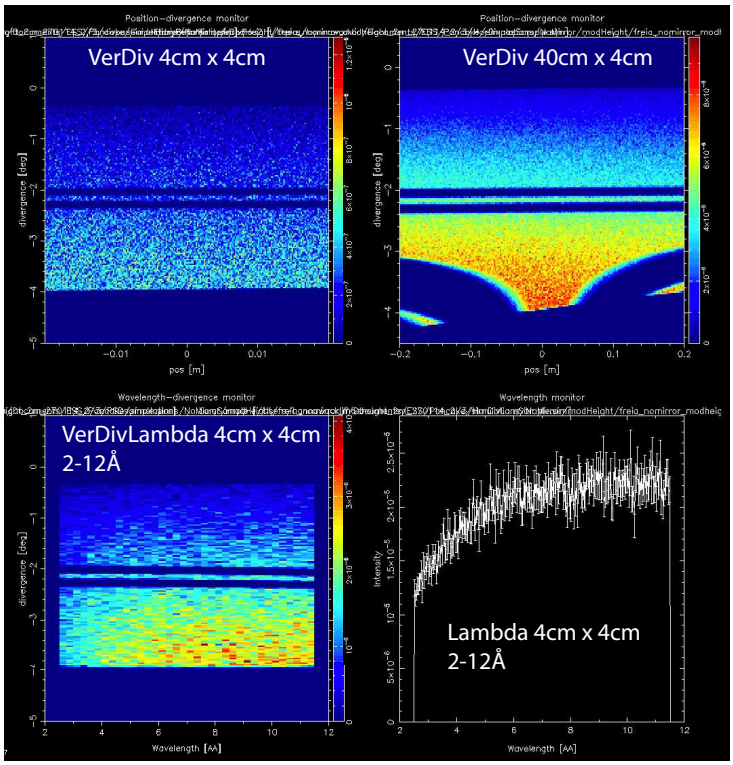

B:

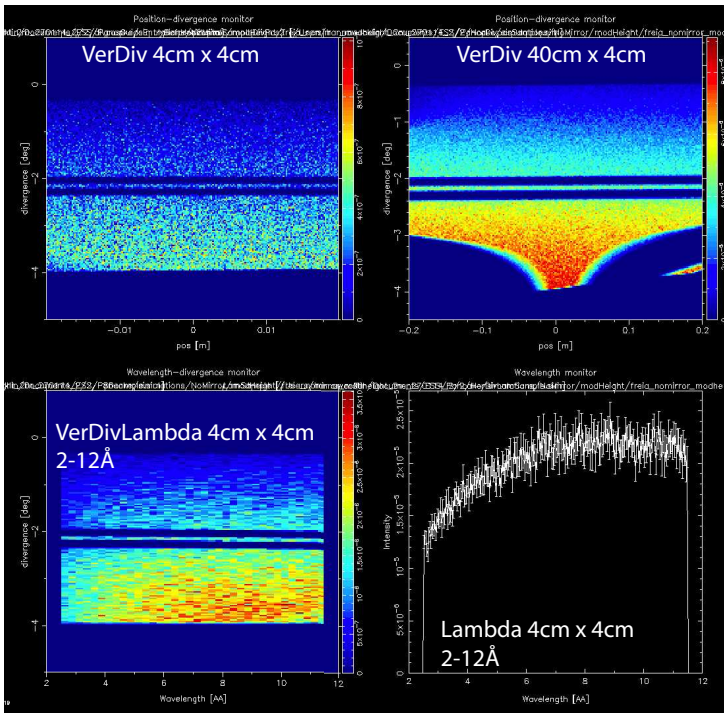

Figure 17: **A**: Moderator height = 40mm. Top row: left - vertical divergence impinging on a 4cm x 4cm horizontal sample, right - vertical divergence over 40cm around the sample centre. Bottom row: left - wavelength-divergence distraction and right - wavelength spectrum on a 4cm x 4cm horizontal sample, 2-12 Å. The guide starts at 2m from source.
B: Moderator height = 30mm. Top row: left - vertical divergence impinging on a 4cm x 4cm horizontal sample, right - vertical divergence over 40cm around the sample centre. Bottom row: left - wavelength-divergence distraction and right - wavelength spectrum on a 4cm x 4cm horizontal sample, 2-12 Å. The guide starts at 2m from source.

A:

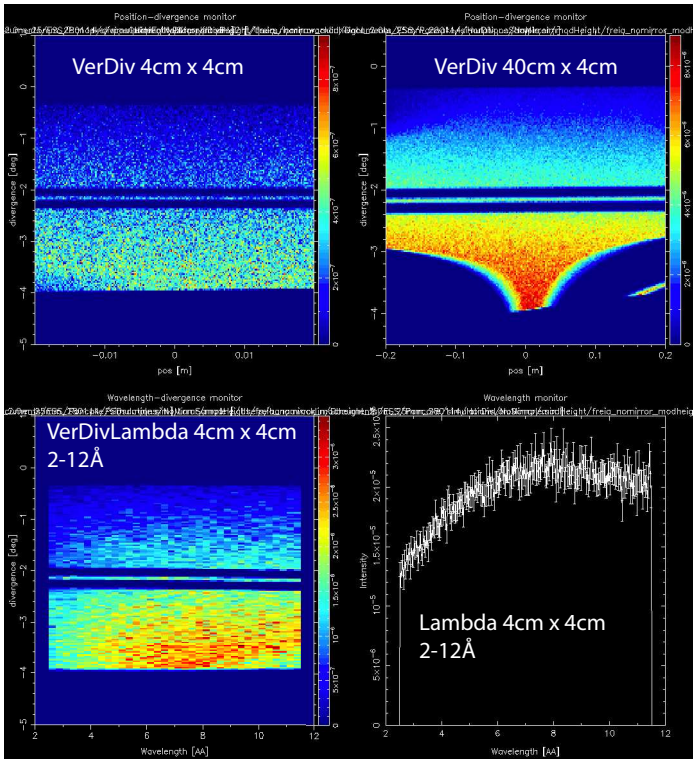

B:

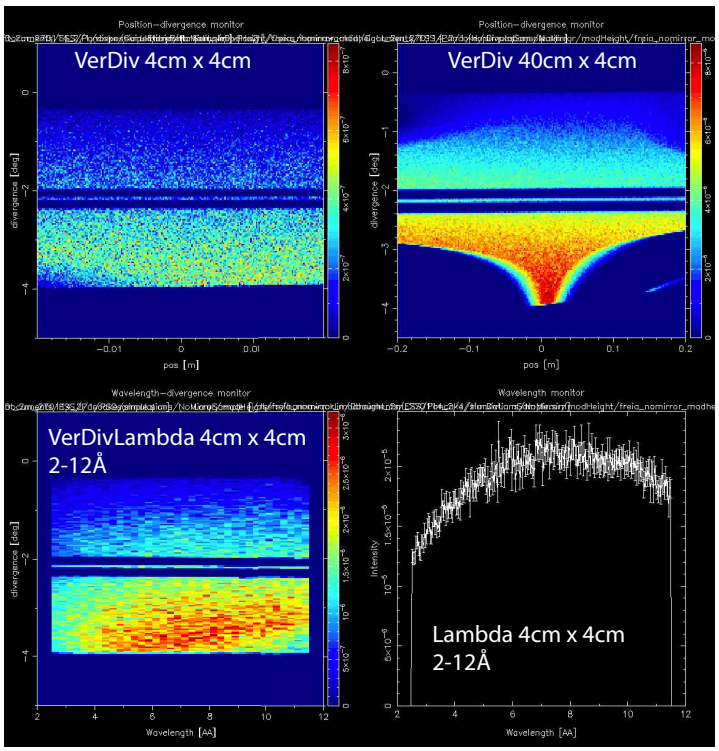

Figure 18: **A**: Moderator height = 25mm. Top row: left - vertical divergence impinging on a 4cm x 4cm horizontal sample, right - vertical divergence over 40cm around the sample centre. Bottom row: left - wavelength-divergence distraction and right - wavelength spectrum on a 4cm x 4cm horizontal sample, 2-12 Å. The guide starts at 2m from source.
B: Moderator height = 20mm. Top row: left - vertical divergence impinging on a 4cm x 4cm horizontal sample, right - vertical divergence over 40cm around the sample centre. Bottom row: left - wavelength-divergence distraction and right - wavelength spectrum on a 4cm x 4cm horizontal sample, 2-12 Å. The guide starts at 2m from source.

A:

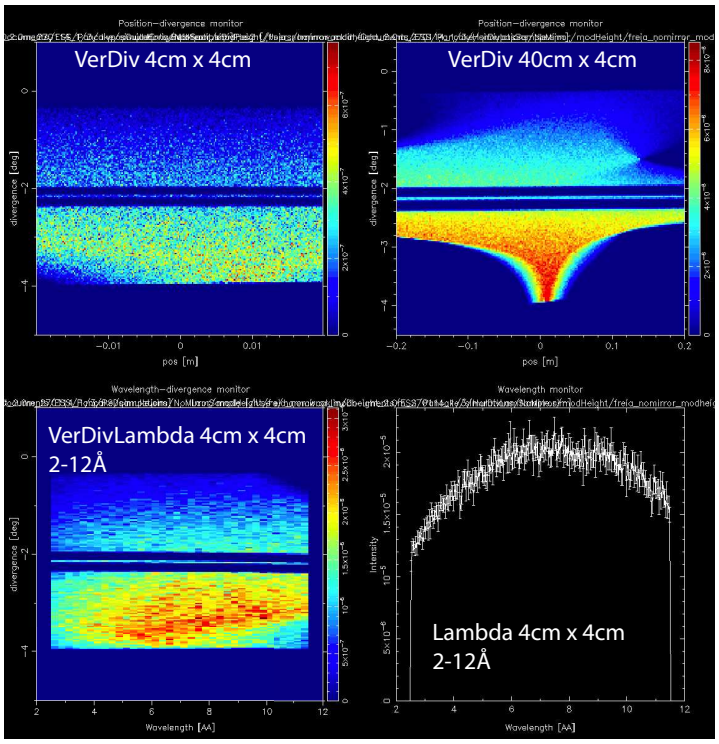

B:

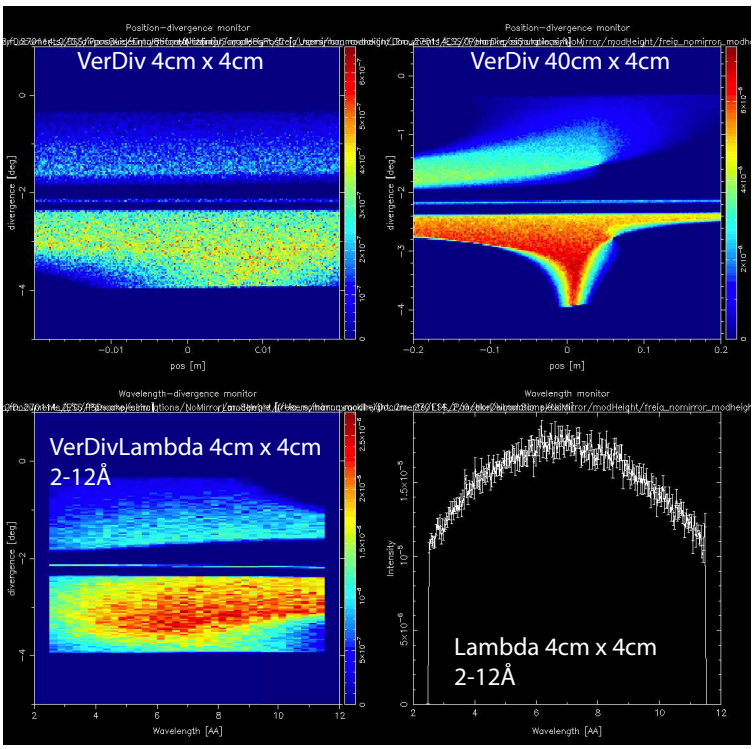

Figure 19: **A**:Moderator height = 15mm. Top row: left - vertical divergence impinging on a 4cm x 4cm horizontal sample, right - vertical divergence over 40cm around the sample centre. Bottom row: left - wavelength-divergence distraction and right - wavelength spectrum on a 4cm x 4cm horizontal sample 2-12 Å. The guide starts at 2m from source.
B:Moderator height = 10mm. Top row: left - vertical divergence impinging on a 4cm x 4cm horizontal sample, right - vertical divergence over 40cm around the sample centre. Bottom row: left - wavelength-divergence distraction and right - wavelength spectrum on a 4cm x 4cm horizontal sample, 2-12 Å . The guide starts at 2m from source.

5.2 Choppers

Wavelength Band Choppers Three pairs of counter-rotating diskchoppers are inserted at 6.5 m,10 m and 15 m from the moderator to select the used wavelength band (e.g. 2 Å –11.4 Å) and to avoid overlap between successibe frames. The spacing between the two choppers in a pair is 2.5 cm and at each side of the pair there is a distance of 1.25 cm to the guide. All chopper pairs have a radius of 375 mm and run at 14 Hz or 7 Hz. With a guide width of 50 mm, one chopper is partially open for (50 mm)/(729 mm$\times 2\pi \times$ 14 Hz)=780 μs. The chopper pairs at 6.5 m and 10 m have angular openings of 150° and 200°, while the one at 15 m has openings of 175° and 200°. The choppers are phased so that first window begins to open for the arrival of the shortest wavelength neutrons coming from the beginning of the 2.86 ms ESS pulse and the second window is fully open until immediately after the longest wavelength neutrons from the end of the 2.86 ms ESS pulse have arrived. Fig. 21 shows that the choppers are working as expected. The first two chopper pairs are sufficient at 14Hz and in the pulse-skipping mode at 7Hz the third pair is required to avoid frame-overlap neutrons with up to 70Å wavelengths.

Wavelength Frame Multiplication Pulse shaping choppers at the first available position = 6.5m at ESS transmit only a limited bandwidth, e.g. a single chopper creating 1ms pulses: If the shortest wavelength is 2Å and starts from the end of the 2.86 ms pulse, the longest wavelength that starts from the beginning of the pulse and arrives at the 6.5m 1ms later is 4.35Å . The bandwidth is thus 2.35Å , which fills less than half of the 71 ms frame.

The natural length of an instrument is defined as the length at which the selected bandwidth fills the frame. This can be derived from:

$$L_{\mathrm{nat}} = \mathrm{posWFM} + \mathrm{posWMF}\frac{t}{T}\,,$$

where t is the pulse length and T is the source period. For 6.5 m as the first chopper position that is

$$L_{\mathrm{nat}} = 6.5 \times 24.97 = 162.32\mathrm{m}$$

Clearly this is not a good solution for broad bandwidth instruments. If using a double chopper system to generate a constant resolution proportional to the chopper separation, the bandwidth is even more limited.

To overcome the bandwidth limitation, wavelength frame multiplication can be used. In this system double disc choppers separated by a distance z_0 are used with multiple windows to select frames with increasing wavelength from the source pulse. E.g. 7-fold WFM at dt/t = 2% (full width) for 2.5-11.3Å (as on FREIA) is shown below. The lines depict the time of flight of the shortest and longest wavelength neutrons in each subframe. The pulse length increases with wavelength keeping the relative resolution constant.

If no WFM is used, a double chopper with one window can only accept a bandwidth equivalent to one of the subframes for the same resolution.

Definition of the first WFM frame The time at which the shortest wavelength neutrons from the end of the pulse (2.86ms) reach the first WFM chopper defines the closing point of

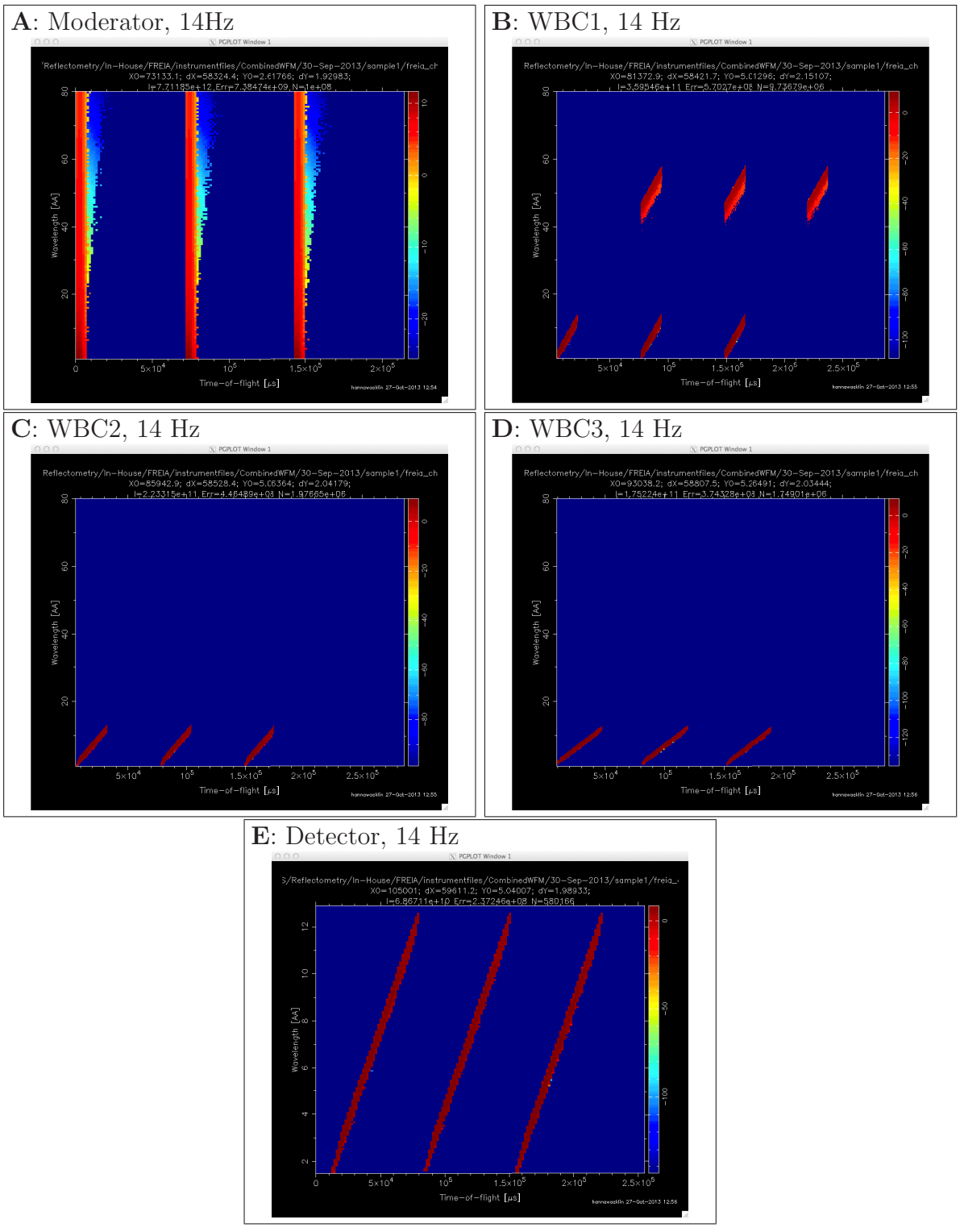
A: Moderator, 14Hz
B: WBC1, 14 Hz
C: WBC2, 14 Hz
D: WBC3, 14 Hz
E: Detector, 14 Hz
Wavelength [Å]
Time−of−flight [μs]

Figure 20:

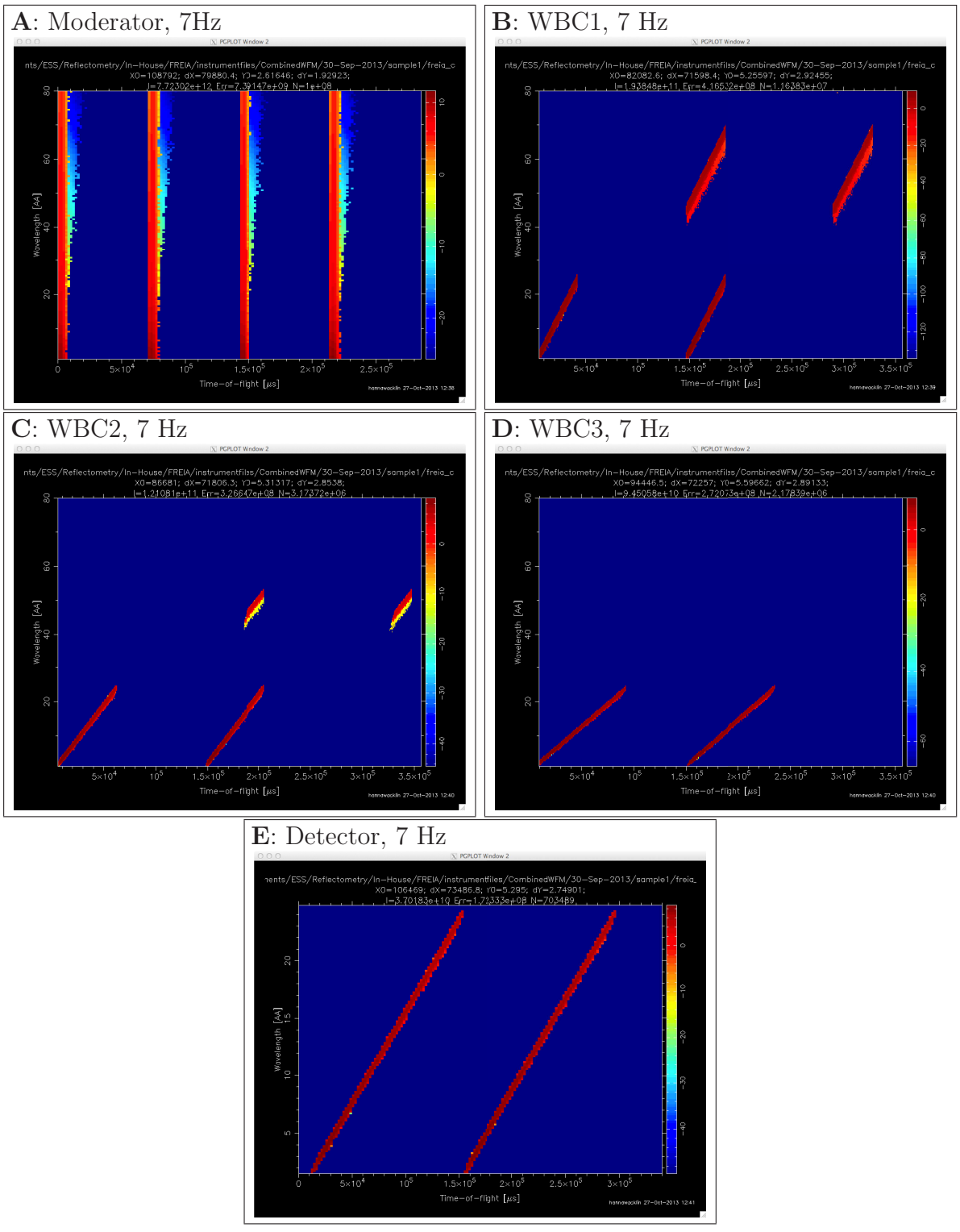
A: Moderator, 7Hz
B: WBC1, 7 Hz
C: WBC2, 7 Hz
D: WBC3, 7 Hz
E: Detector, 7 Hz
Wavelength [Å]
Time−of−flight [μs]

Figure 21:

the first window:

$$t11_{\max}(\mu s) = 252.78 \times (\text{posWFM1} - 0.5 \times z_0)\text{Lam}_{\min} + 2860\mu s\,.$$

The first window of the second WFM chopper is set to open at the same time as WFM1 closes:

$$t21_{\min} = t11_{\max}$$

The selected pulse width for this wavelength is defined by the chopper separation z_0:

$$W\text{Lam}_{\min 1} = 252.78 z_0\,\text{Lam}_{\min}$$

The longest wavelength of the first frame ($\text{Lam}_{\max 1}$) is now determined by the start of the source pulse ($t = 0$) and the opening point of the first window of WFM2.

$$\text{Lam}_{\max 1} = t21_{\min}/252.78 \times (\text{posWFM1} + 0.5 \times z_0))$$

The intersection of the longest wavelength with the position of WFM1 then defines the opening point of the first window of WFM1:

$$t11_{\min} = 252.78 \times (\text{posWFM1} - 0.5 \times z_0) \times \text{Lam}_{\max 1}$$

The time at which the longest wavelength intersects the position of WFM2 defines its closing point.

$$t21_{\max} = t11_{\max} + 252.78 \times \text{Lam}_{\max 1} z_0;$$

and the pulse width of the longest wavelength is given by:

$$W\text{Lam}_{\max 1} = t21_{\max} - t21_{\min}$$

The time during which each window is open (Topen) is defined by (for the base width of the pulse):

$$\text{WFM11Topen} = (t11_{\max} - t11_{\min})$$

and

$$\text{WMF21Topen} = (t21_{\max} - t21_{\min})$$

The angular opening of each window is proportional to this time and the chopper frequency (Hz):

$$\text{WFM1A1} = 360 \times F \times \text{WFM11Topen}$$

$$\text{WMF2A1} = 360 \times F \times \text{WFM21Topen}$$

The phasing of choppers relative to the centre of the guide (when phase = 0) The first chopper in a pair starts to open when $\text{Lam}_{\max}$ from the beginning of the pulse arrives, from which the time at which each window (H x W)) is centered at the guide can be defined:

$$tWFM11 = t11_{\min} \times 10^{-6} + 0.5 \times (\text{WFM1A1} + W/(R - H))/(2 \times \pi \times \sqrt{(F \times F)});$$

and

$$t\text{WFM21} = t21_{\min} \times 10^{-6} + 0.5 \times (\text{WFM2A1} + W/(R - H))/(2 \times \pi \times \sqrt{(F \times F)});$$

The next window is defined using the fact that the minimum wavelength of each frame is the same as the maximum wavelength of the previous frame:

$$\mathrm{Lam}_{\mathrm{min2}} = \mathrm{Lam}_{\mathrm{max1}}$$

and so on. The number of sub-frames needed to fill the time-of-flight frame at the detector depends on the length of the instrument (L) and the natural length of the instrument (L_{nat}) at which a single frame would fill the frame:

$$N = (L_{\mathrm{nat}} - \mathrm{posWFM})/(L - \mathrm{posWFM}) = (\mathrm{posWFM} \times T)/t(L - \mathrm{posWFM})$$

where t is the pulse length and T is the source period. For a 25m instrument with the WFM choppers centred at 6.9m, this gives 9 frames for 71.42ms The chopper rotation speeds that can be used depend on the length of the wavelength band selected, i.e. the time required from the start of the first frame until the end of the last frame at each chopper position, e.g. for seven sub-frames:

$$F(Hz) = (t17_{\mathrm{max}} - t11_{\mathrm{min}})/T$$

Limitations of Wavelength Frame Multiplication The resolutions that can be achieved by WFM at ESS depend on the length of the instrument, the wavelength band and the guide dimensions. Some basic truths are:

- WFM cannot be used to decrease the natural resolution of the source!
- When the natural resolution of the longest wavelengths approaches that of the WFM system, it becomes hard to separate the sub-frames
- The length of the frames, as well as their separation in time get progressively shorter with increasing wavelength, making it more difficult to avoid frame overlap
- The length of the frames increases with decreasing resolution

As a result, for any given instrument length and wavelength band, there is an upper limit to the resolution that WFM can used. In general there is need for two or three frame overlap choppers to

1. avoid cross-talk between the frames
2. avoid contamination from the source pulse tail (which extends to 5ms).

The latter in particular requires that a chopper is placed half-way between the WFM choppers and the detector, at which point the sub-frames already fill half of the 71.42ms period (if they fill the full frame at the detector). As a consequence, this chopper can then rotate only a 2 x 14Hz.

The largest possible radius and the frequency of the last frame overlap chopper limit the dimensions of the guide that can be used, or alternatively the worst resolution (=longest sub-frames) that can be generated on any given instrument.

It is often necessary to reduce the window size of this chopper by a small fraction to achieve full sub-frame separation at the detector. The limiting factor is that there still needs to be sufficient intensity in the wavelength overlap regions between the subframes, so that a continuous spectrum can be used.

The consequence for FREIA is that the full bandwidth (2.5-11.3Å) cannot be used for WFM resolutions above 2.5% (full width).

5.3 Cross talk between collimation slits

In the kinetic mode with all three collimation slit pairs open, it is possible that some wrong beams that exit S1 can lead to crosstalk and get through the wrong opening at S2. Figure 22 shows that mostly these wrong beams fall outside the working range of S2, which is only 2 cm due to the strong focusing of the beam towards the sample. It is worth noting that there is no cross-talk between the slit position for the highest (4.1°) and lowest angles (0.35°), and that while the middle angle may have some crosstalk with the other two angles, most of these cross-beams will not fall on sample. They may however hit the detector and will contribute to background. This would imply that the fast shutters for the kinetic mode would be needed at both slit positions. We investigated a simple idea of a split guide with absorbing walls

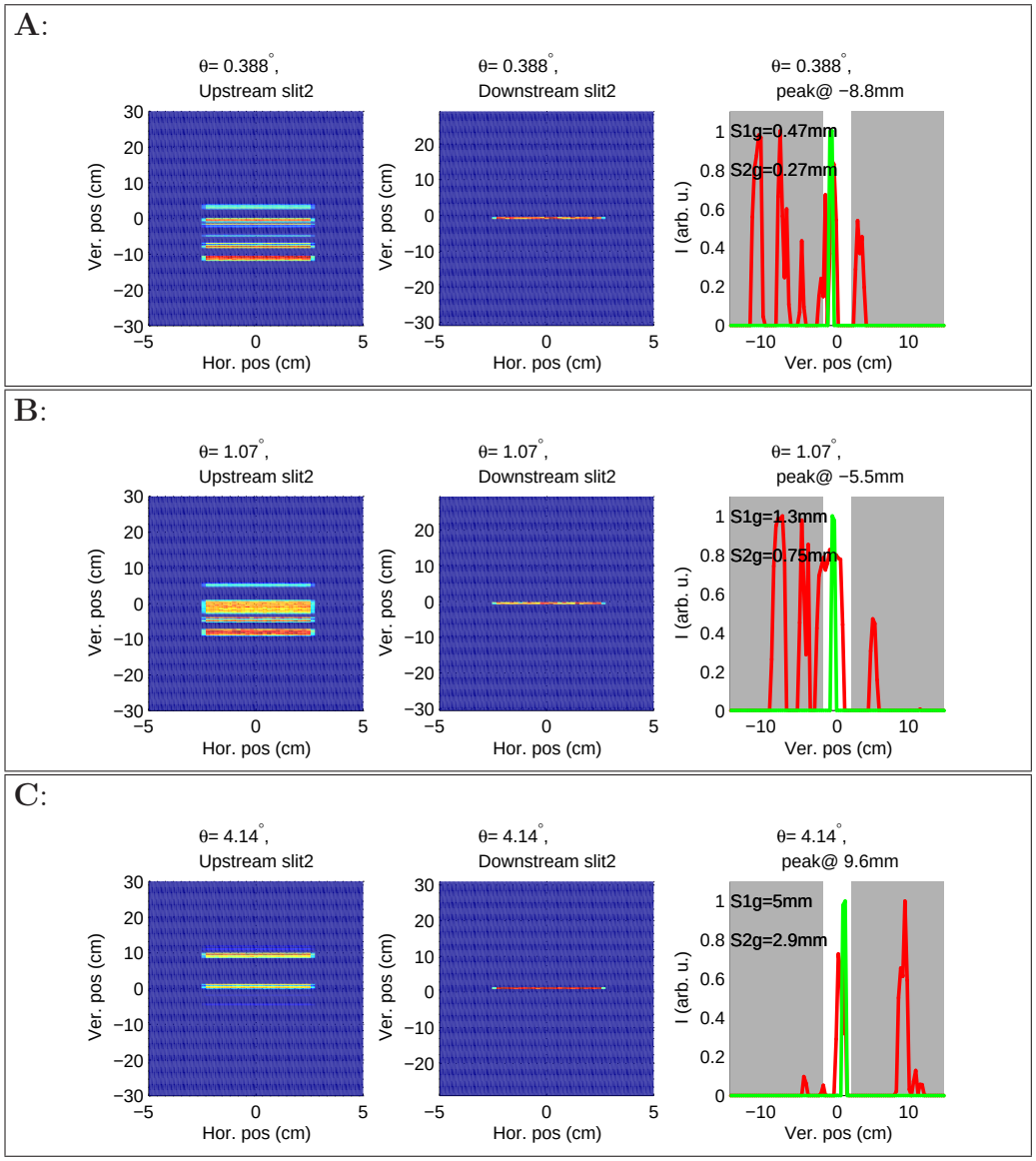

Figure 22:

(as illustrated in Fig.23) as a means to avoid a second pair of fast shutters, and found that a such a guide is able to prevent all the crossbeams. The model simulated in McStas was a

split guide with four equally spaced channels with wall thicknesses between 0.5 and 1mm. In reality the channel widths and wall positions can be optimized such that only three channels will be needed.

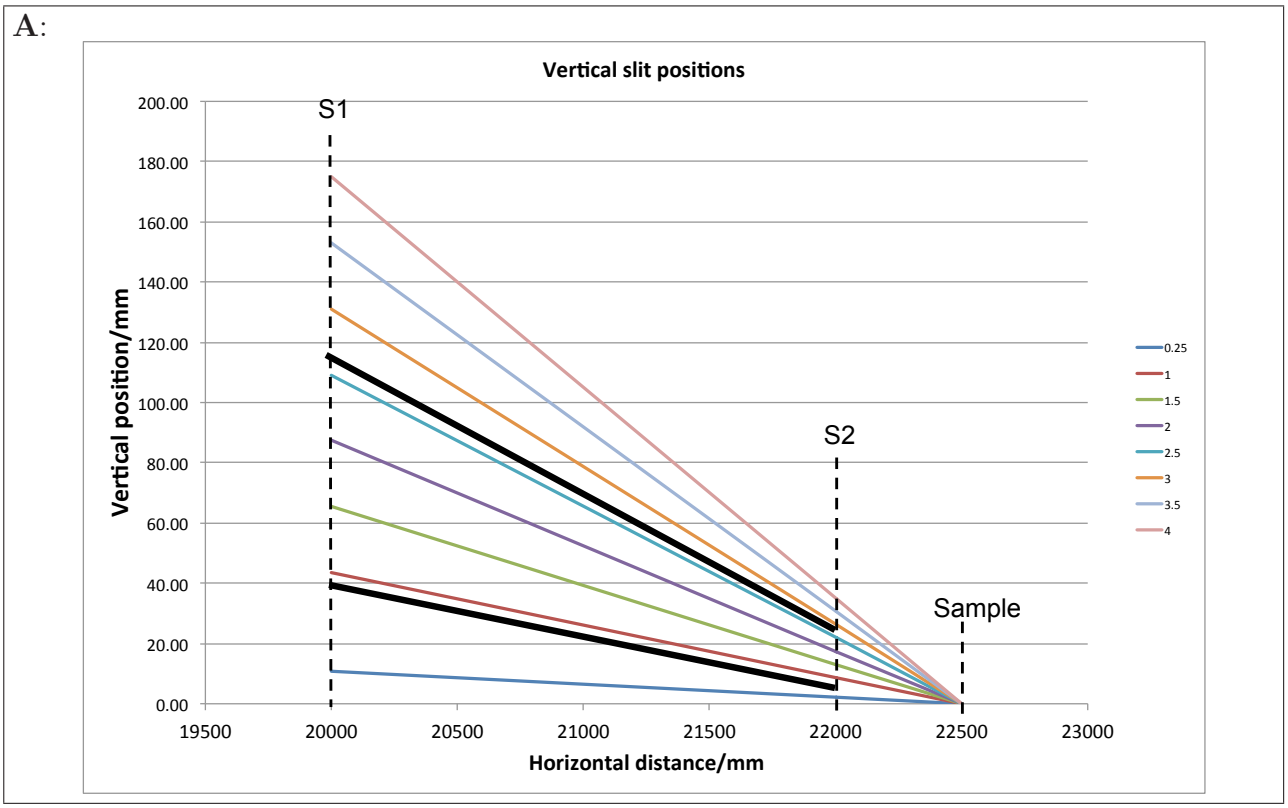

Figure 23:

5.4 The elliptical guide optimization strategy

The aim in the design of the elliptical guide and optimization was to obtain an as gapless as possible distribution of intensity vs grazing angle and horizontal position within an 40×40 mm^2 horizontal area centered in the vicinity of the 2nd focal point of the elliptical guide. In addition to this, the wavelength spectrum reaching the sample should be spatially homogeneous as well as independent of the value of $\Delta\theta/\theta$. The optimization includes 4 independent steps:

1. optimizing the distribution of intensity vs grazing angle at the sample position (at 3Å)
2. optimizing the beam extraction shielding (ensuring Line Of Sight elimination, reduction of background radiation at the sample position
3. optimizing the horizontal focusing of the beam
4. optimizing the coating of the guide

Below we outline how the guide was optimised. The remaining optimizations are available on request.

5.5 optimizing the distribution of intensity vs grazing angle at the sample position

The shape of the guide side walls has no impact on the distribution of intensity vs grazing angle at the sample position. Rather it is controlled by the mirror orientation, the guide inclination, the top and bottom guide shape and the relative vertical positions of the moderator, the mirror, the guide and the sample. In order to improve statistics for this part of the optimization, only neutrons with zero horizontal divergence have been included in the simulations.

The wavelength spectrum of interest is spans from 2Å to 10Å. However, during this part of the optimization, the wavelength band is limited to 0.001Åcentered at 3Å. This is to ensure that the optimized guide will transport both short and longer wavelengths, since the longer wavelengths have a larger critical angle of reflection. The coating of mirror is m=6. For the optimizations, the guide coating is m=6. This is solely to avoid the situation where the guide shape is controlled by some arbitrary choice of m-value distribution through the guide. The optimal distribution of m-values (which is far from m=6 all the way), taking also cost into account, is determined after the guide shape is fixed. The Figure-Of-Merit used in the optimization is the intensity monitored within a 40×40mm^2 horizontal area centered at the sample position. The FOM-monitor includes only the neutrons with grazing angles in the interval 0°–4°.

Table 3 shows the parameter values varied in the the optimization.

PARAMETER	DESCRIPTION
Y_sample	Vertical position of the sample
Y_mirror	Vertical position of the deflection mirror
Y_guide	Vertical position of the guide
focus_inh	1st focal point position
focus_outh	2nd focal point position
smallaxis_w	Ellipse minor axis
T_mirror	Mirror inclination
TT_guide	Guide inclination

Table 3: Parameters for the optimization including the mirror and the top/bottom shape of the guide.